ÉCOLE DE PHYSIQUE DES HOUCHES
ISUD 2026
15th International Symposium on Ultrasonic Doppler methods for fluid Mechanics & engineering
UGA Université Grenoble Alpes
EPFL

PROCEEDINGS

15^{th} ISUD

May 3^{rd} to 7^{th} , 2026
Ecole de Physique des Houches, Les Houches, France

Organizers & Editors

D. Hurther (LEGI, UGA-CNRS) & G. De Cesare (PI-LCH, EPFL)

ISUD scientific committee

- G. De Cesare, Chair, Ecole Polytechnique Federale Lausanne (EPFL), Switzerland
- S. Eckert, Helmholtz-Zentrum Dresden-Rossendorf, Germany
- S. Fischer, Ubertone, France
- D. Hurther, Universite Grenoble Alpes-CNRS, LEGI, France
- T. Ihara, Tokyo University of Marine Science and Technology, Japan
- H. Kikura, Tokyo Institute of Technology, Japan
- O. Mariette, Met-Flow, Switzerland
- H. Murakawa, Kobe University, Japan
- C. Rennie, University of Ottawa, Canada
- Y. Tasaka, Hokkaido University, Japan
- J. Wiklund, Incipientus Ultrasound Flow Technologies, Sweden
- J. Windhab, Swiss Federal Institute of Technology Zurich (ETH), Switzerland

LEGI
LABORATOIRE DES ECOULEMENTS GEOPHYSIQUES ET INDUSTRIELS

LCH
PLATEFORME DE CONSTRUCTIONS HYDRAULIQUES

UBERTONE

Content

Keynote presentations…………………………..…………………………p4

Day 1 Hydroacoustic metrology of turbulent two-phase flows – a numerical approach
Guillaume Fromant
Day 2 Hydro-acoustic measurements of water and sediment fluxes in rivers
Jérôme Le Coz
Day 3 Exploring the Potential of UVP in Aquaculture
Ippei Oshima

Day 1-May 4th 2026: Ultrasonic Flow Metrology……………..…………p13

A numerical study of velocity biases using wideband multi bistatic Doppler ultrasonic profilers: impacts of the system geometry and the pulse duration. **Maxime Lernould[1]**, Oriana Yon-Campaner[2], Georges Stienne[1], David Hurther[2], Guillaume Fromant[1]

Turbulence-Particle Interactions observed from a single-frequency bistatic pulse-to-pulse coherent Doppler velocimeter. **Joris Weel[1]**, Guillaume Fromant[2], Roeland van de Vijsel[1], Ton Hoitink[1]

Pulse-coherent Doppler velocity profile measurements in turbulent open-channel flows using a novel wideband multibistatic ADVP: contribution & correction of spectral broadening, directivity & Doppler noise effects. **Oriana Yon-Campaner[2]**, Maxime Lernould[1], David Hurther[2], Pierre Alain Barraud[2], Guillaume Fromant[1]

Investigation of uncertainty from parallax bias in high-resolving Acoustic Doppler Velocimetry Profiling. **M. Burckbuchler[1]**, S. Fischer[1], M. Noack[2]

Can Ultrasonic Doppler methods unlock the dynamics of fluid mud in estuaries? **Sophie Defontaine[1,2]**

Multi-Frequency Techniques in Nearshore Sediment Transport Acoustics. **Gregory Wilson[1]**, Eli Faigle[1] & Alex Hay[2]

Day 2-May 5th 2026: Environmental Flows……………………………..…p36

In-situ calibration of Acoustic Backscatter Systems for measuring suspended sand concentrations in rivers. **Bjarne Vincent[1],** Céline Berni[1], Guillaume Dramais[1], Jérôme Le Coz[1], Benoît Camenen[1]

Bedload & suspended sediment transport process analysis in highly turbulent open-channel flows using ACVP technology: performances & limitations. **Christophe Reymond[12]**, David Hurther[12], Giovanni De Cesare[1]

Wave Boundary Layer Dynamics around Onshore-Migrating Bars (based on ACVP measurements). Florian Grossmann[1,3], David Hurther[2], Rafael Almar[1], and **Jose Alsina[3]**

ADV measurements in an aerated Denil fish pass. **J. Schneider**, A. Hussin, S. Haun

Effect of Submerged Vane Field on Flow Characteristics in a Mobile-bed Channel with 30° Water Diversion. **Zehra Büyüker[1]**, Gökçen Bombar[1]

Spatial configurations of submerged roughness elements influence sediment erodibility similarly to their density: a case study of common cockles. Maxime Laukens[1], **Christian Schwarz[1,2]**

Three-dimensional flow structures identified over three-dimensional dunes with the UB-Lab 3C. **Stephen M. Simmons[1]**, Robert E. Thomas[1], Richard J. Hardy[2], Daniel R. Parsons[3], and Stéphane Fischer[4]

Day 3-May 6th 2026: Complex Flows………………………………………p60

Recent activities in ultrasonic flow measurements for liquid metal Rayleigh-Bénard convection. T. Vogt[1], F. Schindler[1], N. Kim[1], S. Su[2], M. Sieger[1], T. Wondrak[1]**, S. Eckert[1]**

Identification of Flow States in the DRESDYN Precession Experiment Using Ultrasound Doppler Velocimetry. **Kunal K. Jani[1]**, André Giesecke[1], Thomas Gundrum[1], Frank Stefani[1]

Fundamental study on ultrasonic pulse reception based on light dfelction effects. **Riku Hirai[1]**, Shuntaro Kozaka[1], Weichen Zhang[2], Hiroshige Kikura[2], Naruki Shoji[3], Hideki Kawai[3]

Experimental study of ultrasound-driven jets in liquid metal. **Elio Guillon[1,2]**, Sophie Miralles[1], Valéry Botton[1], Gilles Despaux[3], Emmanuel LeClézio[3], Sven Eckert[4], Klaus Timmel[4]

Flow Profile Reconstruction of Hydrothermal Fluid Using Experimental Buoyant Jet Model. **Tomonori Ihara**, S. Ueno

Evaluation of Flow Regime and Wetness Fraction in Two-Phase Flows using a Clamp-on Ultrasonic Technique. **Hideki Murakawa[1]**, Yuya Kojima[1], Kodai Kondo[1], Katsumi Sugimoto1

Measurement of Bubble Rising Behavior using an Ultrasonic Phased Array Technique. **Kota Uemura[1]**, Tasuki Nakane[1], Katsumi Sugimoto[1], Hideki Murakawa[1]

Machine Learning-Based Ultrasonic Tomography for Void Distribution Reconstruction with Noise-Reduction Preprocessing. **Yuya Kojima**[1], Hideki Murakawa[1], Katsumi Sugimoto[1], Teppei Kondo[2], Yuta Abe[3], Kosuke Aizawa[3]……………………………………………………………………………………Not available.

	Monday, May 4th	Tuesday, May 5th	Wednesday, May 6th	Thursday, May 7th
7h45-8h45	Breakfast	Breakfast	Breakfast	Lunch box
8h50-9h	Opening (D. Hurther)			**Technical Visit**
9h-10h	Keynote 1 by **G. Fromant**	Keynote 2 by **J. Le Coz**	Keynote 3 by **I. Oshima**	
10h-10h30	Coffee Break Award committee meeting	Coffee Break	Coffee Break	7:30 Bus departure for Veytaux
	Ultrasonic flow metrology (D. Hurther)	**Environmental Flows** (G. De Cesare)	**Complex flows** (H. Murakawa)	
10h30-10h55	M. Lernould (award)	B. Vincent	S. Eckert	9:15-11:15
10h55-11h20	J. Weel (award)	C. Reymond (award)	K.K. Jani (award)	Hydroelectric Powerplant
11h20-11h45	O. Yon-Campaner (award)	J. Alsina	R. Hirai (award)	Veytaux Forces Motrices
11h45-12h10	M. Burckbuchler	J. Schneider	E. Guillon (award)	
12h10-14h00	Lunch	Lunch	Lunch	11:30-12:45 Lunch at Oasis rest.
13:50-14h15			T. Ihara	sponsored by Ubertone
14h15-14h40	S. Defontaine	Z. Büyüker	H. Murakawa	
14h40-15h05	G. Wilson	C. Schwarz	K. Uemura (award)	12:55-14:45
15h05-15h30	To be defined	S.M. Simmons	Y. Kojima (award)	Lake Geneva boat trip
15h30-16h00	Coffee Break	Coffee Break	Coffee Break	15:10-16:30
	Tech. innovation session		Techn. Innovation session	Bus trip Lausanne-Geneva (central bus station)
16h00-16h30	Ubertone (S. Fischer)	ISUD 30th anniversary (G. De Cesare)	Ylec (V. Aumelas)	
16h30-17h30	Free discussion	Free discussion / hiking	-ISUD committee meeting-	
17h30-18h30			Award committee meeting	
19h30	Dinner	Dinner	Dinner -Ubertone Award ceremony-	

Hydroacoustic metrology of sediment transport: a novel numerical approach

Guillaume Fromant[1]

[1] Lab. D'Informatique Signal et Images de la Côte d'Opale (LISIC), Univ. Du Littoral Côte d'Opale, 50 rue Ferdinand Buisson, 62228 Calais, France.

Keywords: Sediment transport, coherent Doppler sonar, ACVP, turbulence, two-phase flows, point-particle, velocity estimation

Accurate modelling and prediction of sediment transport in aquatic environments are essential for sustainable coastal and river management. Current approaches rely on physics-based numerical models combined with detailed measurements of sediment fluxes. In sediment-laden flows, concentrations typically range from 0.01–1 g/L in the upper dilute suspension layer, governed by turbulent motion, to 10–1000 g/L in the lower dense bedload layer, where particle–particle interactions dominate transport. Such conditions generate strong flow opacity, which limits the applicability of optical techniques such as PIV and LDV/LDA. In contrast, high-resolution hydroacoustic instrumentation has emerged as a promising alternative for measuring sediment fluxes. Mono- and multi-bistatic ultrasonic sonar systems, combining pulse-to-pulse coherent Doppler frequency profiling with incoherent backscatter intensity measurements, provide co-located, time-resolved profiles (along the acoustic beam) of both multi-component velocity and sediment concentration. Operating at MHz frequencies, these systems achieve profiling ranges on the order of meters, with millimetric spatial and millisecond temporal resolution [1-6].

These approaches have demonstrated their ability to deliver reliable, high-resolution sediment flux measurements in boundary layers [7-10] and have more recently enabled direct comparisons with turbulence-resolved two-phase flow simulations [11-12]. Nevertheless, despite well-established theoretical foundations—rooted in radar interferometry and medical ultrasound—data processing and interpretation remain challenging in aquatic environments due to the complexity of ultrasound scattering processes. In particular, sensor geometry, echo amplitude and phase statistics, and flow turbulence all limit the achievable accuracy of velocity, concentration, and flux estimates [eg. 13].

This study presents a numerical modelling framework to simulate backscattered echoes recorded by a bistatic Acoustic Concentration and Velocity Profiler (ACVP, [3]) using a point-particle approach. The method enables the representation of complex turbulent flows and aims to improve the estimation of velocity, concentration, and flux. Building on previous numerical efforts (e.g. [13-15]), the model adopts a Lagrangian formulation that explicitly resolves scattering from individual particles. It provides a flexible framework to investigate the influence of beam geometry, pulse characteristics (frequency and duration), particle spatial distribution and scattering properties, as well as flow dynamics on the recorded echoes.

The model is first evaluated in a simplified unidirectional flow, where non-inertial particles (fluid tracers) move at a constant velocity. It is then extended by introducing isotropic turbulent fluctuations using a linear forcing method [16] to assess their impact on echo formation. Finally, a second, inertial particle phase is incorporated to examine the effective mixture velocity observed by the system.

Overall, the proposed numerical model offers a robust framework for investigating the dominant scattering mechanisms in hydroacoustic sediment flux measurements. It also provides a valuable tool for developing improved processing techniques (eg. Two-phase hydroacoustic inversion, [17]) and for better quantifying associated measurement uncertainties.

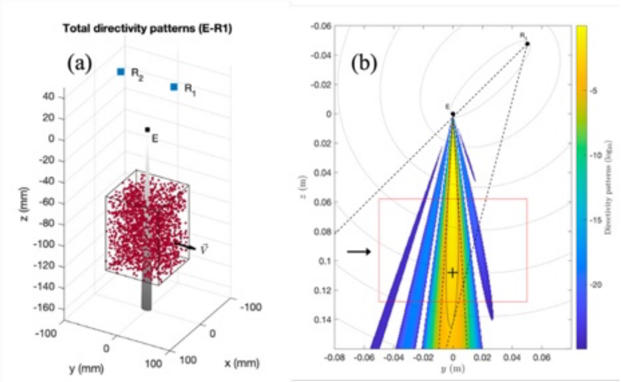

Figure 1: (a) 3D representation of the sampled domain and transducers' sensitivities for one modelled ACVP emitter–receiver couple. The red dots are modelled particles moving. The gray region bound the mainlobe of the emitter-receiver couple diretivity function showing the volume sampled within the simulated domain. (b) Spatial directivity patterns of the modelled system in the yz plane. The red boxes indicate the limits of the domain in which particles are in motion. The dotted lines define the –3 dB limits of the directivity patterns of the emitter and one receiver projected onthe yz plane. The solid black line is the –3 dB contour of the complete system directivity patterns. From [18]

References

[1] Shen, C., and Lemmin, U. (1997). “Ultrasonic scattering in highly turbulent clear water flow,” Ultrasonics 35(1), 57–64.

[2] Zedel, L., and Hay, A. E. (1999). “A coherent Doppler profiler for high-resolution particle velocimetry in the ocean: laboratory measurements of turbulence and particle flux,” J. Atmos. Ocean. Technol. 16(8), 1102–1117.

[3] Hurther, D., Thorne, P. D., Bricault, M., Lemmin, U., and Barnoud, J.-M. (2011). “A multi-frequency acoustic concentration and velocity profiler (ACVP) for boundary layer measurements of fine-scale flow and sediment transport processes,” Coast. Eng. 58(7), 594–605.

[4] Hurther, D., and Lemmin, U. (2001a). “A correction method for turbulence measurements with a 3D acoustic Doppler velocity profiler,” J. Atmos. Ocean. Technol. 18(3), 446–458.

[5] Zedel, L., and Hay, A. E. (2002). “A three-component bistatic coherent Doppler velocity profiler: Error sensitivity and system accuracy,” IEEE J. Ocean. Eng. 27(3), 717–725.

[6] Fromant, G., Mieras, R. S., Revil-Baudard, T., Puleo, J. A., Hurther, D., and Chauchat, J. (2018). “On bedload and suspended load measurement performances in sheet flows using acoustic and conductivity profilers,” J. Geophys. Res. Earth Surf. 123(10), 2546–2562.

[7] Revil-Baudard, T., Chauchat, J., Hurther, D., and Barraud, P.-A. (2015). “Investigation of sheet-flow processes based on novel acoustic high-resolution velocity and concentration measurements,” J. Fluid Mech. 767, 1–30.

[8] Grossmann, F., Hurther, D., van Der Zanden, J., Caceres, I., Sanchez-Arcilla, A., and Alsina, J. M. (2022). “Near-bed sediment transport during offshore bar migration in large-scale experiments,” J. Geophys. Res.: Oceans 127(5), e2021JC017756, http://dx.doi.org/10.1029/2021JC017756.

[9] Guta, H., Hurther, D., and Chauchat, J. (2022). “Bedload and concentration effects on turbulent suspension properties in heavy particle sheet flows,” J. Hydraul. Eng. 148(7), 04022012.

[10] van der Zanden, J., van der A, D. A., Hurther, D., Caceres, I., O’Donoghue, T., and Ribberink, J. S. (2016). “Near-bed hydrodynamics and turbulence below a large-scale plunging breaking wave over a mobile barred bed profile,” J. Geophys. Res.: Oceans 121(8), 6482–6506, https://doi.org/10.1002/2016JC011909.

[11] Cheng, Z., Chauchat, J., Hsu, T. J., and Calantoni, J. (2018). “Eddy interac- tion model for turbulent suspension in Reynolds-averaged Euler–Lagrange simulations of steady sheet flow,” Adv. Water Resour. 111, 435–451.

[12] Chauchat, J., Hurther, D., Revil-Baudard, T., Cheng, Z., and Hsu, T.-J. (2022). “Controversial turbulent Schmidt number value in particle-laden boundary layer flows,” Phys. Rev. Fluids 7(1), 014307.

[13] Zedel, L. (2008). “Modeling pulse-to-pulse coherent Doppler sonar,” J. Atmos. Ocean. Technol. 25(10), 1834–1844.

[14] Dillon, J., Zedel, L., and Hay, A. E. (2012a). “Simultaneous velocity ambiguity resolution and noise suppression for multifrequency coherent Doppler sonar,” J. Atmos. Ocean. Technol. 29(3), 450–463.

[15] Zedel, L., Hay, A. E., Wilson, G. W., and Hare, J. (2021). “Pulse coherent Doppler profiler measurement of bedload transport,” J. Geophys. Res. Earth Surf. 126(4), e2020JF005572, https://doi.org/10.1029/2020JF005572.

[16] Janin, J., Duval, F., Friess, C., & Sagaut, P. (2021). A new linear forcing method for isotropic turbulence with controlled integral length scale. *Physics of Fluids*, *33*(4).

[17] Wilson, G. W., & Hay, A. E. (2015). Measuring two-phase particle flux with a multi-frequency acoustic Doppler profiler. *The Journal of the Acoustical Society of America*, *138*(6), 3811-3819.

[18] Fromant, G., Thorne, P. D., & Hurther, D. (2024). An examination of point-particle Lagrangian simulations for assessing time-resolved hydroacoustic particle flux measurements in sediment-laden flows. *The Journal of the Acoustical Society of America*, *155*(4), 2817-2835.

Hydro-acoustic measurements of water and sediment fluxes in rivers

Jérôme Le Coz[1]

[1] INRAE, Unité de Rechercher RiverLy, Villeurbanne, France.

This lecture reviews some developments of hydro-acoustic methods and software tools for measuring water and sediment fluxes in rivers, and draws research needs and perspectives for operational applications. The hydro-acoustic instruments covered include ADCPs (acoustic Doppler current profilers), ADVs (acoustic Doppler velocimeters), and multi-frequency ABSs (acoustic backscattering systems). Cooperation between field measurement teams and researchers has improved the post-processing, quality control and uncertainty analysis of the results, through the development of operational methods and software packages.

Keywords: River, hydro-acoustics, velocity, discharge, sediment

1. Introduction

Since the beginning of the 21st century, hydro-acoustic instruments have been used increasingly to measure water and sediment fluxes in rivers and canals. This lecture reviews some developments of hydro-acoustic methods and software tools for river measurements, and draws research needs and perspectives for operational applications.

2. Hydro-acoustic instruments for discharge measurements

2.1 ADCPs and ADVs

Adapted from marine science in the 1990's, acoustic Doppler current profilers (ADCP) have become a standard method for discharge measurements by hydrological services nowadays [1,2]. Flow velocity is measured from the Doppler frequency shift of the pulsed ultrasounds backscattered by particles while flow depth is computed from bottom peak detection and time-of-flight. ADCPs usually include 4 single-frequency, bistatic transducers, sometimes a vertical echosounder. Some models have 4 extra transducers operating at a different frequency.

The most common deployment procedure is the moving-boat method: the ADCP displacement is measured either from dedicated bottom pings (Doppler bottom tracking) or from satellite navigation (in case of moving bed, typically). Each river crossing yields a discharge value, the final discharge measurement being the average of a number (usually 6, in France) of discharges over reciprocal crossings.

The other deployment procedure is called “stationary” since the ADCP records depth and time-averaged vertical velocity profiles at a number of fixed positions. Then, discharge is computed using the mid-section method [3,4] used for traditional currentmeters and… their newest hydro-acoustic counterparts: pointwise acoustic Doppler velocimeters (ADVs) and continuous Doppler profilers mounted on a wading rod. These hydro-acoustic instruments have become serious competitors of mechanical and electro-magnetic currentmeters for velocity-area discharge measurements.

ADCPs can also be operated permanently at hydrometric stations: side-looking or, more seldom, up-looking ADCPs continuously record horizontal or vertical, respectively, velocity profiles from which discharge time series can be established, most often using the index velocity method [5,6], based on a calibrated relation between the index velocity (measured) and the cross-sectional average velocity.

2.2 Quality control and uncertainty analysis

Interestingly, for decades end-users, hydrometric agencies and researchers have cooperated (e.g. through the Groupe Doppler Hydrométrie [7] and the International Hydrometry Network) and progressively gained more control on the ADCP, a tool initially seen as a magical black-box. Quality assurance and quality control have been improved through guidelines, manuals, training material for operators, and the internationally developed, open-source QRevInt software [8,9], used for post-processing and reviewing the data from the most common ADCP models.

The development of methods for quantifying discharge measurement uncertainty has been a long-lasting task, still in progress. The interlaboratory tests used in other fields of metrology were adapted to ADCP discharge measurements, through the organization of smaller or larger ADCP intercomparisons (or “regattas”) [10] (cf. Figure 1a). These repeated-measures experiments provide empirical uncertainty estimates based on variance analysis [11]. An open-source software tool (QRame, cf. Figure 1b) for processing regatta results was developed [12] and the World Meteorological Organization (WMO) recently issued guidelines for conducting discharge measurement intercomparisons [13]. Such uncertainty observations in real, diverse field conditions are valuable for improving and validating uncertainty computation methods that have been developed in parallel, especially the OURSIN method [14] implemented in QRevInt.

Similar methods (OURSIN-MS uncertainty [15]) and tools (QRevMS software [16]) are in development for mid-section discharge measurements using hydro-acoustic instruments, including acoustic Doppler currentmeters or velocimeters (ADCs, ADVs) and stationary ADCPs. In such uncertainty methods, the velocity measurement uncertainty is not precisely quantified, since discharge extrapolation or interpolation between verticals are the dominant uncertainty sources, in most situations.

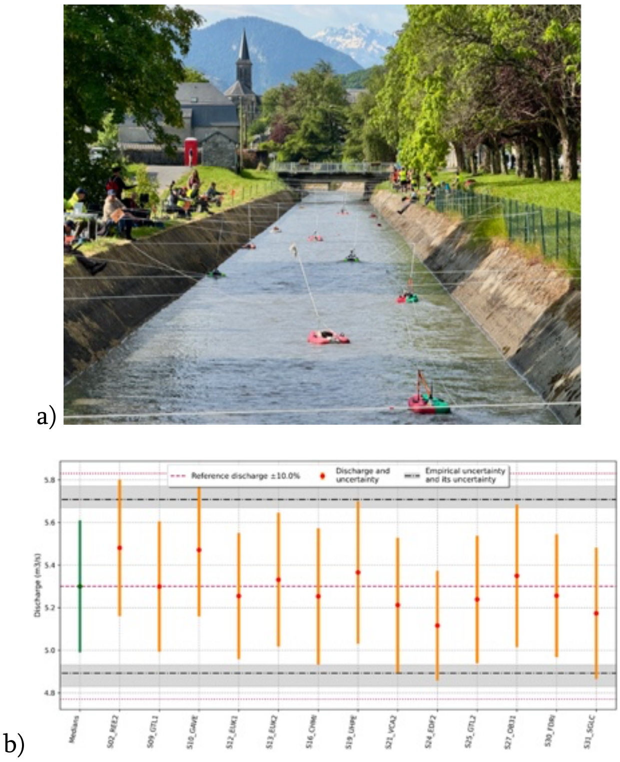

Figure 1: ADCP intercomparison, in the Neste Canal in Hèches, France, June 3, 2025: a) view of the measurements, and b) discharge and uncertainty results in QRame software.

While research and development are ongoing, the practitioners now have much better knowledge and tools to review and defend their hydro-acoustic river discharge measurements through quality control and uncertainty analysis.

3. Sediment transport measurements

Less advanced is the hydro-acoustic measurement of sediment transport in rivers. However, owing to the great potential of less intrusive, high spatio-temporal resolution measurements compared to sediment sampling techniques, a significant research effort has been dedicated to the detection and quantification of bedload and suspended load in rivers, using ADCPs, side-looking ADCPs, and multi-frequency acoustic backscattering systems (ABS).

3.1 Bedload detection and estimation

The difference between bottom-track and satellite navigation displacements yields the apparent velocity of the moving bed, which is an average velocity over a more or less deep portion of the substratum (depending on acoustic frequency), plus potentially a near-bed layer with highly-concentrated suspension [17]. Another difficulty for establishing bedload flux from apparent bed velocity is to estimate the thickness of the moving-bed layer.

3.2 Suspension from backscatter inversion

The suspended load in rivers is typically composed of two populations: fine particles (silt and clay, diameter <67 μm) in relatively homogeneous concentration and grain size throughout the river cross-section, and sands with much higher spatial (vertical) and temporal variability [18]. While the fines can be measured efficiently using optical systems (turbidity meters [19]), only the analysis of acoustic backscatter profiles has the potential to capture the dynamics and fluxes of suspended sands.

A wide range of backscatter inversion methods have been proposed to measure the concentrations, and possibly the size, of suspended particles [20,21]. However, due to the complexity of the acoustic response of sediments [22], the current methods require a high level of expertise (models are imperfect and inversion is sensitive to operator choices and measurement errors), a significant amount of calibration data (from intensive water sampling and analysis), and the deployment of multi-frequency profilers with calibrated transducer constants (such calibration is a difficult task). Also, the in-situ deployment during floods or dam-flushing operations (when sand transport occurs) is a technical challenge (cf. Figure 2a), and the acoustic signal is often biased by spurious scatterers other than solid particles, especially air bubbles or micro-bubbles [23].

In spite of these sources of difficulty, encouraging results were obtained both at monitoring stations equipped with side-looking ADCPs [24,25] and at gauging cross-sections using multi-frequency ABSs [21,26] (cf. Figure 2b). Recently developed software packages like HYDRAC [27] and AcouSed [28] will help test various deployment and inversion methods before their future transfer to operational practitioners.

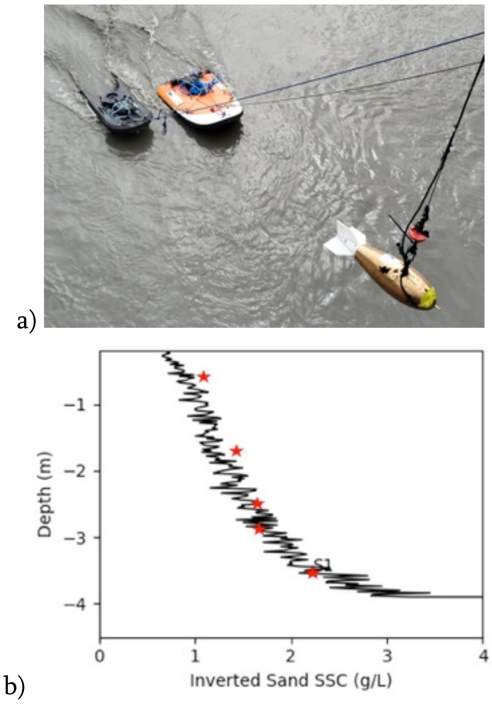

Figure 2: ABS suspended sediment measurements during the Upper Rhône dam flushing operation (APAVER 2025): a) US-P06 sampler, UB-sediflow on the black board and Aquascat on the orange board (photo G. Dramais), and b) sand concentrations at a vertical derived from Aquascat data using the AcouSed software: water samples (stars) and backscatter inversion (line).

4. Summary and research needs

The recent history of hydro-acoustic measurements of water and sediment fluxes in rivers is a fine example of fruitful cooperation between scientists and end-users.

Hydro-acoustic discharge measurements now are a standard in hydrometry with well-established practices, quality control and uncertainty quantification. Nevertheless, uncertainty computation still requires development, to adapt to new instruments and procedure, and validation, through interlaboratory experiments conducted in a broader ranger of contexts and measuring conditions.

Hydro-acoustic sediment flux measurements are still challenging but their potential to supplement, if not replace, traditional methods for suspended sand is attractive. Active research is needed to make hydro-acoustic sediment methods affordable to non-specialist end-users and to quantify the measurement uncertainty. This will be possible through physically-sound and robust inversion methods implemented in operational software. Innovating inversion procedure needs to be tested in field conditions with accurate sampling reference data.

References

[1] Le Coz J, *et al.*: Mesures hydrologiques par profileur Doppler, Editions Quae, 164 p (2008).

[2] Oberg KA and Mueller DS: Validation of streamflow measurements made with acoustic Doppler current profilers. J. Hydraul. Eng., 133 (2007), 1421-1432

[3] ISO 748:2021: Hydrometry — Measurement of liquid flow in open channels — Velocity area methods using point velocity measurements, ISO, Geneva.

[4] Le Coz J, *et al.*: Uncertainty in open-channel discharges measured with the velocity-area method, Flow Meas. Instrum., 26 (2012), 18-29.

[5] Le Coz J, *et al.*: Evaluation of river discharges monitored by a fixed side-looking Doppler profiler, Water Resour. Res., 44 (2008), W00D09.

[6] Levesque VA and Oberg KA: Computing discharge using the index velocity method: U.S. Geological Survey Techniques and Methods 3-A23 (2012), 65 p.

[7] Le Coz J, *et al.*: Jaugeage des rivières par aDcp : pour une culture commune, La Houille Blanche, 04 (2007).

[8] Mueller DS: QRev — Software for computation and quality assurance of Acoustic Doppler Current Profiler moving-boat streamflow measurements — User's manual (2016). US Geological Survey.

[9] Lennermark M and Hauet A: Developing a post-processing software for ADCP discharge measurement piloted by an international and inter-agency group: a unique, ambitious experience… and one that works! EGU22-9379 (2022).

[10] Le Coz J, *et al.*: Estimating the uncertainty of streamgauging techniques using in situ collaborative interlaboratory experiments, J. Hydraul. Eng., 7 (2016), 04016011.

[11] Despax A, *et al.*: Decomposition of uncertainty sources in acoustic Doppler current profiler streamflow measurements using repeated measures experiments, Water Resour. Res., 55 (2019), 7520-7540.

[12] Le Coz J, *et al.*: QRame, an open-source software for post-processing large sets of ADCP discharge measurements and computing their uncertainty, IAHR RiverFlow2024 conference proceedings (2024), Liverpool, UK, 6 p.

[13] WMO: Guidance on Field-based Intercomparison Events for Streamflow Measurement Instruments and Techniques, Expert-Team Hydrometry (in press).

[14] Despax A, *et al.*: Validation of an uncertainty propagation method for moving-boat acoustic Doppler current profiler discharge measurements, Water Resour. Res., 59 (2023), e2021WR031878

[15] Hammemi S, *et al.*: Validation of a novel uncertainty propagation method for stationary acoustic Doppler current profiler discharge measurements, IAHR RiverFlow2026 conference proceedings (2026), Thessaloniki, Greece, 8 p.

[16] https://www.genesishydrotech.com/qrevms

[17] Jamieson EC, *et al.*: Evaluation of ADCP apparent bed load velocity in a large sand-bed river: moving versus stationary boat conditions, J. Hydraul. Eng., 137 (2011),

1064-1071.

[18] Agrawal YC and Hanes DM: The implications of laser-diffraction measurements of sediment size distributions in a river to the potential use of acoustic backscatter for sediment measurements, Water Resour. Res., 51 (2015), 8854-8867.

[19] Navratil O, *et al.*: Global uncertainty analysis of suspended sediment monitoring using turbidimeter in a small mountainous river catchment, J. Hydrol., 398 (2011), 246-259.

[20] Thorne PD and Hurther D: An overview on the use of backscattered sound for measuring suspended particle size and concentration profiles in non-cohesive inorganic sediment transport studies. Cont. Shelf Res., 73 (2014), 97-118.

[21] Vergne A, *et al.*: Using a down-looking multifrequency ABS for measuring suspended sediments in rivers, Water Resour. Res., 56 (2020), e2019WR024877.

[22] Vergne A, *et al.*: Acoustic backscatter and attenuation due to river fine sediments: Experimental evaluation of models and inversion methods, Water Resour. Res., 57 (2021), e2021WR029589.

[23] Vergne A, *et al.*: Some backscatter modelling issues complicating the sonar-based monitoring of suspended sediments in rivers, Water Resour. Res., 59 (2023), e2022WR032341.

[24] Moore SA, *et al.*: Using multifrequency acoustic attenuation to monitor grain size and concentration of suspended sediment in rivers, J. Acoust. Soc. Am., 133 (2013), 1959-1970.

[25] Marggraf J, *et al.*: Improving hydroacoustic methods for monitoring suspended-sand flux and grain size in sediment-laden rivers, Earth Surf. Process. Landf., 50 (2025), e6056.

[26] Dramais G, *et al.*: Combining sampling and acoustic backscatter profiling for estimating suspended sand concentrations during dam flushing, IAHR RiverFlow2026 conference proceedings (2026), Thessaloniki, Greece, 9 p.

[27] Fromant G, *et al.*: Hydrac, an inversion software for SPM quantification, IAHR RiverFlow 2020 conference proceedings (2020), 340-348

[28] Moudjed B, *et al.*: AcouSed: a software for acoustic inversion to compute concentrations of suspended sediments in rivers., IAHR RiverFlow2024 conference proceedings (2024), Liverpool, UK, 6 p.

Exploring the Potential of UVP in Aquaculture

Ippei Oshima[1, 2]

[1] Institute of Fluid Science, Tohoku University, 2-1-1 Katahira, Aoba-ku, Sendai, Miyagi 980-8577, Japan.
[2] Center for Mathematical Science and Advanced Technology, Japan Agency for Marine-Earth Science and Technology, Yokohama, Kanagawa 236-0001, Japan.

In aquaculture, quantifying feeding activity is a critical issue because it directly influences fish growth, health, and feeding efficiency. While feeding behavior has been studied using various sensing techniques, quantitative measurement remains difficult. Underwater cameras allow direct observation of fish behavior during feeding and provide detailed information on individual motion and group dynamics. Imaging sonar extends observation to nighttime and turbid environments, enabling visualization of fish distribution and collective behavior where optical methods fail. However, each method has limitations, and no single approach provides continuous and reliable monitoring. In this keynote, we present our efforts to characterize fish behavior using multiple sensing techniques, including cameras, imaging sonar, and UVP. We show how each method captures different aspects of fish behavior. Although the application of UVP to actively swimming fish is still at an early stage, our results show that it can detect fish presence and motion. We discuss how UVP can complement existing methods and enable quantitative monitoring of feeding activity in aquaculture systems.

Keywords: Aquaculture, Fish behavior, Fish detection, Optical and acoustic measurements

1. Introduction

Fisheries are a major source of protein. Aquaculture is important because it provides a stable protein supply while reducing pressure on wild resources. In aquaculture systems, understanding fish behavior is essential for effective management. Feeding activity is a key factor that directly influences fish growth, health, and feed efficiency. By monitoring and controlling feeding activity, production performance can be improved. In addition, early detection of abnormal behavior can help identify problems such as red tides, parasite infections, and sudden mortality.

In practice, feeding activity is often evaluated indirectly using physiological or production-based indicators. Conventional methods use physiological indicators such as feed intake, weight gain, and feed conversion ratio (FCR) [1]. These indicators show the results of feeding, but not the behavior itself.

Recently, behavioral approaches have been introduced to assess feeding activity. Fish behavior in individual fish is measured using sensors such as video cameras, sonar systems, and motion sensors. These methods measure swimming speed, acceleration, and feeding responses (e.g., [2]). Feeding activity of fish groups is estimated from collective motion, often using optical flow analysis [3, 4]. Biologging can detect feeding-related events with high accuracy. However, it is difficult to apply at production scale [5].

Although echosounders are widely used in fisheries, they are not often applied in fish cages where fish are densely raised. Many challenges in using acoustic techniques have been reported. Acoustic techniques are used to estimate feeding activity from fish distribution and movement. Fish in low-visibility conditions can be observed using imaging sonar and have been detected based on both direct echoes and acoustic shadows [6]. Aggregation and dispersion during feeding in fish cages have been monitored using scanning sonar [7]. These methods do not measure feeding directly. Instead, they estimate it from fish movement and distribution.

In this keynote, we present our research using underwater cameras, imaging sonar, and UVP. Each method captures different aspects of fish behavior. Although the use of ultrasonic velocity profilers such as UVP and ADCP for actively swimming fish is still limited and at an early stage, these techniques can detect fish presence and movement. We also discuss how these techniques can be used for quantitative monitoring in fish cages. UVP measures velocity, which allows quantitative analysis of fish movement that is difficult with existing methods.

2. Visualization using underwater camera

Direct visualization using underwater cameras is useful. Figure 1 shows a snapshot of swimming Yellowtail (*Seriola quinqueradiata*), illustrating typical group behavior. In the previous study, swimming speed and movement characteristics have been estimated from image correlation. However, cameras installed in sea cages move due to cage oscillation, wave motion, and fish motion. Hence, these evaluation methods are difficult to apply.

We are developing methods to evaluate fish movement directly. We track the motion of the caudal fin over time and calculate tail beat frequency (TBF) using image analysis with AI. TBF at three time points from before to after feeding is shown in Fig. 2. The result shows that feeding increases TBF, indicating higher feeding activity.

Figure 1: Underwater camera image of Yellowtail in a sea cage.

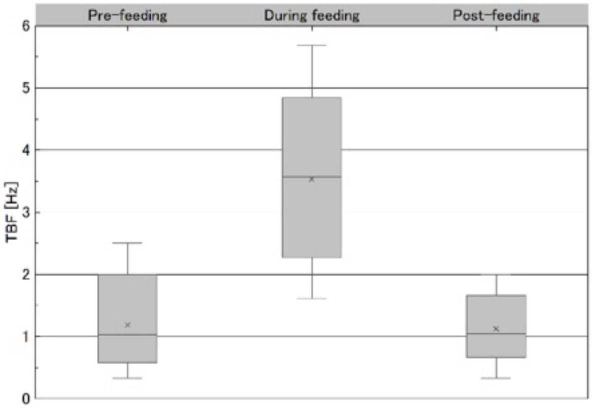

Figure 2: Tail beat frequency (TBF) from before to after feeding, obtained by automated image analysis.

After feeding, TBF decreases as feeding activity is reduced.

3. Visualization using imaging sonar

Imaging sonar can observe fish behavior in low-visibility conditions and over a wide area where optical methods are limited. Figure 3 shows an acoustic image of Chub mackerel (*Scomber japonicus*) in a land-based fish cage, captured using imaging sonar. Fish are observed as thin, bright targets. Acoustic shadows can also be identified in the image.

This method can visualize fish distribution and group behavior even in turbid water or at night, allowing monitoring of changes in aggregation and dispersion. However, the interpretation of sonar images is not easy because they include noise caused by factors such as air bubbles and speckle noise. Therefore, quantitative evaluation of fish behavior is difficult.

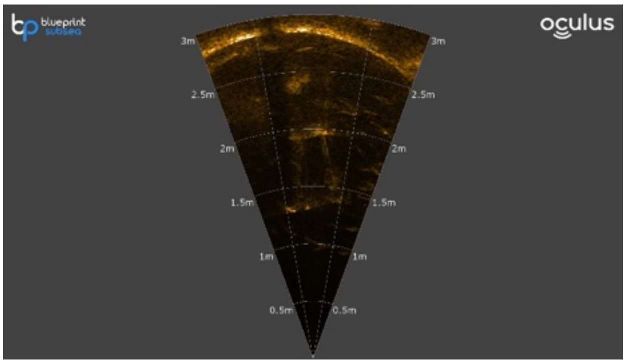

Figure 3: Image captured by an imaging sonar. Many thin, bright targets are fish.

4. Velocity measurement using UVP

Fish cages have various shapes such as circular and rectangular, and are used in land-based, offshore, and submersible systems. Understanding the flow velocity distribution both inside and outside the cages is useful for maintaining water quality, ensuring appropriate swimming conditions for fish, optimizing feed dispersion, and determining cage placement and depth.

As methods for measuring spatial flow distributions, ADCP and UVP can be considered. Both instruments can measure velocity profiles along an ultrasonic beam. For example, it has been reported that in ADCP measurements, when a fish school passes through the beam, the echo intensity increases and the velocity of the fish school, which acts as a scatterer, is measured [8]. Depending on the transducer frequency and the sampling volume of the beam, it may be possible to capture the swimming characteristics of individual fish.

We conducted UVP measurements in a land-based fish cage containing many Chub mackerel. We investigate what types of fish-related events can be detected. Figure 4 shows a colormap of the velocity field measured by UVP. In some regions where velocities higher than the background flow are observed, fish presences can be detected.

Although the application of UVP to actively swimming fish is still at an early stage, the results show its potential for monitoring fish behavior in aquaculture systems.

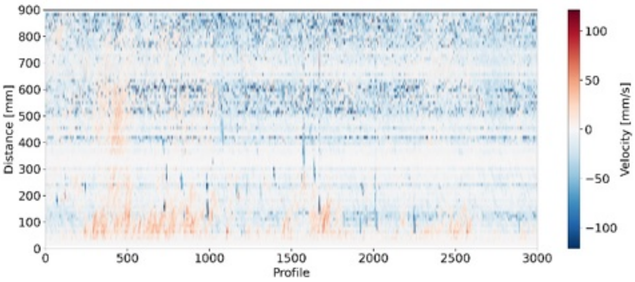

Figure 4: Colormap of velocity distribution measured by UVP. Fish are detected as elongated regions with strong negative velocity signals.

5. Summary

In this study, we presented our recent work to monitor fish behavior in aquaculture using underwater cameras, imaging sonar, and UVP. Each method captures different aspects of fish behavior.

Underwater cameras observe fish behavior directly and can estimate tail beat frequency (TBF) through image analysis. Imaging sonar extends observation capability to low-visibility environments and provides information on fish distribution and group behavior. UVP measures velocity profiles and can detect fish-related signals in the flow field. The results demonstrate that fish presence and movement can be identified as velocity signals, providing a basis for quantitative analysis.

These results indicate that combining optical and acoustic techniques with velocity measurements can improve monitoring of fish behavior in aquaculture systems.

Acknowledgement

This work was supported by Cross-ministerial Strategic Innovation Promotion Program (SIP), “Building a Resilient and Nourishing Food Chain for a Sustainable Future” (Grant Number JPJ012287; funding agency: Bio-oriented Technology Research Advancement Institution). The author would like to thank Dr. Haruka Nishikawa, Dr. Gen Li, Dr. Go Eguchi, Mr. Yusuke Horiguchi, Ms. Yukiyo Kobayashi of Japan Agency for Marine-Earth Science and Technology (JAMSTEC), Prof. Takero Yoshida of Nihon University, Dr. Tomohito Imaizumi of Japan Fisheries Research and Education Agency (FRA) and Prof. Osamu Tominaga of Fukui Prefectural University for their cooperation.

References

[1] Cho CY & Bureau DP: Reduction of Waste Output from Salmonid Aquaculture through Feeds and Feeding, Prog. Fish-Cult. 59 (1997), 155–160.

[2] Kawabata Y, *et al.*: Use of a gyroscope/accelerometer data logger to identify alternative feeding behaviours in fish, J. Exp. Biol. 217 (2014), 3204–3208.

[3] Ubina N, *et al.*: Evaluating fish feeding intensity in aquaculture with convolutional neural networks, Aquacult. Eng. 94 (2021), 102178.

[4] Zhao S, *et al.*: Fish feeding behavior recognition via lightweight two stage network and satiety experiments, Sci. Rep. 15 (2025), 30025.

[5] Broell F, *et al.*: Accelerometer tags: detecting and identifying activities in fish and the effect of sampling frequency, J. Exp. Biol. 216 (2013), 1255–1264.

[6] Connolly RM, *et al.*: Out of the shadows: automatic fish detection from acoustic cameras, Aquat. Ecol. 57 (2023), 833–844.

[7] Sauphar C, *et al.*, Monitoring behavior of post-smolts Atlantic salmon (Salmo salar) during their first month after sea transfer in a commercial sea cage using a mechanical 360-degree single-beam scanning sonar, Aquac. 620 (2026), 743909.

[8] Zedel L, *et al.*: Acoustic Doppler current profiler observations of herring movement, ICES J. Mar. Sci., 60 (2003), 846-859.

A numerical study of velocity biases using wideband multi bistatic Doppler ultrasonic profilers: impacts of the system geometry and the pulse duration.

Maxime Lernould*[1], Oriana Yon-Campaner[2], Georges Stienne[1], David Hurther[2], Guillaume Fromant[1]

[1]Laboratoire d'Informatique, Signal et Image de la Côte d'Opale (LISIC), Université du Littoral Côte d'Opale (ULCO), Calais, France.
[2]Laboratoire des Écoulements Géophysiques et Industriels (LEGI), Université Grenoble Alpes (UGA), CNRS UMR 5519, Grenoble, France.
*contact: mailto:maxime.lernould@univ-littoral.fr

Validation of turbulent two-phase flow simulations requires high-resolution multi-frequency measurements of velocity and concentration within the benthic boundary layer. While multi-bistatic acoustic Doppler systems like the ACVP offer non-intrusive profiling in opaque suspensions, their use with broadband sensors at multiple frequencies introduces complex instrumental biases. This study investigates two primary sources of error: spectral broadening induced by ultrashort pulses and the finite bandwidth of the sensors, and geometric biases arising from frequency-dependent directivity beampatterns. Using a Lagrangian point-particle numerical simulation, we demonstrate that velocity is systematically overestimated (underestimated) when the nominal carrier frequency of the pulses is lower (higher) than the central frequency of the sensors. A comprehensive correction strategy is formulated to simultaneously compensate for these spectral and geometric effects. Results show that the proposed method accurately recovers the prescribed velocity field, regardless of the pulse duration or sensor bandwidth. This integrated correction is a critical step for improving the metrological performance of multi-frequency ultrasonic profilers in sediment-laden flows.

Keywords: multi-bistatic pulse-to-pulse coherent Doppler sonar, multi-frequency, velocity bias, broadband sensors, spectral broadening, sediment transport.

1. Introduction

Validation of two-phase flow simulations requires high-resolution measurements of each flow phase velocities and particle phase concentration within the benthic boundary layer. While conventional optical systems (PIV, LDV) are effective in dilute environments, they become impractical in high-concentration regimes due to the opacity of the mixture. In this context, acoustic techniques offer an efficient alternative: bistatic ultrasonic Doppler systems operating in the MHz range non-intrusively penetrate opaque suspensions and enable simultaneous profiling of collocated multi-component velocity and concentration with high spatial ($\mathcal{O}$(mm)) and temporal $\mathcal{O}$(ms)) resolutions. This is the case of the ACVP (Acoustic Concentration and Velocity Profiler) technology, which is a multi-bistatic system using a high-directivity central emitter with several wide-angle receivers to permit nearly collocated bistatic velocity measurements along a profile aligned with the transmitting direction. This system has recently showed major metrological advances in terms of single-frequency particle flux estimation (Hurther et al., 2011, Revil-Baudard et al., 2015, Fromant et al., 2018 [1-3]). This system also suggests its strong potential to concurrently resolve the fluid phase of turbulent flows through the frequency-dependent scattering properties of turbulent microstructures formed by passive additive quantities (Shen and Lemmin, 1997, Lavery et al., 2003 [4-5]).

In a will to resolve each phase of turbulent two-phase flows using ultrasonic Doppler systems and improve hydroacoustic metrology of sediment transport, it thus becomes mandatory to consider the capability of such systems to provide measurements at multiple frequencies using broadband sensors.

However, the use of these systems at multiple frequencies, particularly in multi-bistatic configurations, is subject to complex instrumental biases in terms of velocity:

First, ultrasonic Doppler systems operating in the MHz frequency range usually emit ultrashort pulses ($\mathcal{O}(\mu s)$) in a will to maximize the measurements spatial resolution ($\mathcal{O}(mm)$), which induces a spectral broadening of the emitted pulse around the carrier frequency. This spectral broadening is suspected to be subsequently weighted by the sensors frequency responses. This in turn would offset the frequency effectively emitted in the medium (Willink and Evans, 1996 [6]), which differs from the nominal frequency imposed by the system's electronics the more it deviates from the sensors central frequency. Subsequent velocity estimations are however carried out considering the system nominal frequency.

Secondly, bistatic systems measurement geometry brings additional challenges for multiple component velocity field reconstruction as each measurement volume along a profile is not exactly centered on the transmitting direction, but rather on the barycenter of the (frequency-dependent) directivity beampatterns across the isotravel lines defining the measurement volume of interest within a profile (Figure 1). This geometric bias becomes even more intricate as the spectrum of the emitted pulse spreads around the carrier frequency.

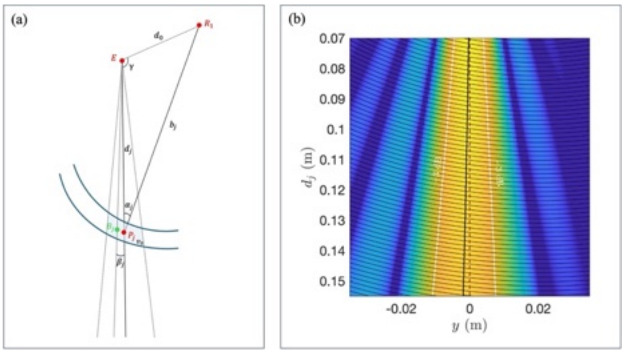

Figure 1: (a) (Color online) Schematics of the geometry of one emitter (E) receiver (R) of an ACVP system in a Cartesian coordinate system. The emitter E and receiver R_1 are separate by a distance d_0. γ is the angle formed by the (ER_1) axis and the emitter normal axis (vertical axis here). Each j particles are positioned at a distance d_j from E and b_j from R_1, the angle formed by these two components is α_j. P_j is the center of the sampled volume v_0. B_j is the pressure barycenter of the volume v_0 and the angle between the emitter axis and the axis $(E-B_j)$ is β_j. The grey dotted lines define the –3 dB threshold of the directivity beampatterns. (b) (Color online) Spatial directivity beampatterns of a modelled ACVP emitter-receiver couple working at 1MHz in the yz plane. The emitter E and the receiver R_1 are aligned in the yz plane. The white solid lines define the –3 dB threshold of the directivity beampatterns. The thin black curves are the isotravel distances from E to R_1, separated by one pulse duration of 2 μs, which defines the different volumes sampled by receiver R_1. Here, the emitter-receiver distance is $d_0 = 0.0704$ mm, the angle formed by the vertical and $E-R_1$ directions is $\gamma = 2.3512$ rad. E is located at (0,0,0) m, R_1 is located at (0,0.05, –0.045) m. The red dotted line shows the emitter axis, aligned here with the vertical axis. The thick black line shows the range dependent position of the pressure barycenter for each sampled volume.

An integrated correction strategy has been formulated to compensate for these effects. It corrects the velocity estimate by taking into account the effective frequency and the recalculated frequency-dependent beampatterns. From this correction, we then define an effective carrier frequency f_{eff} for the recorded echoes:

2. Numerical simulation

The implemented numerical simulation environment is based on a Lagrangian point-particle approach (Fromant and al, 2024 [9]) to model backscattered ultrasonic demodulated echoes. The model was improved to digitally reproduce the complete acoustic measurement chain of a bistatic ACVP system including the measured wideband frequency response of the transducers. N particles (here considered as perfect fluid tracers), treated as individual non-inertial scatterers with constant scattering properties, are initially distributed randomly in a rectangular simulation domain (defined by x, y, z). The simulation generates P_n pulses at a fixed pulse repetition frequency f_{prf} . At each time step, corresponding to the time separating two consecutive pulses, the position of each particle is updated according to its imposed advection velocity (set constant over the y direction to $(u, v, w) = (0.33,0,0)\, m/s$). To keep a constant volume concentration in the simulation box, particles leaving the domain are cyclically reintroduced on the opposite side at a random lateral position, thus avoiding periodicity effects. The complete temporal echo $b(t)$ is then calculated by summing the individual contributions of each particle, integrating the directivity of the system, the attenuation and the Doppler frequency shift induced by the particles' motion. For a fixed carrier frequency of the emitted pulse, we consider each produced echo as a sum of Fourrier modes to account for spectral broadening effects. The recorded echoes can be expressed as follows:

$$b(t) = \sum_{p=1}^{N_p} \sum_{n=-\infty}^{+\infty} a(p,n) \cos\left(2\pi f(n) t + \varphi(p,n)\right) \tag{1}$$

With a (φ) the echo amplitude (phase) of the nth Fourrier mode coming from particle corresponding to the frequency $f(n)$. The sum of the backscattered echoes $b(t)$ from the N particles contained in the insonified volume v_0 is then demodulated in order to extract their in-phase $(I(t))$ and quadrature $(Q(t))$ components. In practice, the recorded signal at a receiver is demodulated using the reference signal imposed to the system prior to the pulse generation (of nominal frequency f_{nom}) to obtain $I(t)$ and $Q(t)$, as described in Rolland, 1995 [8], from which the Doppler frequency ν_D at each receiver can be estimated. From these components, the quasi-instantaneous velocity can be calculated from ν_D. A number of numerical simulations were carried out by imposing different pulse durations ($\tau_c = [2, 8]$ oscillation cycles) at fixed carrier frequencies ($\nu = [0.66, 0.83, 1.04, 1.25, 1.39]$ MHz), in the case of broadband sensors (the measured impulse response of which is fed as input to the simulation) and infinite band sensors (idealized case). The same post-processing chain is applied to the synthetic backscattered echoes. Table 1 lists the detailed specifications and input parameters for all the simulation cases considered in this work.

Table 1 : Simulation parameters for each run. N is the number of particles in the domain, P_n is the number of considered pulses, τ_c is the pulse duration, expressed in terms of cycle number (u, v, w) are the velocity components, d_0 is the emitter-receiver distance, γ is the angle formed by the vertical and the $E - R_1$ axis, f_{prf} is the pulse repetition frequency and Bode column indicates the nature of the simulation, either inputting the real sensors impulse response (Real) or considering infinite band sensors (Inf.).

Run (#)	N (#)	(u, v, w) m/s	d_0 (mm)	γ (rad)	f_{prf} (Hz)	P_n (#)	τ_c (#)	Bode
1	1500	(0.33, 0, 0)	0.0704	2.3512	1600	3000	2	Real
2	1500	(0.33, 0, 0)	0.0704	2.3512	1600	3000	8	Real
3	1500	(0.33, 0, 0)	0.0704	2.3512	1600	3000	2	Inf.
4	1500	(0.33, 0, 0)	0.0704	2.3512	1600	3000	8	Inf.

3. Results

f_{eff} is computed using the measured frequency responses of the sensors, and compared to the nominal frequency f_{nom} imposed in the simulations. The results are shown in Figure 2 for the case of 2 and 8 cycles.

First, there appears to be systematic overestimation as $f_{nom} < f_c$ (with f_c the central frequency of the emitter) and underestimation as $f_{nom} > f_c$ (Figure 2a). However, the magnitude of these over/underestimations is damped as the number of cycles increases, hence as the spectral width of the emitted pulses narrows. This effect is further confirmed by the horizontal velocity estimated at each prescribed nominal frequency. These velocities are calculated based on the synthetic demodulated echoes provided by the simulations (Figure 2b); these are systematically seen to be overestimated (underestimated)for nominal frequencies lower (higher) than f_c. As the effective frequency differs from the nominal frequency, the estimated velocities are offset: Figure 3a,b displays histograms of raw velocities estimated using a number of pulse-pairs of 2 for $\nu = 1.39$ MHz, for the runs 1 and 2 (Table 1). The theoretical distribution of such velocities can be obtained analytically (Fromant et al. 2024 [9]), and is seen to match the current dataset: similar autocorrelation coefficients (Fromant et al. 2024 [9]) are observed for each distribution, but those are centered around different mean velocities for the 2 cycles case and the 8 cycles case.

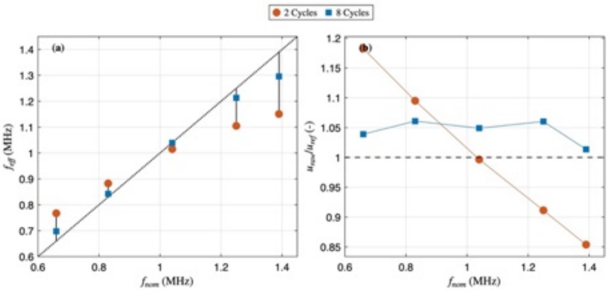

Figure 2: (a) shows the difference between the imposed nominal carrier frequency f_{nom} in the simulations and the effective carrier frequency f_{eff} from the backscattered pulses, for both 2 and 8 cycles (respectively in orange and blue). (b) shows the velocity ratio of the mean raw velocity u_{raw} estimated from the synthetic echoes and the prescribed velocity ($u_{ref} = 0.33$ m/s).

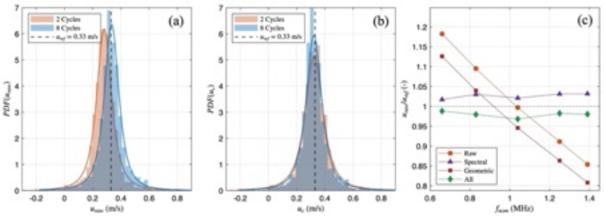

Figure 3: (a) Histograms of the raw velocity estimated from the synthetic echoes using a pulse-pair number m=2 for runs 1 ($\tau_c = 2$ cycles, in orange) and 2 ($\tau_c = 8$ cycles, in blue) ; theoretical PDFs computed estimated from the velocity autocorrelation coefficient are superimposed, as well as the prescribed velocity (black dotted vertical line), (b) Histograms of the corrected velocity estimated from the synthetic echoes using a pulse-pair number m=2 for runs 1 ($\tau_c = 2$ cycles, in orange) and 2 ($\tau_c = 8$ cycles, in blue) ; theoretical PDFs computed estimated from the corrected velocity autocorrelation coefficient are superimposed, as well as the prescribed velocity (black dotted vertical line) (c) mean velocity for each carrier frequency as a function of the applied correction (raw in orange, spectral correction only in purple, geometric correction only in brown and all corrections in green).

Finally, the correction is verified and allows to account for both spectral width and beampatterns directivity biases (Figure 3c) simultaneously, or in a decomposed fashion using the insight provided by the infinite band runs (runs 3 and 4) which by definition are unaffected by spectral broadening effects. At first order, it is shown that the velocity bias induced by the directivity beampatterns of the system can be considered constant over the bandwidth of the sensors, which simplifies the initial correction as the geometric terms in the denominator can be removed from the summation term. This leads to a single offset accounting for the geometric correction, independent on the frequency of the sensors bandwidth.

4. Conclusions

The capability of ultrasonic bistatic Doppler systems to resolve turbulent two-phase flows relies on mitigating inherent instrumental biases. The use of broadband sensors in bistatic configurations creates a discrepancy between the system's prescribed nominal frequency and the effective frequency carried by the echoes within the medium, function of the sensors frequency impulse response. In addition, these systems are subject to frequency-dependent geometric bias themselves function of the system directivity beampatterns. In the present study, a numerical experiment is proposed to assess the measurement accuracy of the quasi-instantaneous velocity and a correction method is successfully tested. Correcting spectral and geometric errors is a critical step towards unlocking the full potential of multi-frequency ACVP for high-resolution measurements of sediment transport in turbulent two-phase flows.

References

[1] Hurther, D., & Thorne, P. D. (2011). Suspension and near-bed load sediment transport processes above a migrating, sand-rippled bed under shoaling waves. *Journal of Geophysical Research: Oceans*, *116*(C7).

[2] Revil-Baudard, T., Chauchat, J., Hurther, D., & Barraud, P. A. (2015). Investigation of sheet-flow processes based on novel acoustic high-resolution velocity and concentration measurements. *Journal of Fluid Mechanics*, *767*, 1-30.

[3] Fromant, G., Mieras, R. S., Revil-Baudard, T., Puleo, J. A., Hurther, D., & Chauchat, J. (2018). On bedload and suspended load measurement performances in sheet flows using acoustic and conductivity profilers. *Journal of Geophysical Research: Earth Surface*, *123*(10), 2546-2562.

[4] Shen, C., & Lemmin, U. (1997). Ultrasonic scattering in highly turbulent clear water flow. *Ultrasonics*, *35*(1), 57-64.

[5] Lavery, A. C., Schmitt, R. W., & Stanton, T. K. (2003). High-frequency acoustic scattering from turbulent oceanic microstructure: the importance of density fluctuations. *The Journal of the Acoustical Society of America*, *114*(5), 2685-2697.

[6] Willink, R. D., & Evans, D. H. (2002). The effect of geometrical spectral broadening on the estimation of mean blood velocity using wide and narrow ultrasound beams. *IEEE transactions on biomedical engineering*, *43*(3), 238-248.

[7] Lhermitte, R., & Serafin, R. (1984). Pulse-to-pulse coherent Doppler sonar signal processing techniques. *Journal of Atmospheric and Oceanic Technology*, *1*(4), 293-308.

[8] Rolland, T. (1995). *Développement d'une instrumentation Doppler ultrasonore: application aux écoulements turbulents en hydraulique* (Doctoral dissertation, Verlag nicht ermittelbar).

[9] Fromant, G., Thorne, P. D., & Hurther, D. (2024). An examination of point-particle Lagrangian simulations for assessing time-resolved hydroacoustic particle flux measurements in sediment-laden flows. *The Journal of the Acoustical Society of America*, *155*(4), 2817-2835.

Turbulence-Particle Interactions observed from a single-frequency bistatic pulse-to-pulse coherent Doppler velocimeter

Joris Weel[1], Guillaume Fromant[2], Roeland van de Vijsel[1], Ton Hoitink[1]

[1] Hydrology and Environmental Hydraulics Group, Department of Environmental Sciences, Wageningen University & Research, Wageningen, the Netherlands.
[2] Laboratoire d'Informatique, Signal et Image de la Côte d'Opale, Université du Littoral Côte d'Opale, Calais, France.

With the aim of aiding turbulence resolved multiphase hydroacoustic flow measurement development, an oscillating grid turbulence setup was created. It is equipped with a micro-bubble generator and can host solid particles at the same time. This setup can therefore be of use in future studies of novel multiphase methods and devices. Using this setup, the current capability of a commercial single frequency bistatic pulse-to-pulse coherent Doppler velocimeter to identify turbulence modulation by solid particles was studied. To validate the acoustic measurements, a low-cost PTV system was set-up using the open source particle tracking software TracTrac. Acquisitions were performed at two turbulent regimes, $Re_g = 6075$ and $Re_g = 10125$, with known and controlled concentrations of either 30 µm micro-bubbles, 600 µm polystyrene particles or both the bubbles and particles present in the fluid. By comparing horizontal turbulent intensity profiles of these profiles this method was capable of detecting turbulence modulation qualitatively. The particles were observed to increase turbulent intensity far away from the grid, where it had decayed to low levels.

Keywords: Turbulence-Particle Interactions, ACVP, Oscillating grid turbulence

1. Introduction

Geophysical surface flows are turbulent and contain multiple phases, such as river flows where sediments on an erodible bottom are transported by hydrodynamic forcing at multiple scales. To predict sediment transport and the impacts of future extreme events, these multi-scale processes are essential to understand. One important collection of processes is turbulence-particle interactions. These interactions can for example modulate the strength of turbulence or result in non-uniform concentration distributions [1,2].

To validate findings from modelling studies on this topic, physical experiments remain essential to justify assumptions and simplifications. Gravity is an example of something that is often omitted in simulations while physical experiments indicate its importance [2,3].

Recent experimental work has mostly been conducted using Particle Tracking Velocimetry (PTV) and Particle Image Velocimetry (PIV) [2] and in earlier years using Laser Doppler Anemometry (LDA) [1]. The main shortcoming of these light-based methods is their inability to measure at high particle concentrations, where the translucency becomes too small. Hydroacoustic devices, such as Acoustic Concentration Velocity Profilers (ACVP) rely on consecutive short pulses phase coherence to estimate time-resolved multi-component velocity and concentration over a profiling range of O(10cm). These systems have originally been developed to study sediment transport, and have shown their ability to resolve the particle phase motion in energetic flow conditions (Re = O(10^4-10^5)) with high spatial (O(mm)) and temporal (O(ms)) resolutions [4,5]. They are capable of this at very high concentrations where light-based methods fail and can thus potentially extend the concentration range over which turbulence-particle interactions are observable. This is especially useful when looking at, for example, wall bounded turbulence, sediment transport and bedform behaviour in rivers, where turbulence-particle interactions or even particle-particle interactions in the highly concentrated near-bed region have been hypothesized to influence river dune dynamics [6,7].

In order to more accurately study and quantify two-phase flows and turbulence-particle interactions, the motion of both the fluid, called the carrier phase, and the particles, called the dispersed phase should be resolved. This is until present not possible using ACVP technology. However, simultaneous two-phase measurements are currently under development and this internship aims to contribute to that by creating and testing an experimental setup that can be used to develop two-phase measurements methodologies. The resulting setup was used to demonstrate the current capability of pulse-to-pulse coherent Doppler velocimeters to capture turbulence-particle interactions and enhance our understanding of these hydroacoustic particle flux measurements. To achieve this the following questions will be answered:

- What are the current limitations in using a single-frequency bistatic pulse-to-pulse coherent Doppler sonar system to track turbulence-particle interactions?
- How does the presence of 600 µm low density polystyrene particles alter turbulent conditions in an oscillating grid setup?

2. Methods

2.1 Experimental setup

The OGT-setup used for this study can be seen in figure 1, it is 45 by 45 by 75 cm and contains only the grid near the bottom. The grid has a mesh size of M = 5 cm, and follows a programmable sinusoidal motion with a stroke length (S) from 0 to 4.5 cm and frequency (f_g) range 0 to 5 Hz. The turbulent regime can be characterized by the grid Reynolds number Re_g, which is defined as:

$$Re_g = \frac{f_g S^2}{\nu} \tag{1}$$

The horizontal turbulent intensity over depth can be modelled using the following equation [8,9],

$$u'_{rms} = C M^{1/2} S^{3/2} f_g z^{-1} \tag{2}$$

Where C is a constant varying between 0.20 and 0.25 [8]. Some even indicate a wider range [10], but the lower limit is always at 0.20. Under the grid, a bubble generator is situated which forms bubbles with a mean diameter of ~ 30μm and normalized standard deviation of 0.4. See Table 1 for the characteristics of the polystyrene particles that were used.

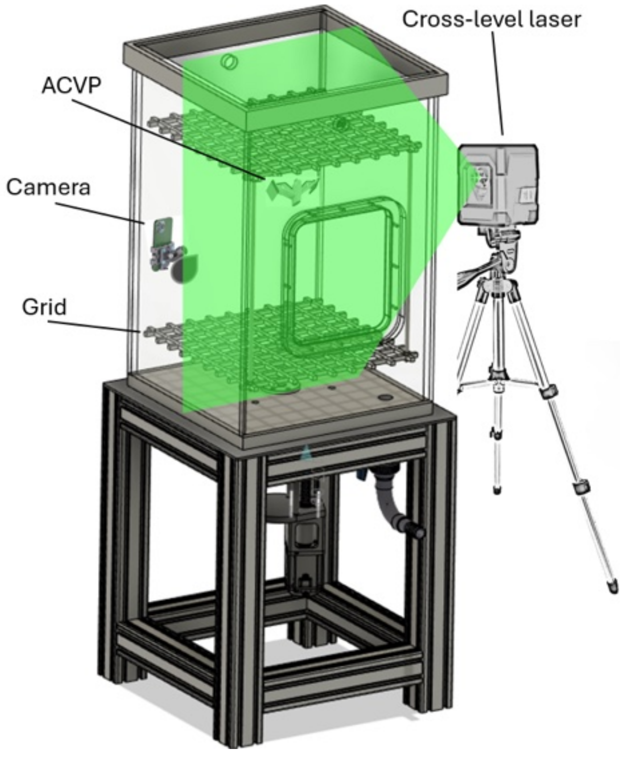

Figure 1: Experimental setup

Table 1: Polystyrene particle parameters

Parameter	Value or Range
d	600 μm
Re_p	4.2
St	0.1 - 1
d/η	1.5 - 5

2.2 ACVP

The acoustic measurements were performed using a UB-Lab3C system (Ubertone ©), with two receivers, allowing for time-resolved 2C(u,w)-velocity to be recorded over a 20 cm profile range with 2.2 mm vertical resolution. The employed device is a bistatic, single-frequency, pulse-to-pulse coherent Doppler velocimeter, centred around 1 MHz. Within the setup described above, the ACVP is mounted with the emitter 30 cm above the mean grid position. Attachment and formation of bubbles on the transducers were prevented by using small pumps and hoses to create a flow over their surface. The pulse repetition frequency is set to 1600 Hz and 64 consecutive pulses are used to produce a time-resolved velocity estimate, resulting in a temporal resolution of 25 Hz.

2.3 PTV

A low cost PTV setup [11] was developed. The setup uses a phone camera with a resolution of 1920 x 1080 at 60 fps. The phone is fixed in place on the side of the tank. A cross-level laser was placed to the side. A calibration sheet of 17 x 25 dots with 1 cm spacing was temporarily installed into the tank after it was filled. This sheet was used to align the laser, undistort the videos and made it possible to measure distances. In the videos a region of interest (ROI) was selected that corresponded to a 2 cm wide vertical profile directly below the ACVP. The open-source particle tracking software TracTrac [12] was used to detect all dispersed bubbles and particles within this ROI. The program then computed the horizontal (u) and vertical (w) velocities in pixel/frame for every particle in each frame, which was converted to m/s.

2.4 Acquisitions

The 6 tested scenarios, their turbulent regime and presence/absence of particles and/or bubbles can be seen in Table 2. The high-turbulence regime (Reg = 10125) is the highest achievable in the tank (f_g = 5 Hz and S = 4.5 cm). The low-turbulence regime (Reg = 6075) was found by taking the lowest energy where the majority of the polystyrene particles remained in suspension over time. This regime is forced by the grid oscillating at 3 Hz with the same stroke. All acquisition scenarios were performed in three consecutive 3-min repetitions. This is long enough to ensure convergence of the root-mean-square and mean velocity measurements [10].

The acquisitions were completed in the following steps:

1. The bubble generator and the oscillating grid were turned on, waited until turbulence and bubble concentration stabilize.

2. Three repetitions of scenario 1 were measured.

3. Bubble generator was turned off.

4. Monitor the decreasing backscatter intensity as the bubbles disappear.

5. Once the bubble backscatter is negligible (after roughly 10 minutes): 2 g/l of 600 μm polystyrene particles were added and the acquisitions of scenario 2 were started.

6. After completing three repetitions for scenario 2, the

bubble generator was turned back on.

7. Once the bubble generator was on for seven minutes the acquisitions for scenario 3 were started.

After draining and cleaning the tank it was refilled to repeat the same procedure at the other regime. As the bubble generator slowly raises the water temperature, all experiments started once the temperature reached 15 ◦C. Over the consecutive runs at one regime the temperature increased by 1 to 2 degrees Celsius.

Table 2: Acquisitions

Scenario	Re_g	Dispersed phase
MB-L	6075	Micro-Bubbles
P-L	6075	Particles
B-L	6075	Both
MB-H	10125	Micro-Bubbles
P-H	10125	Particles
B-H	10125	Both

3. Results

3.1 Comparing ACVP & PTV

u'_{rms} evaluated from the PTV and the ACVP systems are displayed in Fig. 2. Additionally, a dashed model line can be seen, this is the model in equation 9 with C = 0.20 and a value of 0.006 ms^{-1} added, showing that the ACVP values appears to systematically overestimate u'_{rms} compared to the model. This was anticipated, as the horizontal velocity component is affected by noise due to the geometry of the bistatic system [13]. The PTV profile has a different shape than that of the ACVP and the model, but it is in reasonable agreement with the model when close to the grid ($z/M < 1.5$). The PTV data in this plot is from the acquisitions of scenario P-H. This was done because this method has thus far been unable to detect the bubbles adequately. This is expected to be due to the weak scattering of light by the micro-bubbles and the video quality being inadequate to capture this. The ACVP data shows MB-H, as this represents the flow of the fluid, which is what the model was developed for.

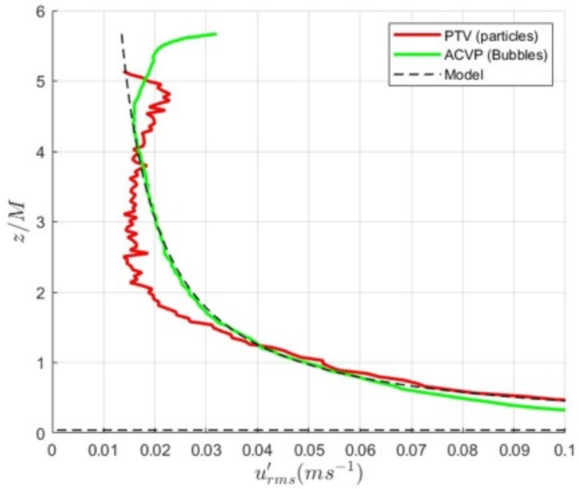

Figure 2: Comparison of horizontal turbulence intensity profiles

3.2 Turbulent intensity

Figure 3 shows u'_{rms} over depth which represents the turbulent intensity. As expected it is always higher for scenario B than for P. This is due to the small inertial lag of the particles to the forcing by the surrounding fluid. u'_{rms} is consistently highest for scenario B and at highly turbulent conditions ($u'_{rms} > 0.015$ ms^{-1}), scenario P results in lower turbulent intensity than scenario MB. However, where the u'_{rms} decreases to below 0.015 ms^{-1}, u'_{rms} of P becomes greater than that of MB. This is visible in both the high and low regime plots as the profile P rises faster than the profile MB and overtakes it at $u'_{rms} \approx 0.015$ ms^{-1} . On top of that, slightly closer to the grid, when $u'_{rms} \approx 0.018$ ms^{-1} the lines of B and MB start diverging from one another when moving upwards through the profile to the lower intensities. With the turbulent intensity decreasing faster when only bubbles are present.

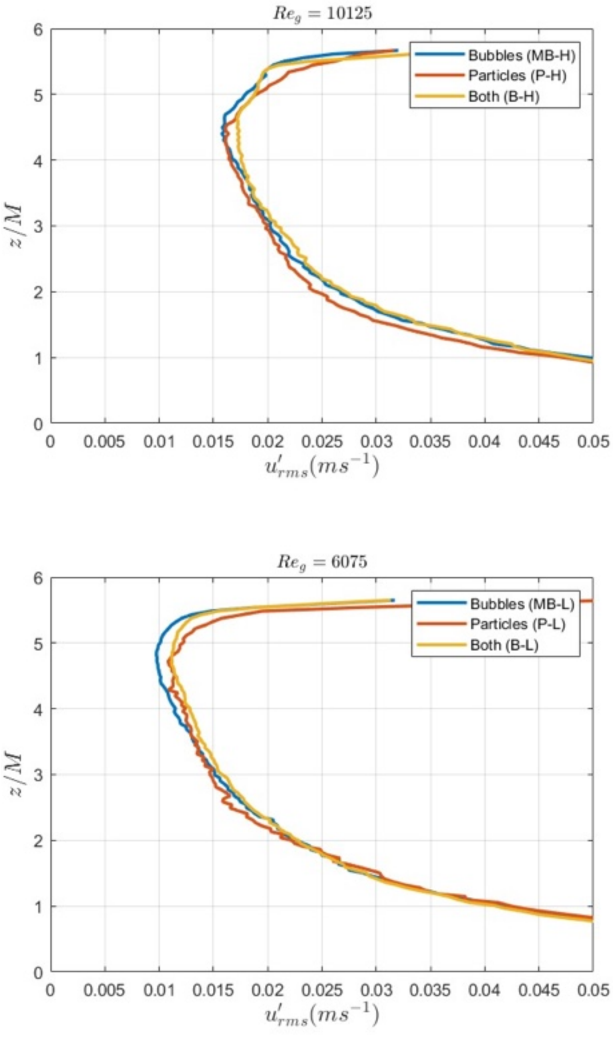

Figure 3: Horizontal turbulent intensities separated by turbulent regime, lines show acquisitions with different dispersed phases present

4. Discussion

Our results indicate that the presence of particles results in an increase in turbulent intensity. This is especially apparent in low turbulence conditions far away from the grid. This observation is supported by previous work where the effects of particles with similar St and d/η on grid generated turbulence were studied [3]. In this work it was observed that the particles generate turbulence, but this was only apparent far from the grid, where the turbulence had sufficiently decayed. The increase in turbulent energy would however be at the scale of the particle, which is unfortunately not resolved by the ACVP as it can only go as far as the Taylor micro-scale. It has been hypothesized that redistribution of energy through the turbulent scales could be responsible for an increase at the larger scales [3]. In our case, the fact that it only becomes visible at low turbulence could be because under energetic conditions the particle lag reduces the apparent turbulent intensity more strongly than wake shedding increases it. But in low-intensity turbulence this balance may be reversed. Although our observations are confirmed by earlier work the absolute differences are small and the effects have only been observed in grid generated turbulence. As noted by others [1], grid generated turbulence decays to low levels, which makes any difference to that turbulence seem significant. Flume experiments in shear flows with similar turbulent intensities could be performed to attempt to confirm the observed turbulence particle interactions in a different setting and study them further.

When both dispersed phases are present, the apparent velocity is a mixture of the velocity of both phases. With a non-linear contribution depending on the particle scattering properties and relative concentration of the phases and the potential presence of sound-scattering turbulent microstructures [14]. This prevents resolving the motion of the micro-bubbles when particles are present and thus quantification of the turbulence modulation strength is not possible. By applying multifrequency methods this problem could be solved by separating the velocities of both phases.

5. Conclusion

We have shown the capability of single frequency ACVPs to qualitatively identify turbulence modulation by lightweight polystyrene particles. In a series of lab experiments we have resolved the motion of the unladen fluid and that of particles in suspension. Comparing their second order turbulence statistics to those of the mixed signal when both dispersed phases are present, allows for identification of turbulence modulation. Using this method we have found a turbulence increase due to the particles, especially far above the grid, where turbulence intensity has decayed significantly. This observation is in agreement with earlier observations by Poelma et al. (2007) on particles with similar values of St and d/η. However, in order to quantify the modulation strength, two-phase turbulence resolved measurements are needed.

References

[1] Balachandar, S., Eaton, J. K., Jan. 2010. Turbulent dis persed multiphase flow. Annual Review of Fluid Me chanics 42 (1), 111–133.

[2] Brandt, L., Coletti, F., Jan. 2022. Particle-laden turbulence: Progress and perspectives. Annual Review of Fluid Me chanics 54 (1), 159–189.

[3] Poelma, C., Westerweel, J., Ooms, G., Oct. 2007. Particle fluid interactions in grid-generated turbulence. Journal of Fluid Mechanics 589, 315–351.

[4] Hurther, D., Thorne, P. D., Bricault, M., Lemmin, U., Barnoud, J.-M., Jul. 2011. A multi-frequency acous tic concentration and velocity profiler (acvp) for bound ary layer measurements of fine-scale flow and sediment transport processes. Coastal Engineering 58 (7), 594 605.

[5] Fromant, G., Mieras, R. S., RevilBaudard, T., Puleo, J. A., Hurther, D., Chauchat, J., Oct. 2018. On bedload and sus pended load measurement performances in sheet flows using acoustic and conductivity profilers. Journal of Geo physical Research: Earth Surface 123 (10), 2546–2562.

[6] Lange, S. I. d., van de Vijsel, R. C., Torfs, P. J. J. F., Waller stein, N. P., Hoitink, A. J. F., Jul. 2025. Bimodality in subaqueous dune height suggests flickering behavior at high flow. Nature Communications 16 (1).

[7] Revil-Baudard, T., Chauchat, J., Hurther, D., Barraud, P.-A., Feb. 2015. Investigation of sheet-flow processes based on novel acoustic high-resolution velocity and con centration measurements. Journal of Fluid Mechanics 767, 1–30.

[8] Poulain-Zarcos, M., Mercier, M. J., ter Halle, A., May 2022. Global characterization of oscillating grid turbu lence in homogeneous and two-layer fluids, and its impli cation for mixing at high peclet number. Physical Review Fluids 7 (5), 054606.

[9] Hopfinger, E. J., Toly, J.-A., Nov. 1976. Spatially decaying turbulence and its relation to mixing across density inter faces. Journal of Fluid Mechanics 78 (1), 155–175.

[10] McCorquodale, M. W., Munro, R. J., Nov. 2018. A method for reducing mean flow in oscillating-grid turbulence. Experiments in Fluids 59 (12).

[11] Smerdon, A., van der A, D., ODonoghue, T., Nov. 2022. Piv for peanuts- a low cost particle image velocimetry systemto observe terminal velocity in suspensions.

[12] Heyman, J., Jul. 2019. Tractrac: A fast multi-object track ing algorithm for motion estimation. Computers and Geosciences 128, 11–18.

[13] Hurther, D., Lemmin, U., Mar. 2001. A correction method for turbulence measurements with a 3d acoustic doppler velocity profiler. Journal of Atmospheric and Oceanic Technology 18 (3), 446–458.

[14] Shen, C., Lemmin, U., Feb. 1997. Ultrasonic scattering in highly turbulent clear water flow. Ultrasonics 35 (1), 57 64.

15th International Symposium on Ultrasonic Doppler Methods for Fluid Mechanics and Fluid Engineering
LEGI, Univ. Grenoble Alpes, France (3.-7. May 2026)

Pulse-coherent Doppler velocity profile measurements in turbulent open-channel flows with a novel wideband multi-bistatic ADVP: contribution & correction of spectral broadening, directivity & Doppler noise effects

Oriana Yon-Campaner[1*], Maxime Lernould[2], Pierre-Alain Barraud[3], Guillaume Fromant[2], David Hurther[1]

[1] Lab. of Geophysical & Industrial Flows (LEGI), Univ. Grenoble Alpes / CNRS, 1009 rue de la Piscine, 38041 Saint-Martin d'Hères, France. *oriana.yon-campaner@univ-grenoble-alpes.fr
[2] LISIC, Univ. du Littoral Côte d'Opale, 62228 Calais, France.
[3] TIMC, Univ. Grenoble Alpes, 38000 Grenoble, France.

Acoustic Concentration and Velocity Profilers (ACVPs) are multi-bistatic systems enabling simultaneous profiling of turbulent flow velocity and suspended sediment concentration. In high-concentration or near-bed flows, however, two systematic velocity biases compromise measurement accuracy. The first, a directivity bias, arises from the pressure-weighted centroid of the sampling volume deviating from the emitter axis by a frequency-dependent angle β_k, causing overestimation of the horizontal velocity component by up to 10% near the bed. The second, a spectral broadening bias, results from the use of short acoustic pulses: the broadened pulse spectrum shifts the effective acoustic frequency f_{eff} away from the nominal carrier f_0, inducing velocity errors of 10–20%. Both biases propagate into second-order turbulent statistics, including turbulence intensity $\langle u'^2 \rangle$ and Reynolds shear stress $\langle u'w' \rangle$. We present analytical corrections for both biases and validate them using controlled laboratory experiments with a five-frequency ACVP system operating between 0.66 and 1.39 MHz. The corrected velocity profiles and turbulent statistics show strong agreement with reference measurements, demonstrating that turbulent characterization is achievable with a multi-frequency system with appropriate signal processing.

Keywords: Acoustic Doppler velocimetry, ACVP, bistatic geometry, velocity bias correction, spectral broadening, turbulent statistics, sediment-laden flows

1. Introduction

Sediment transport in fluvial and coastal environments is a primary driver of geomorphological evolution and the regulation of nutrient and pollutant fluxes. Despite its importance, the accurate prediction of sediment transport rates, particularly under energetic regimes, remains constrained by a significant scientific bottleneck: the lack of experimental two-phase flow datasets. Historically, transport models and measurement techniques have relied on single-phase mixture theory [1,2] or mixture-flow measurements [3,4,5,6], which assume that particles follow fluid parcels without inertial lag, except for gravitational settling. Recent advances in two-phase fluid-particle modeling [7,8,9] have highlighted the necessity of accounting for complex two-way and four-way couplings. As discussed by Finn and Li [10], these interactions, such as particle lag velocity and turbulence modulation, are crucial for understanding sediment-laden flows. However, the development of these numerical perspectives has outpaced the available measurement systems capable of resolving such interactions.

In this study, a novel wide-band (also called broadband or multifrequency, below) ACVP system capable to operate at multiple time-resolved ultrasound frequencies is described for future turbulence-resolved two-phase flow measurements. Acoustic Concentration and Velocity Profilers (ACVPs) combine multi-bistatic ADVP technology (Rolland and Lemmin 1994) with multi-frequency ABS technology in a single versatile sonar system. This combination allows for simultaneous profiling of flow velocity and suspended sediment concentration in highly turbulent, clear-water and sediment-laden flows [11,12,13]. They are particularly suited for process studies of bottom benthic Boundary Layer dynamics in energetic river, estuarine and coastal flows (high Shield number flows) where sediment transport rates (as sediment fluxes) result from net mean current, net wave-driven and net turbulence-driven transport flow-rate.

However, operating broadband ultrasonic Doppler sonars at multiple frequencies introduces complex broadband measurement biases arising from the sensor and electronic hardware properties and the short-pulse transmission model required for high-resolution measurements. This study characterizes and corrects the systematic errors inherent to the multi-bistatic ADVP system as part of our ACVP technology, operating in the MHz range. Two dominant sources of bias are identified: (1) the transducer directivity beampatterns, and (2) the spectral broadening of emitted pulses induced by the emission of short duration pulses required for high-resolution profiling of turbulent velocity microscales.

Results demonstrate that geometric directivity effects induce a significant systematic bias (also called parallax error in the literature) of the mean streamwise velocity near the bed, while the vertical velocity component remains unaffected. Additionally, spectral broadening of the pulse spectra causes a frequency-dependent shift in the effective ultrasound carrier frequency, leading to velocity underestimation at higher frequencies.

Regarding turbulent quantities, frequency-induced biases in the mean velocity of up to 10–20% propagate non-linearly into second-order statistics. This leads to significant errors in the estimated turbulent intensity and also in Reynolds shear stress profiles (unaffected by Doppler noise effects), rendering multifrequency turbulence characterization unreliable without prior correction. The integrated correction methodology proposed here yields a unified turbulent quantity estimates across the acoustic frequency range of the system and address a methodology to decrease the Doppler noise Reynolds normal stress profiling with wideband ADVPs.

2. Theory

2.1 Bistatic Geometry and Directivity Bias

The multi-bistatic ACVP system features a symmetrical geometry consisting of a central cylindrical emitter (radius a_0) and two rectangular receivers (Fig. 1a) designed to optimize the overlap between emission and reception beams [14].

The spatial sensitivity of the system is described by a directivity function $D(\vec{p}, f)$, defined as the root-mean-square product of the emitter and receiver directivity functions evaluated at particle position $\vec{p}$ [15,16,17]. This function weights scattered echo amplitudes and defines the measurement volume at each range gate r. A key consequence is that the pressure barycenter of the measurement volume drifts away from the emitter's vertical axis by a frequency and range-dependent angle β_k. Despite remaining below 1°, this drift introduces systematic horizontal velocity biases of up to ~10%.

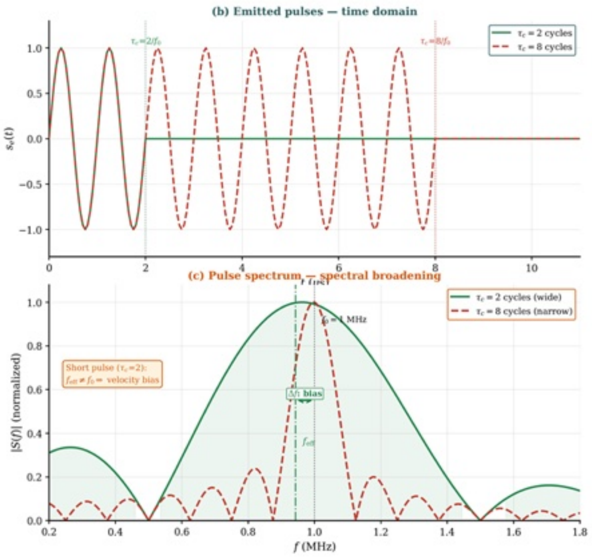

Figure 1: (a) Bistatic ACVP geometry showing the emitter E, receiver R, nominal bisector angle α, directivity deviation angle β, and effective bisector angle α'. F and F' denote the pressure-centroid of the sampling volume at nominal and shifted positions, respectively. (b) Time-domain emitted pulses for τ_c = 2 cycles (short, broadband) and τ_c = 8 cycles (long, narrowband). (c) Corresponding normalized spectra |S(f)|: the short pulse yields a wide spectrum whose centroid f_{eff} shifts away from the nominal carrier frequency f_0 by Δf, introducing the spectral broadening velocity bias.

2.2 Spectral Broadening Bias

Short pulse durations (τ_c = 2 cycles) are required for high spatial resolution but produce a broadened frequency spectrum (Fig. 1b,c). Each spectral component of the emitted signal produces a Doppler shift, weighted by the combined frequency response of the pulse, emitter, and receivers through a coefficient $h(n)$. The measured Doppler frequencies are therefore expressed as a weighted spectral centroid which simultaneously accounts for directivity and spectral broadening effects. This also yield to an effective frequency $f_{eff} \neq f_0$, used for a simplified expression.

2.3 Doppler noise contribution & reduction in turbulent Reynolds normal stress profile

The velocity biases introduced by directivity and spectral broadening effects (Section 2.2) do not only affect mean velocity estimates, but also propagate into higher-order turbulent statistics. Since turbulent quantities such as intensities, $\langle u'^2 \rangle$ and $\langle w'^2 \rangle$, and shear stress $\langle u'w' \rangle$, are derived from velocity fluctuations, any systematic or random bias in the instantaneous velocity reconstruction will directly impact their estimates.

Furthermore, Doppler noise, arising from the finite number of scatterers within the measurement volume, adds a broadband random error floor to the velocity estimates. This noise component directly adds the physical velocity variance, leading to an overestimation of turbulent intensities if left uncorrected (Garbini [18], Hurther and Lemmin [14]). In this study we apply the dual frequency noise reduction method proposed by Hurther and Lemmin [20]. By selecting two distinct operating frequencies and calculating the cross-correlation between the datasets, we can effectively suppress the uncorrelated noise inherent to each signal while preserving the physical velocity fluctuations. In comparing this dual-frequency cross-correlation approach to the method proposed by Garbini [18] our results indicate that the current technique provides velocity estimates with higher turbulence resolution and a reduced noise floor.

Together, these corrections ensure that the velocity fields reconstructed provide a reliable basis for the estimation of turbulent quantities, minimizing both systematic and random error contributions across the measured velocity profiles.

3. Experimental Setup

Experiments were conducted in a 10 m tilting flume (0.36 m wide) using an immobile bed of PMMA particles with uniform flow conditions and a Reynolds number of $Re = 2.10^4$. Vertical velocity profiles were collected using an ACVP mounted in a vacuum box to minimize free-surface interference. To ensure high-quality acoustic backscatter, micro-air bubbles ($d \approx 50\,\mu m$) were introduced as near-perfect fluid tracers ($St \ll 1$). The ACVP operated across five nominal frequencies (0.66 to 1.39 MHz, Table 1) using a multi-frequency pulsing scheme, with 10-minute acquisition periods subdivided to optimize signal gain and spatial resolution across the 0.15 m measurement depth.

Table 1: Parameters imposed for each nominal frequency (f_0), including the Pulse Repetition Frequency (PRF) in Hz, the number of gates in the profiles, the gain in dB and the time resolution of each gate in µs.

Nominal emitted frequency (f_0)	Pulse repetition frequency	Gates number	Gain	Time resolution
MHz	Hz	-	dB	µs
0.66	1600.7171	88	84	3.04
0.83	1602.5641	117	82	2.40
1.04	1600.0000	144	82	1.92
1.25	1602.5641	183	88	1.60
1.39	1600.0000	212	90	1.44

4. Results

4.1 Characterization of Directivity and Spectral Biases

The study compared two operational modes: a high-resolution mode (2-cycle pulses) and a narrow-bandwidth mode (8-cycle pulses). Initial findings revealed that raw streamwise velocity measurements exhibit systematic deviations from the reference velocity, taken at 1MHz, largely driven by the transducer's finite bandwidth. For short pulses, these errors were most pronounced, showing an overestimation of 20% at the lower frequency bound (0.66 MHz) and an underestimation of 15% at the upper bound (1.39 MHz). While longer pulses moderated these discrepancies, the consistent frequency-dependent decay confirmed that raw estimates are mostly influenced by the transducer's Bode curves.

4.2 Evaluation of Correction Methodologies

Two correction strategies were implemented to reconcile the multifrequency datasets. A spectral-only correction model, which accounts for pulse duration and filtering, successfully reduced the frequency dependence but proved insufficient for absolute accuracy, leaving residual errors of 3% to 8% at the bandwidth extremes. To address this, a combined spectral-directivity correction was applied, which weights each frequency component by its specific directivity pattern. Experimental results showed similar success as numerical model, reducing errors to approximately 0.5% for short pulses and demonstrating that integrating spatial sensitivity with spectral analysis is essential for unbiased velocimetry.

4.3 Development of a Simplified Operational Model

A correction of the vertical and horizontal Doppler velocity profile has been proposed and a comparative analysis showed that systematic errors of less than 1% can be obtained from simulations. This indicates that the complex interplay between directivity and spectral broadening can be effectively corrected. Vertical profiles validated this efficiency; while raw data was highly dispersed, the corrected profiles collapsed into a single consistent curve, maintaining a relative error below 3% over the entire mean velocity profile, except in the high-gradient region subject to spatial averaging effects in the near-wall flow region.

4.3 Turbulent Statistics

The bias corrections are applied to each velocity component independently. For turbulence intensities (square root of Reynolds normal stress divided by water density), the multiplicative nature of both biases leads to added quadratic amplification in $\langle u'^2 \rangle$ and $\langle w'^2 \rangle$. After correction by cross-correlation estimations instead of auto-correlation estimates, intensity profiles for all 5 ultrasound frequencies of $u_{rms}/\,u_*$ and $w_{rms}/\,u_*$ collapse onto the Nezu and Nakagawa [19] laws. Furthermore, the Reynolds shear stress $-\langle u_c' w_c' \rangle$ corrected for the systematic errors (Doppler noise contribution being negligible by essence), recovers the expected linear profile with $u_*^2 \approx 2.3 \times 10^{-4}\, m^2/s^2$ at the bed.

5. Summary

Two systematic velocity biases affecting wideband multi-bistatic ACVP measurements have been identified and analytically corrected: (1) a directivity bias arising from near-field pressure centroid drift from its theoretical position, assumed along the emitter axis (up to 10% near the bed), and (2) a spectral broadening bias induced by short pulse emission mode (10–20% depending on frequency) for high-resolution velocity profiling. Both biases were found to propagate non-linearly into first order velocity moment but also into second-order turbulent velocity statistics. The proposed corrections applied to five ultrasound frequencies (0.66–1.39 MHz) for wideband ADVP measurements, reduce residual errors to below 5%, enabling reliable turbulence-resolved velocity profiling in high Reynolds number open-channel flows. Moreover, the use of a dual-frequency Doppler noise reduction method (Hurther and Lemmin [20]) compared to a standard increases Doppler noise considerably, thanks to the bias corrected dataset.

References

[1] Guo, J., & Julien, P. Y. (2001). Turbulent velocity profiles in sediment-laden flows. *Journal of Hydraulic Research*, *39*(1), 11-23.

[2] McTigue, D. F. (1981). Mixture theory for suspended sediment transport. *Journal of the Hydraulics Division*, *107*(6), 659-673.

[3] Guta, H., Hurther, D., & Chauchat, J. (2022). Bedload and

concentration effects on turbulent suspension properties in heavy particle sheet flows. *Journal of Hydraulic Engineering*, *148*(7), 04022012.

[4] Guta, H., Hurther, D., & Chauchat, J. (2024). Turbulent kinetic energy budget of sediment-laden open-channel flows: bedload-induced wall-roughness similarity. *Journal of Fluid Mechanics*, *987*, A25.

[5] Revil-Baudard, T., Chauchat, J., Hurther, D., & Barraud, P. A. (2015). Investigation of sheet-flow processes based on novel acoustic high-resolution velocity and concentration measurements. *Journal of Fluid Mechanics*, *767*, 1-30.

[6] Revil-Baudard, T., Chauchat, J., Hurther, D., & Eiff, O. (2016). Turbulence modifications induced by the bed mobility in intense sediment-laden flows. *Journal of Fluid Mechanics*, *808*, 469-484.

[7] Cheng, Z., Hsu, T. J., & Chauchat, J. (2018). An Eulerian two-phase model for steady sheet flow using large-eddy simulation methodology. *Advances in Water Resources*, *111*, 205-223.

[8] Mathieu, A., Cheng, Z., Chauchat, J., Bonamy, C., & Hsu, T. J. (2022). Numerical investigation of unsteady effects in oscillatory sheet flows. *Journal of Fluid Mechanics*, *943*, A7.

[9] Salimi-Tarazouj, A., Hsu, T. J., Traykovski, P., Cheng, Z., & Chauchat, J. (2021). A numerical study of onshore ripple migration using a Eulerian two-phase model. *Journal of Geophysical Research: Oceans*, *126*(2), e2020JC016773.

[10] Finn, J. R., & Li, M. (2016). Regimes of sediment-turbulence interaction and guidelines for simulating the multiphase bottom boundary layer. *International Journal of Multiphase Flow*, *85*, 278-283.

[11] Hurther, D., & Lemmin, U. (1998). A constant-beam-width transducer for 3D acoustic Doppler profile measurements in open-channel flows. Measurement Science and Technology, 9(10), 1706–1714. https://doi.org/10.1088/0957-0233/9/10/010

[12] Fromant, G., Mieras, R. S., Revil-Baudard, T., Puleo, J. A., Hurther, D., & Chauchat, J. (2018). On Bedload and Suspended Load Measurement Performances in Sheet Flows Using Acoustic and Conductivity Profilers. Journal of Geophysical Research: Earth Surface, 123(10), 2546–2562. https://doi.org/10.1029/2017JF004560

[13] Thorne PD & Hanes DM: A review of acoustic measurement of small-scale sediment processes, Cont. Shelf Res. 22 (2002), 603–632.

[14] Hurther, D., & Lemmin, U. (2001). A Correction Method for Turbulence Measurements with a 3D Acoustic Doppler Velocity Profiler. Journal of Atmospheric and Oceanic Technology, 18(3), 446–458.https://doi.org/10.1175/1520-0426(2001)018%3C0446:ACMFTM%3E2.0.CO;2

[15] Fromant, G., Thorne, P. D., & Hurther, D. (2024). An examination of point-particle Lagrangian simulations for assessing time-resolved hydroacoustic particle flux measurements in sediment-laden flows. The Journal of the Acoustical Society of America, 155(4), 2817–2835. https://doi.org/10.1121/10.0025766

[16] Moore, S. A., & Hay, A. E. (2009). Angular scattering of sound from solid particles in turbulent suspension. *The Journal of the Acoustical Society of America*, *126*(3), 1046-1056.

[17] Simmonds, J., & MacLennan, D. N. (2008). *Fisheries acoustics: theory and practice*. John Wiley & Sons.

[18] Garbini, J. L., Forster, F. K., & Jorgensen, J. E. (1982). Measurement of fluid turbulence based on pulsed ultrasound techniques. Part 2. Experimental investigation. *Journal of Fluid Mechanics*, *118*, 471-505.

[19] Nezu, I., & Nakagawa, H. (1995). Turbulence measurements in unsteady free-surface flows. *Flow measurement and instrumentation*, *6*(1), 49-59.

[20] Hurther D**.**, & Lemmin U., (2008). Improved turbulence profiling with field adapted Acoustic Doppler Velocimeters using a bi-frequency Doppler noise suppression method. *J. of Atmos. and Oceanic Technol*. 25 (2), 452-463.

Investigation of uncertainty from parallax bias in high-resolving Acoustic Doppler Velocimetry Profiling

Marie Burckbuchler[1,2], Stéphane Fischer[1], Markus Noack[2], Nils Rüther[3]

[1] UBERTONE S.A.S., 8A rue principale, Schiltigheim, France.
[2] Karlsruhe University of Applied Science, Karlsruhe, Germany.
[3] Technical University of Munich, Germany.

For detailed studies on hydraulics, a precise and versatile instrumentation suitable for both hydraulic laboratory research and field measurements is required. Therefore, ADVP (Acoustic Doppler Velocity Profiler) techniques provide valuable answers as it allows the measurement of instantaneous colocalised multi-component velocity profiles and suspended sediment concentration (SSC). As for any measurement technique, the mastering of the uncertainties is a must for any scientifically-based interpretation of collected data and requires an in-depth investigation and quantification. This study aims to close these knowledge gaps allowing the systematic pre-determination of uncertainties for users of ADVP instruments. In this abstract, the focus is on one source of uncertainty: the parallax bias. The development of an experimental test bench prototype is presented. And first results of numerical simulation and of experimental measurements show great potential for the purpose of this study.

Keywords: Acoustic Doppler Velocimetry Profiling (ADVP), quantification of uncertainty, Acoustic beam simulation, Acoustic field measurement, Directivity

1. Introduction

For hydraulics in general but also for the study of geomorphological processes in river systems—which have become a hot topic in light of current environmental challenges such as extreme events—there is a growing need for precise and versatile instrumentation suitable for both hydraulic laboratory and field research. More and more research applications arise, which are using the bistatic ADVP (Acoustic Doppler Velocity Profiler) technique, as it allows the measurement of instantaneous colocalised multi-component velocity profiles and suspended sediment concentration [1].

[2] lists uncertainty sources inherent to the complexity of ultrasound scattering processes. They propose an initial model to simulate the processes of hydroacoustic diffusion happening with high-resolution profiling instrumentation such as ADVP , ACVP , UVP , ADV or ABS ([3], [4], [1]). This tool is planned to be developed further to evaluate the contributions of uncertainties over the whole ultrasonic measurement chain.

Following researchers' feedback and multiple preliminary studies by the company Ubertone (France) two main and relevant uncertainty sources remain unsolved for ADVP measurements. First, the hydraulic perturbation due to the transducer holder, which has to be in contact with the flowing water, and second, the parallax bias due to directivity issues and transducer manufacturing specifications. These uncertainties were already pointed out for the single point ADV and short range ADVP instruments ([5], [6]). In this abstract, we present the early stages of the study on the parallax bias.

2. Material and methods

2.1 The ADVP technology

The ADVP refers to an ADV with a profiling capability [7]. It includes one emitter and at least 2 wide beam receivers that sample the signal over a measurement line to get instantaneous 2-component or 3-component velocity profile measurements.

The system uses piezoelectric transducers to convert electrical signals into acoustic pulses and back. The emitter (Tr0) uses a circular piezoelectric element to produce a narrow beam, while the receivers (Tr1...4) utilise rectangular piezoelectric elements to provide a wide opening angle, ensuring the beams intersect across a large measurement window.

The transducers are held in a specific configuration by a holder which is referred to as the head. The geometric parameters of the head are visualised in Figure 1 including:

- d_0 the distance between the center of the emitter and the center of the receiver (in m)
- gamma the angle from the axis of the emitter to the segment d_0
- AlphaS the angle between the axis of the emitter and the central axis of the receiver

To simplify the following explanations, we will concentrate on the two receivers case. All three transducers are set up in one plane, and the beams of the emitter and the receivers must intersect. Geometric parameters of the head are shown in Fig 1.: d_0 is the distance between the center of the emitter and the center of the receiver, gamma is the angle from the axis of the emitter to the segment d_0, AlphaS is the angle between the axis of the emitter and the central axis of the receiver.

Figure 1: Current standard head geometry at Ubertone (emitter transducer in green, receivers transducers in yellow).

After pulse emission by Tr_0, the system switches to receiving mode via Tr_1 and Tr_2. As the wave propagates at sound speed c, particles (scatterers) intercept the beam and diffuse echoes back to the receivers. The time-of-flight t_j defines the position of a measurement cell dj along the emission axis. Due to the bistatic geometry, the intercell distance along the emitting axis is non-constant.

The continuous backscattered signal is sampled periodically, where each sample represents the sum of echoes from all scatterers within a specific cell j. The measurement cells are distributed along the narrow (green) beam constituting the profile.

The acoustic scatterers, moving with the liquid flow, will induce a frequency shift in the scattered signal called the Doppler shift f_D. The instrument sends n_{ech} pulses in the medium with a given PRF. In each cell of the profile j, the information obtained from the scattered n_{ech} pulses, received by the transducer Tr_i is used by the instrument to estimate a Doppler shift f_{Dij}. This shift is directly linked to V_{ij}, the sum of two projections of the 2C velocity vector: onto the emitter axis $\overline{e_e}$ and over the direction $\overline{e_{rij}}$ of the echoes from the cell towards the receiver Tr_i ($i \in \{1,2\}$).

$$f_{Dij} = \frac{f_0}{c} \cdot \overline{V_j} \cdot \left(\overline{e_{rij}} - \overline{e_e}\right) \tag{1}$$

$$V_{i,j} = \frac{c \cdot f_{Dij}}{f_0} = \overline{V_j} \cdot \left(\overline{e_{rij}} - \overline{e_e}\right) \tag{2}$$

with:

$V_{i,j}$: velocity component measured with Tr_i at the cell j
V_j: norm of the projection of the 3 component velocity vector in the (x,z) plane [m/s],
c: sound speed in the medium [m/s],
$f_{D,i,j}$: Doppler frequency [Hz],
f_0: carrier frequency [Hz].
$\alpha_{i,j}$: Doppler angle for Tr_i at the cell j

The precision of measurement of the Doppler velocities based on the Doppler frequency estimation is 0.2 to 1% on Ubertone's instruments [8].

The components u_j and w_j in the orthonormal coordinate system $\left(\overline{e_u}, \overline{e_w}\right)$ can be then calculated, and represented in Fig. 2:

$$u_j = \frac{V_{2j} - V_{1j}}{2 \sin \alpha_j} \tag{3}$$

$$w_j = \frac{V_{1j} + V_{2j}}{2\left(1 + \cos \alpha_j\right)} \tag{4}$$

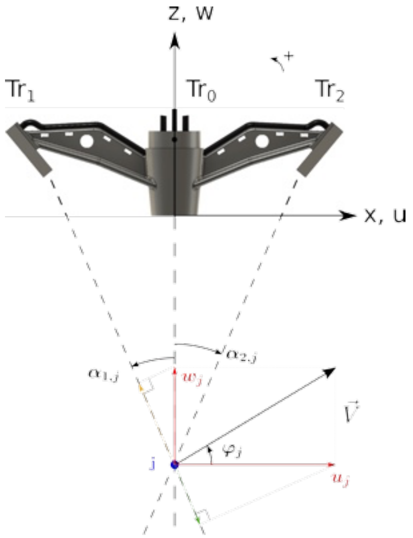

Figure 2: Schematic description of the projections of the velocity vector

2.1 Transducer and acoustic beam

The transducers are characterised by their central frequency and piezoelectric element surface dimension.

The actual acoustic beam is shaped by a diffraction phenomenon that can be described by a Rayleigh integral [9].

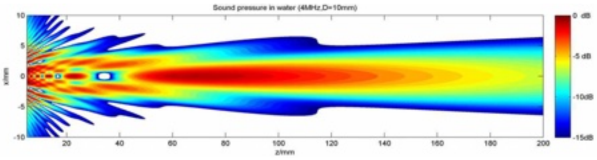

Figure 3: Detailed beam shape simulation for 4MHz emission and piezoelectric element of 10mm diameter

Based on this integral, Figure 3 shows a numerical modelisation of the sound pressure in water in front of a circular transducer of emission frequency 4 MHz, and active diameter of 10 mm.

2.3 Directivity and parallax bias

One of the most important intrinsic acoustic sources of errors of this measuring technique comes from the effects of directivity inducing a parallax bias. This issue was already introduced in the thesis of [10] and has been strongly observed on the Nortek Vectrino II ADV profiler in [6]. Indeed, the measurement volumes of both emitter-receiver pairs are not perfectly superimposed, due to the particular shape of the measurement cells. Additionally, the barycenters (or center of energy) of the cells of each emitter-receiver pair are deviating from the emitting axis with distance to the transducers, due to the actual shape of the emitting beam.

The emitted pulse is characterised by a number of periods n_{em} and a length ct_{em}, which defines thus a cell thickness r_{em}.

The measurement cell is the area situated between two ellipses sharing the same foci, placed at the center of the emitter and the receiver transducer (i.e. segment d_0). The major axis length of the first ellipse is equal to the distance of flight between the emitter, the beginning of the measuring cell and the receiver, and for the second ellipse, between the emitter, the end of the cell and the receiver. The pulse length ct_{em} corresponds to the difference between the major axes of both ellipses.

The illustration in Figure 4 depicts two pairs of ellipses (i.e. two measurement cells).

The cell thickness decreases slightly along the depth and converges toward $ct_{em}/2$.

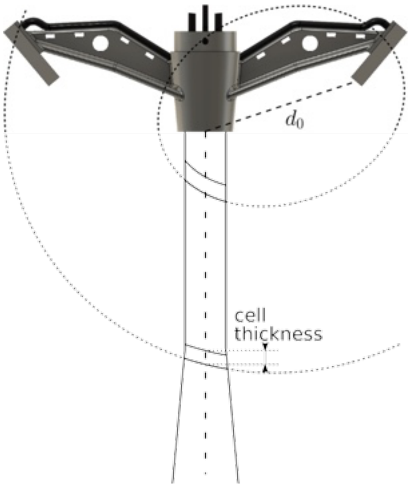

Figure 4: Representation of the bistatic cell thickness.

Furthermore, considering the above description of the acoustic beam, the field of energy is in reality not homogeneously distributed over the entire cell volume. This impact has already been assessed by the company Ubertone for the first generation of transducer holder geometry and another geometry used by the community (Figure 5), indicating an error in the measured velocity exceeding 5% or even 30% depending on geometry.

Thus, the geometry was optimised by using this preliminary basic model reflecting the parallax bias, leading to a bias of less than 1% over 30cm, with: d_0*=100mm, Gamma=120°, AlphaS=25°.*

The parallax bias is intrinsic to the bistatic measurement technique and highly influenced by the geometry (*d_0, gamma, alphas*) of the transducer head and of the transducers' characteristics (frequency, active diameter and manufacturing quality). Therefore, it is obvious that any modification to the transducer head parameters has to be characterised in terms of parallax bias. Furthermore, the directivity of the transducers also needs to be mastered and characterised.

2.4 Numerical simulation

A first simulation model was established, using the Fraunhofer approximation of the beam section for an emitter and receiver couple, to weigh the velocity component contributions within each volume.

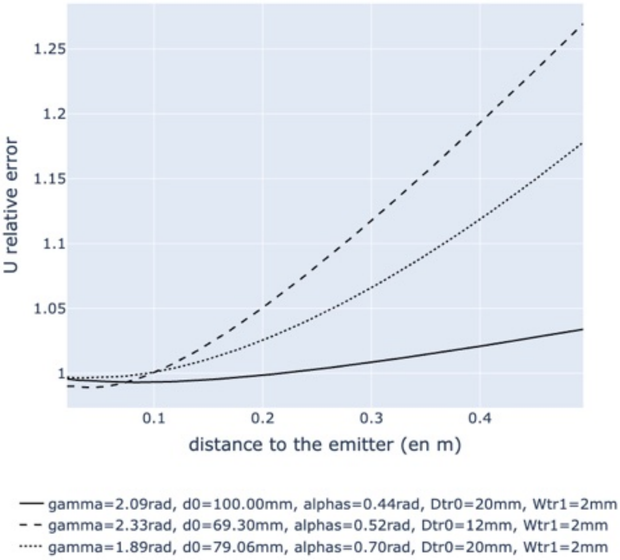

Figure 5: Simulation of parallax bias at 1MHz, 0.001m resolution on the emitter axis,

This model is waiting for the results of the experimental measurement to be either validated or improved.

2.4 Experimental setup

An experimental characterisation bench is developed to map the actual beams of the used transducers. As of today, there is no plug-and-play commercial solution, and the existing solutions work only with non-open source softwares. Moudjed (2013, [9]) presents results from such a bench, which is and will be a good reference for our current work. Nevertheless, one transducer energy field needed about 150 hours to be scanned, and the many trials affected the transducer's efficiency.

Our bench should in the end be able to map any complete bistatic head's energy field, based on open-source libraries, with an absolute positioning uncertainty of less than 1mm. And one of the differences with [9] is that we are looking for the energy field in the transducer's coordinate system, to be able to assess the alignment of the transducer's body with the acoustic axis. Thus the accuracy of the target's and of the transducer's position independently from each other should be maximised.

Prior to using a hydrophone, we are trying a simpler system with a target. And a UVP (UB-Lab P) is managing the emission and reception by the transducer.

Moreover, a hydrophone presents a risk of degradation over time, as does the transducer, which will add a variability. A target will allow recording the distribution of the acoustic beam, which is the main information we need in the directivity study (direction and opening angle), not a quantitative amplitude.

The ideal target would be a sphere of millimeter or sub-millimeter range diameter, which could be moved around in three dimensions. An even simpler model to begin with is a 0.2mm nylon line weighted with a fishing sinker, attached to a carriage, moving in a 2D plane in front of the transducer.

5. Results

The accuracy of positioning was first assessed. The homing position of the carriage is very much repeatable with an uncertainty of 0.05mm. The relative positioning uncertainty is of less than 0.1 mm. These were determined following several campaigns of measurement and a total of about 30 target coordinate iterations and 10 measurement points per iteration, including assessment of repeatability, operator's error and measurement tool accuracy.

For the backscattered echo amplitude measurement, the peak of the target in the profile needs to be automatically detected and the gain needs to be automatically adapted to ensure the signal is not saturating. First results were obtained in Figure 6 for a grid of 9 coordinates, after the near field. Now the code needs to be further optimized to be as efficient and as fast as possible, to be able to characterise a series of transducers of different manufacturing, and later on different bistatic head geometries in reasonable durations.

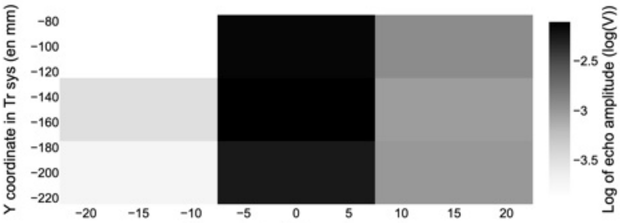

Figure 6: Backscattered echo amplitude at 9 points in front of a 1MHz, 20mm active diameter transducer

6. Summary

First measurements of the energy field to observe the actual distribution, including main direction and aperture angle, of any transducer with this new bench are promising. Higher resoluted maps should follow shortly.

The next step will be to acquire the maps of a series of transducers to check the statistics and spreading of the characteristics. We should then measure the spatial directivity patterns of a complete bistatic head and observe the influence of geometrical changes.

Numerical work will then also be developed further to improve the system's understanding, such as the impact of different sources of errors around the directivity: transducer manufacturing tolerance, piezoelectric element characteristics, the complete Rayleigh beam model, etc.

In the end, we would like to be able to characterise a bistatic transducer head's uncertainty due to the parallax bias. This can then be included knowingly when using the instrument in a hydraulic study case.

This study is part of a broader study on uncertainty sources in high-resolving Acoustic Doppler Velocimetry Profiling, including the hydraulic perturbation of the head which needs to be in contact with the medium.

We could also study the possibility of using various frequency transducers to expand the applicabilities: higher frequency for higher spatial resolution, or lower frequency for deeper exploration. These variations also impact the parallax bias.

References

[1] Hurther D, *et al.*: A multi-frequency Acoustic Concentration and Velocity Profiler for boundary layer measurements of fine-scale flow and sediment transport processes. Coastal Engineering, 58 (2011), 594–605 .

[2] Fromant G, *et al.*: An examination of point-particle Lagrangian simulations for assessing time-resolved hydroacoustic particle flux measurements in sediment-laden flows. J. Acoust. Soc. Am. 155 (4) (2024), 10.1121/10.0025766.

[3] Lemmin U & Rolland T: Acoustic velocity profiler for laboratory and field studies. Journal of Hydraulic Engineering (1997).

[4] Thorne P D & Hanes D M: A review of acoustic measurement of small-scale sediment processes. Continental shelf research (2002).

[5] Cabrera R & Lohrmann A: Small Scale Laboratory Flow Measurements with the ADV-1, Proceedings of OCEANS '93 (1993), DOI: 10.1109/OCEANS.1993.326129.

[6] Thomas R E, *et al.*: Bias in mean velocities and noise in variances and covariances measured using a multistatic acoustic profiler: the Nortek Vectrino Profiler. Measurement Science And Technology. 28(7) (2017).

[7] Rolland T & Lemmin U: A two-component acoustic velocity profiler for use in turbulent open-channel flow. Journal of Hydraulic Research, 35(4) (1997), 545–562.

[8] Fischer S, *et al.*: A new velocity estimation method using spectral identification of noise, Flow Measurement and Instrumentation 19(3) (2008), 197-203, DOI: 10.1016/j.flowmeasinst.2007.06.008.

[9] Moudjed B: Caractérisation expérimentale et théorique des écoulements entraînés par ultrasons. Perspectives d'utilisation dans les procédés de solidification du Silicium Photovoltaïque. Thèse de doctorat N° 2013ISAL0145, INSA de Lyon, Lyon (2013).

[10] Rolland T: Développement d'une instrumentation Doppler ultrasonore adaptée à l'étude hydraulique de la turbulence dans les canaux, Thèse de doctorat N° 1281, Ecole Polytechnique Fédérale, Lausanne (1994).

Can Ultrasonic Doppler methods unlock the dynamics of fluid mud in estuaries?

Sophie Defontaine[1,2]

[1] Cerema, RHITME Research Team, Margny Les Compiègne, France
[2] University Rouen Normandie, Université Caen Normandie, CNRS, Normandie University, M2C UMR 6143, Rouen, France

Hyper-turbid estuarine states, together with associated fluid mud, represent a critical management issue because of their pronounced impacts on water quality, estuarine ecosystem productivity, and navigational safety. Progress in our understanding of fluid mud dynamics has been hindered by the scarcity and limited resolution of in-situ data, mainly due to technical constraints in measuring fluid mud dynamics. In this study we propose to investigate the ability of the newly developed UBFlow3C Acoustic Doppler Velocity Profiler prototype for field deployment in quantifying turbulent velocities within fluid mud layers. An initial series of laboratory experiments was conducted using natural mud from the Loire Estuary. Fluid mud was introduced at the base of a cylindrical tank filled with tap water, generating a distinct two-layer flow characterized by a sharp luthocline and the presence of internal waves. Strong turbulence damping has been observed at the interface. Although preliminary, these first results are promising. This project is currently at a very early, exploratory stage. The work presented here is intended primarily to share initial observations and to solicit expert feedback and experience-based insights that will help guide future developments and experimental design.

Keywords: Fluid mud dynamics, Estuaries, Turbulence, laboratory experimentation

1. Introduction

Changing climate (sea level rise and prolonged drought) and increasing anthropogenic pressure (channel deepening) are likely to promote fine sediment accumulation, potentially driving estuaries toward hyper-turbid states [1, 2, 3]. In some estuaries, fluid mud layers extend over several tens of kilometers and can occupy as much as 40% of the water column. Past research has revealed that sediment-induced stratification may be responsible for shear reduction, suppression of bed-generated turbulence, thus reducing sediment flux and causing internal waves at the luthocline [4, 5]. Dyer and co-workers demonstrated the importance of internal waves which are likely to swamp any effects there may be of drag reduction [5]. The recent study of Becker and co-workers in the Ems Estuary reported that the stabilizing effect of sediment-induced stratification is notably more pronounced than generally considered [6]. They observed that vertical stratification is controlled by a balance between hindered settling and entrainment of fluid mud. However, the fundamental physical mechanisms at play in fluid mud dynamics are still poorly understood, representing a major gap in our understanding that urgently needs to be addressed.

In highly turbid environment, fine cohesive suspended sediment cause strong acoustic and optical attenuation, making conventional instruments unreliable. In addition, fluid mud composition (water, clay minerals, sand, silt, and organic matter) and its structure can vary significantly depending on location and depth. Then the following question arises: Can turbulent velocities reliably be quantified within fluid mud layers?

Various methods have been employed for measuring flow velocity in highly concentrated bed suspension layers, from epoxy-coated hot-film sensors and laser Doppler to electromagnetic current meters (ECM) [7, 8, 5], but each has major limitations. Measurements are generally restricted to one or two velocity components, at low frequency and at one or two depths. The need of better resolution data has been stressed on various studies [9, 10, 11, 6].

Ultrasonic Doppler methods have been used for oceanographic purposes to study mainly flows containing sandy sediments, and only few were devoted to cohesive sediments. Recently, laboratory experiments using ADV, LDV or UDVP have demonstrated the promising potential in measuring turbulence in fluid mud layers up to hundreds of grams per liter [12, 13, 14]. Although idealized laboratory experiments contribute significantly to our understanding, results from previous lab studies cannot be directly extrapolated to natural mud and estuarine hydrodynamic conditions. For example, under field conditions ADV has proved to be suitable for measuring turbulence velocities in mud mixtures with averaged concentration limited to 15 g/L [15].

In the present study, an innovative field velocity profiler based on ultrasonic Doppler acoustic method is proposed to uncover the physical processes at play in fluid mud dynamics in estuaries and the interactions between fluid mud layer and the overlying water body. The ability of the newly developed UBFlow3C (Ubertone) for field deployments to quantify turbulent properties has been tested under laboratory condition.

2. Material and Method

To assess the potential of the newly developed UBFlow3C (Ubertone) Acoustic Concentration and

Velocity Profiler prototype for field deployment in quantifying turbulent properties within fluid mud layers, an initial series of laboratory experiments was conducted using natural estuarine mud. Experiments were conducted in a cylindrical tank 40 cm in diameter and 50 cm high filled with tap water. The probe was plunged down-looking at the top of the tank with the emitting transducer located 35 cm above the bottom. An OBS5+ was placed in the tank to measure SSC (up to 50 g/L) 5 cm above the bottom.

The UBFlow3C instrument is based on the Acoustic Concentration and Velocity Profiler (ACVP) technology, already used in laboratory experiments [16, 17]. It has been turned into a field prototype for the project ANR WEST and has been successfully deployed on Porsmilin sandy beach [18]. This three-component ACVP is equipped with one central emitting transducer and four side receiving transducers (Fig. 1).

The first experiment was conducted to quantify turbulent properties within the fluid mud layer. A highly concentrated sediment suspension (over 140 g/L) was introduced in a tank filled with tap water 10 cm above the bottom. The velocity profile was measured continuously at 20 Hz from 15 cm away from the emitting transducer to the bottom of the tank, with cells of 5,24 mm. The suspended sediment concentration was measured continuously at 1Hz at 5 cm from the bottom of the tank.

Figure 1: On the left, the three-component ADVP (Acoustic Doppler velocity profiler) prototype named UB-lab 3C, equipped with 1 central emitting transducer and four side receiving transducers. On the right, the cylindrical tank filled with tap water and natural estuarine mud.

5. Results

When the fluid mud was injected into the tank, it produced a well-defined two-layer flow with a sharp luthocline (Fig. 2). The upper layer remained relatively calm, while strong turbulence developed in the lower layer (Fig. 3), accompanied by internal waves at the interface. As the experiment progressed, the sediment gradually settled to the bottom of the tank, increasing the sediment concentration up to 50 g/L.

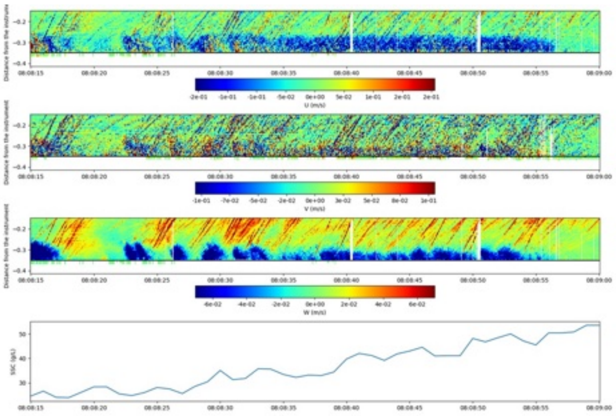

Figure 2: Timeseries of the three velocity components and suspended sediment concentration during the introduction of the sediment in the tank.

In order to estimate the measurement noise, we follow the method of Fugate & Chant (2005) [19], where it is defined as the difference between the total variance at zero lag and the covariance lagged one time step. The measurement noise was estimated around 6,3 x 10^{-4} m/s, i.e. several order of magnitude smaller than mean velocity.

The high-frequency sampling rate of the UBFlow3C allows direct measurements of Reynolds stress with a high degree of accuracy. Turbulent momentum fluxes were estimated as u'w' and v'w'. The turbulent kinetic energy production was estimated as the product of turbulent momentum flux and local shear: $P = -u'w'\frac{\partial u}{\partial z}$. The eddy viscosity was estimated as the ratio of turbulent momentum flux and local shear: $\nu_t = -u'w'\left(\frac{\partial u}{\partial z}\right)^{-1}$.

Profiles of turbulent momentum fluxes, TKE production, and eddy viscosity are shown in Figure 3. These profiles peaked in the last 5 cm above the bottom, with maximum values reaching 5×10^{-4} m^2/s^2, 9×10^{-4} m^2/s^2, 3×10^{-3} m^2/s^3 and 2×10^{-3} m^2/s, respectively; while these turbulent quantities were very low (close to zero) in the upper layer. This demonstrates the ability of density stratification to damp turbulence in a two-layer flow.

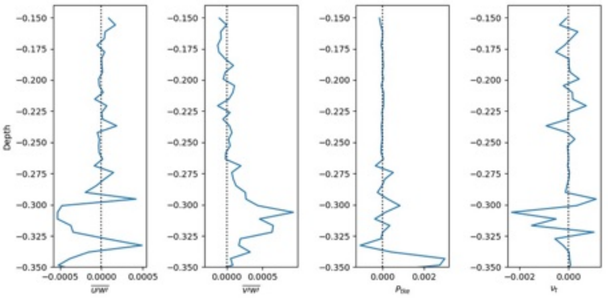

Figure 3: Turbulent momentum fluxes, TKE production, and eddy viscosity profiles.

6. Summary

This project is currently at a very early, exploratory stage. However, the UBFlow3C demonstrated its ability to measure velocity profiles at high-frequency sampling rate (20 Hz) along a vertical profile with a fine spatial resolution (5,24 mm cell size) in a highly concentrated suspension of cohesive sediments (about 50 g/L).

The high-frequency sampling rate allows us to estimate turbulent properties of the flow. A strong damping of the turbulence induced by density stratification has been observed at the luthocline.

Although preliminary, these first results are encouraging. Extensive experimental work is still required to assess the ability of the UBFlow3C to capture the dynamics of fluid mud in estuaries. The purpose of this work presented here is intended primarily to share initial observations and to invite expert feedback and experience-based insights that can guide future developments and experimental design.

References

[1] Takeda Y: Measurement of velocity profile of mercury flow by ultrasound Doppler shift method, Nucl. Technol. 79 (1987), 120-124.

[1] Al Mukaimi, M. E., Dellapenna, T. M. and Williams, J. R. : Enhanced land subsidence in galveston bay, texas: Interaction between sediment accumulation rates and relative sea level rise, Estuarine, Coastal and Shelf Science (2018), 207, 183–193

[2] Sherwood, C. R., Jay, D. A., Harvey, R. B., Hamilton, P. and Simenstad, C. A.: Historical changes in the columbia river estuary, Progress in Oceanography (1990), 25(1-4), 299–352

[3] Wolanski, E. and Chappell, J.: The response of tropical australian estuaries to a sea level rise, Journal of Marine Systems (1996), 7(2-4), 267–279

[4] Shiono, K. and West, J.: Turbulent perturbations of velocity in the conwy estuary, Estuarine, Coastal and Shelf Science (1987), 25(5), 533–553

[5] Dyer, K., Christie, M. and Manning, A.: The effects of suspended sediment on turbulence within an estuarine turbidity maximum, Estuarine, Coastal and Shelf Science (2004), 59(2), 237–248

[6] Becker, M., Maushake, C. and Winter, C.: Observations of mud-induced periodic stratification in a hyperturbid estuary, Geophysical Research Letters (2018), 45(11), 5461–5469

[7] Li, M. Z. and Gust: Boundary layer dynamics and drag reduction in flows of high cohesive sediment suspensions, Sedimentology (2000), 47(1), 71–86

[8] Thompson, C., Amos, C., Angelaki, M., Jones, T. and Binks, C.: An evaluation of bed shear stress under turbid flows, Journal of Geophysical Research: Oceans (2006), 111(C4)

[9] West, J., Oduyemi, K. and Shiono, K.: Some observations on the effect of vertical density gradients on estuarine turbulent transport processes, Estuarine, Coastal and Shelf Science (1991), 32(4), 365–383

[10] McAnally, W. H., Friedrichs, C., Hamilton, D., Hayter, E., Shrestha, P., Rodriguez, H., Sheremet, A., and Teeter, A.: Management of fluid mud in estuaries, bays, and lakes. i: Present state of understanding on character and behavior, Journal of Hydraulic Engineering (2007), 133(1), 9–22

[11] McAnally, W. H., Teeter, A., Schoellhamer, D., Friedrichs, C., Hamilton, D., Hayter, E., Shrestha, P. Rodriguez, H., Sheremet, A., Kirby, R. et al.: Management of fluid mud in estuaries, bays, and lakes. ii: Measurement, modeling, and management, Journal of Hydraulic Engineering (2007), 133(1), 23–38

[12] Baas, J. H., Best, J. L., Peakall, J. and Wang, M.: A phase diagram for turbulent, transitional, and laminar clay suspension flows, Journal of Sedimentary Research (2009), 79(4), 162–183

[13] Baas, J. H., Best, J. L. and Peakall, J.: Comparing the transitional behaviour of kaolinite and bentonite suspension flows, Earth surface processes and landforms (2016), 41(13), 1911–1921

[14] Thompson, C., Amos, C., Angelaki, M., Jones, T. and Binks, C.: An evaluation of bed shear stress under turbid flows, Journal of Geophysical Research: Oceans (2006), 111(C4)

[15] Sottolichio, A., Hurther, D., Gratiot, N. and Bretel, P.: Acoustic turbulence measurements of near-bed suspended sediment dynamics in highly turbid waters of a macrotidal estuary, Continental Shelf Research (2011), 31(10), S36–S49

[16] Hurther, D.,Thorne, P. D., Bricault, M., Lemmin, U. and Barnoud, J. M.: A multi-frequency acoustic concentration and velocity profiler (acvp) for boundary layer measurements of fine-scale flow and sediment transport processes. Coastal Engineering (2011), 58:594–605, 7.

[17] Fromant, G. , Hurther, D. , van der Zanden, J. , van der A, D. A., Cáceres, I., O'Donoghue, T., and Ribberink. J. S.: Wave boundary layer hydrodynamics and sheet flow properties under large-scale plunging-type breaking waves. Journal of Geophysical Research: Oceans (2019), 124:75–98, 1 2019. ISSN 21699291. doi: 10.1029/2018JC014406.

[18] Fritsch, N., Fromant, G., FLOC'H, F., Fischer, S., Cobac, Y., Poitou, C., Prunier, C., Bertin, S., Augereau, E., Jaud, M. et al.: Sediment dynamics under real waves, In Coastal Sediments 2023: The Proceedings of the Coastal Sediments 2023. World Scientific, 1940–1951

[19] Fugate, D. C., and Chant, R. J.: Near-bottom shear stresses in a small, highly stratified estuary, Journal of Geophysical Research: Oceans (2005), 110(C3).

Multi-Frequency Techniques in Nearshore Sediment Transport Acoustics

Gregory Wilson[1], Eli Faigle[1] & Alex Hay[2]

[1] Oregon State University, College of Earth Ocean & Atmospheric Sciences, Corvallis OR, USA.
[2] Dalhousie University, Department of Oceanography, Halifax NS, Canada.

Pulse-coherent MHz-frequency sonar has proven useful for investigating a variety of processes in nearshore wave dominated flows and associated sediment transport processes. The technique can achieve high resolution (e.g., turbulence resolving) velocity measurements in the water column and throughout the wave bottom boundary layer, while backscatter intensity can be used to infer sediment concentrations for calculating sediment transport rate. Additionally, the frequency dependence of scattering can be exploited to obtain more information on the scatterer types, for example sediment grain size can be inferred acoustically if it is not known a-priori. Here we present results using these techniques for measurements under energetic breaking waves over mobile sand beds, in the field and laboratory. Data are shown using a multi-frequency coherent Doppler system, MFDop, and a commercial Aquatec Aquascat 1000 multi-frequency backscatter profiler. We discuss processing techniques using the multi-frequency data to improve measurement quality, specifically mitigating the confounding effects of bubbles and high flow/turbulence which can often limit the reliability of acoustic remote sensing in the nearshore.

Keywords: Flow field measurement, Multifrequency acoustics, Inverse methods

1. Introduction

In the nearshore ocean, sediment transport is often surface gravity wave-dominated: A significant part of the net transport derives from small differences between the seaward and shoreward stroke of each wave, within a cm's thick region next to the mobile seabed. MHz-frequency pulse-coherent acoustic sonar is ideally suited to research in this area, since it can measure sediment concentration and velocity at spatial and temporal resolution sufficient to resolve the relevant wave processes, and remotely so as to not cause flow or bed disturbance. Multiple acoustic frequencies can also be used to add useful information for data inversion and interpretation. This was part of the motivation for developing the MFDop multi-frequency coherent Doppler profiler [1], a rugged field deployable 5-beam system capable of acquiring data at up to four discrete frequencies in the low MHz range.

The MFDop is intended for field research in the nearshore and surfzone, which can often be a challenging environment for pulse-coherent processing, due to the potential for strong turbulent flows and a complicated scattering environment. This has led us to investigate practical limitations, and ways to mitigate them. Here we show recent results using multi-frequency processing algorithms for nearshore wave and sediment transport research, with examples from MFDop and from an Aquatec Aquascat 1000R multi-frequency backscatter profiler. Two applications are considered. In the first application, the Aquascat was deployed in the surfzone of a high energy beach, Duck NC, using a large amphibious vehicle. Data were collected throughout the nearshore zone, including in regions where the water column contains a mixture of suspended sediment and breaking-produced bubbles. An extension to standard acoustic backscatter inversion algorithms was developed to account for the combined multi-frequency scattering from the bubble and sediment phases, and thereby remove bubble "contamination" effects from the inversion for sediment concentration. In the second application, the MFDop was used to measure near-surface flow under near-breaking waves generated in a laboratory wave flume. The high flow speeds present within the wave crest produced a strong "wrapping" effect in phase, as is typical for pulse-coherent Doppler profiler data in high velocity flow. Multi-frequency phase unwrapping [2] was found to be effective for removing the phase ambiguity and recovering a realistic velocity field.

2. Background

2.1 MFDop System Description

The Multi-Frequency coherent Doppler profiler, or MFDop [1], is a 5-beam acoustic profiler, with one active central beam and four outboard receivers in a symmetric bistatic isosceles geometry. The MFDop uses a broadband tone-sequence to transmit up to four concurrent frequencies for each ping, in a frequency range of 1.4 to 2.1 MHz. The multi-frequency data are independently demodulated to record multi-frequency phase and intensity at each range bin. Typical MFDop collections (as in the present work) use a per-frequency pulse length of 5 μs (for 3.75 mm range bin spacing), and ping intervals of order 1-2 ms. The field version of the instrument has a geometry such that a beam overlap region occurs within 0.8 +/- 0.2 m range, while a lab version uses a 0.4 +/- 0.1 m range interval. Measurements of 3-component velocity can be made within the beam overlap region, which is intended to overlap with the bottom boundary layer in our applications; backscatter intensity and along-beam velocity can be measured over a wider range using the center-beam only.

The MFDop's design prioritizes field deployment in breaking waves, with rugged pressure-rated enclosures and transducers. The latest generation of the MFDop, developed during the work presented here, incorporated more-compact and lower-power electronics that reduced the size of the main data acquisition case and further simplified the deployment logistics.

2.2 Experiments

Results will be shown from two experiments. The first experiment, named Blasstex (Boundary Layer Acoustics Suspended Sediment Transport EXperiment), was conducted at the US Army Corps of Engineers Field Research Facility (FRF) in Duck, NC, USA. The FRF operates a large amphibious vehicle called the Coastal Amphibious Research Buggy (CRAB) [3], which was used as a deployment platform in the experiment (Figure 1). Although the MFDop was deployed as part of Blasstex, here we focus on data from a complimentary instrument, the Aquatec Aquascat 1000R, which collected multi-frequency backscatter profiles at 0.5,1.0, and 2.0 MHz alongside the MFDop sampling location. The larger frequency range of the Aquascat allowed us to focus on multi-frequency backscatter inversion algorithm development (focus of the present work), while the MFDop provided complimentary high-resolution velocity data.

Validation data for acoustic backscatter inversions were collected using a sediment suction sampler, which provided near-coincident measurements of the local sediment concentration. Suction samples of 30 seconds each were collected at a range of CRAB station positions, with a known location and time for comparison to the acoustic data. More information on the Blasstex experiment can be found in [6].

Figure 1: Blasstex surfzone field experiment. The instrument frame is shown in the upper panel, which included an Aquascat 1000R (second from right) and sediment pump sampler (third from right, at midpoint of frame). The frame was attached to the FRF CRAB (lower panels), for making surfzone multi-frequency backscatter measurements at Duck NC.

A second experiment, named STONE (Sediment Transport Over Nearshore Environments), was conducted at the US Army Corps of Engineers Coastal Hydraulics Laboratory (ERDC CHL), Vicksburg MS USA. This experiment included measurements using the MFDop to probe the near-surface flow under waves near the onset of wave breaking. To prevent flow disturbance, the MFDop was mounted below a false floor of 3 mm thickness PVC (Figure 2). Preliminary bench-scale tests showed the PVC had approximately 60% transmittance at MFDop frequencies, and the transmitted energy was found to be sufficient for extracting pulse-to-pulse phases.

Research is ongoing to analyze the STONE results scientifically; for the purposes of the present work, the experimental setup provides a useful test dataset involving measurements at high flow speed at ~0.5 meters range, for evaluating a multi-frequency algorithm for Doppler phase unwrapping.

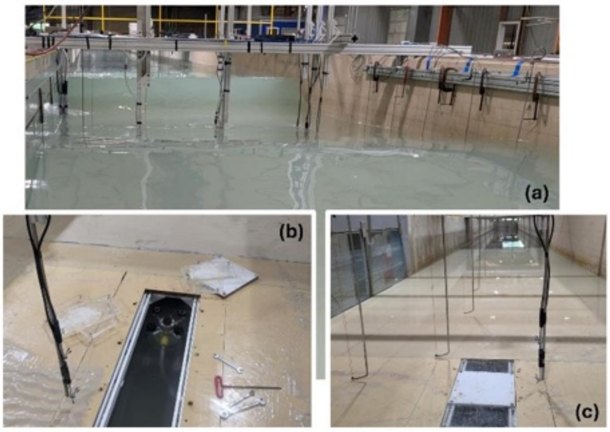

Figure 2: STONE wave lab experiment. Instruments including the MFDop were mounted in the Coastal Hydraulics Lab (ERDC CHL) 3-m wide wave flume, for measurements in breaking and near-breaking waves; photo (a) shows an example of a typical wave condition. The MFDop 5-beam system was mounted below the tank floor as shown in (b), and was covered by a panel of 3 mm thick PVC (white plate seen in photo (c)). The MFDop beams transmitted through the panel for obtaining upward-looking velocity profile data in the water column.

3. Results

3.1 Multi-Frequency Bubble Removal

One type of multi-frequency processing used in nearshore research is for interpreting backscatter amplitude. For example, if the backscatter is from sediment of an unknown size, then multi-frequency data can be used to infer the sediment size and concentration simultaneously [4]. Building on these previous methods, we have considered cases where the sediment is mixed with non-sediment scatterers, such as plastic flow-tracer particles [5] or bubbles [6]. Contamination by bubbles is a critical factor preventing reliable acoustic remote sensing of sediment transport in the surfzone, since wave breaking often produces high concentrations of microbubbles that persist throughout the water column and have similar size and acoustic scattering strength as sediment particles.

Figure 3 shows an example of Aquascat multifrequency backscatter in a mixed bubble-sediment water column under breaking waves. The lowest frequency measurements, 0.5 MHz, are dominated by backscatter in the uppermost portion of the profile, corresponding to bubble plumes generated by active wave breaking above the instrument. At higher acoustic frequencies, the backscatter becomes less sensitive to bubbles, while the scattering signal associated with near-bed sediments becomes more apparent. In this data, plumes of sediment are periodically ejected from the bed into the water column, a process usually associated with sand ripples.

Although the frequencies used here are much higher than the bubble acoustic resonance peak, a strong frequency contrast is seen in Figure 3 between sand and bubbles owing to (i) the very broad width of the bubble resonance peak, and (ii) the relatively weak scattering by the 0.18 mm diameter sediment at 0.5 MHz. An acoustic inversion model that approximates the sand and bubble acoustic cross-sections was used [6] to produce a combined inversion that separates bubble and sediment scattering. Comparisons to suction sampler validation data (not shown) showed an agreement of approximately 25% (includes possible experimental uncertainty of the suction sampler), whereas if no attempt was made to account for bubble contamination the errors were much larger, 300%.

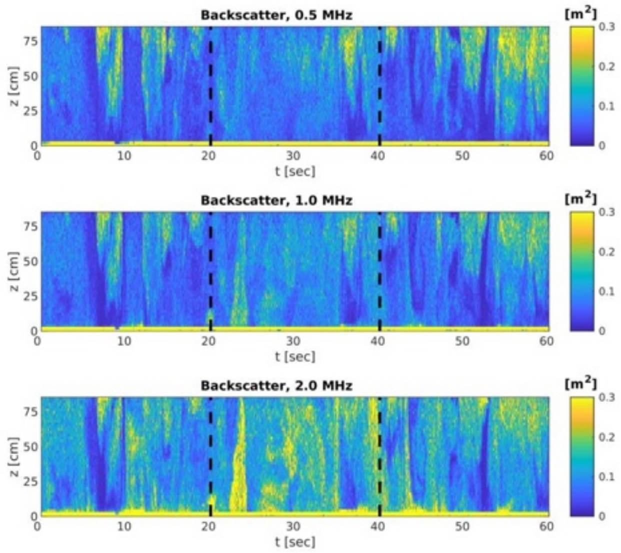

Figure 3 Blasstex measurements, from surfzone in Duck NC. (a) Backscatter profile data under breaking waves at Duck, NC ($z = 0$ is seabed). Data were sampled at 0.5 - 2.0 MHz, which highlights bubble backscatter at lower frequencies and mixed sand-bubble backscatter at higher frequencies. The frequency contrast was used by Wilson et al. (2024) to separate bubble and sand contributions in an acoustic inverse model.

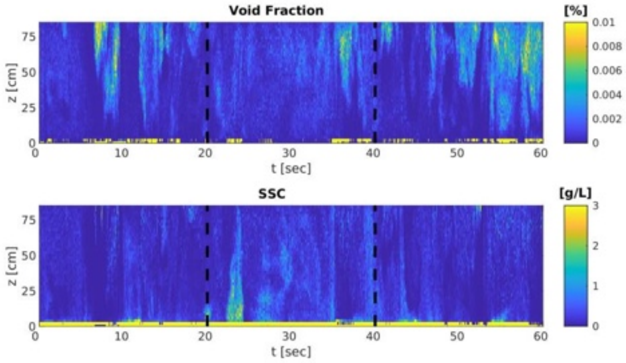

Figure 4 Blasstex results. An acoustic scattering model consisting of a canonical surfzone bubble size distribution and a measured sediment size distribution is used to invert multi-frequency backscatter intensity (Figure 3) for bubble void fraction and sediment concentration (SSC). The results, which were verified by independent measurements of SSC, shows frequency contrast between the two scatterer types (bubbles and sand) that allows them to be separated in the inversion.

4.2 Multi-Frequency Phase Unwrapping

Another use of multi-frequency information is to extend the velocity range of pulse-coherent processing and prevent “velocity wraps” [2]. In the nearshore zone, flow speeds routinely exceed 1-2 m/s, and wrapping is common for single-frequency processing. In our experience with MFDop data, this technique can work well provided there is a sufficiently high signal to noise ratio with which to infer the linear ramp of phase vs. frequency.

Figure 4 shows an example from the STONE experiment in the ERDC CHL wave flume (cf. Figure 2), measuring high flow speeds as a near-breaking wave passed over the upward looking MFDop, with flow speeds of 2-3 m/s. The raw phase data (not shown) contained up to +/- 3 wraps, owing to the relatively large flow speeds and ~0.5 meter profiling range. However multi-frequency unwrapping was effective in this case, resulting in a smooth and realistic velocity field.

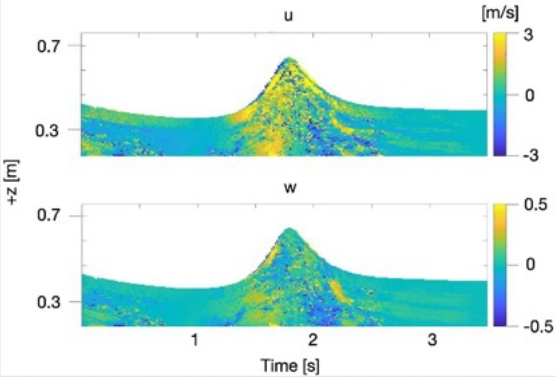

Figure 5: STONE results, from ERDC CHL wave flume. Horizontal (u) and vertical (w) velocities are shown from an up-looking MFDop profile, as a near-breaking wave passes over the instrument (data beyond the free surface was removed based on approximate surface-echo detection).

In this example case, the instrument sampled at $f = 1.4$, 1.9 and 2.1 MHz, with ping interval 1.45 ms and 5.25 μs pulse length. To obtain a best-fitting unwrapped velocity value from the multi-frequency data, an iterative robust least squares approach was used: Specifically, a velocity was determined that would produce a best-fit to the three measured phases (including wraps) in a least-squares sense. A Huber-type robust weighting was included in the fit based on an estimated phase noise variance of $\sigma_{\phi}^{2} = -2\log C$, where C is the correlation; residuals that exceeded $1.345\sigma_{\phi}$ were downweighted by a factor σ_{ϕ}^{-2}, to reduce the effect of outliers on the fit. Iterative least-squares was used due to the nonlinear inter-dependence between velocity, wrap value, and the Huber weights.

6. Summary

As more sophisticated acoustic systems are developed for sediment transport, multi-frequency techniques are one way to improve the fidelity and robustness of the measurements. We have found these techniques to be particularly useful in nearshore field research, where flow speeds and scattering conditions are often sub-optimal for pulse-coherent measurements. Multi-frequency backscatter inversion can help by removing the contaminating effects of bubbles when applying standard (single-scattering) inversion algorithms for sediment concentration. Multi-frequency phase information is one way to mitigate the phase wrapping that occurs in high flow speeds. Here we have shown two examples of these techniques being used in the context of surfzone sediment transport research.

References

[1] Hay, A. E., *et al.*. (2012). Observations of the vertical structure of turbulent oscillatory boundary layers above fixed roughness beds using a prototype wideband coherent Doppler profiler: 1. The oscillatory component of the flow. Journal of Geophysical Research: Oceans, 117(C3).

[2] Zedel, L., & Hay, A. E. (2010). Resolving velocity ambiguity in multifrequency, pulse-to-pulse coherent Doppler sonar. IEEE Journal of Oceanic Engineering, 35(4), 847-851.

[3] Birkemeier, W. A., & Mason, C. (1984). The CRAB: A unique nearshore surveying vehicle. Journal of Surveying Engineering, 110(1), 1-7.

[4] Hay, A. E., & Sheng, J. (1992). Vertical profiles of suspended sand concentration and size from multifrequency acoustic backscatter. Journal of Geophysical Research: Oceans, 97(C10), 15661-15677.

[5] Wilson, G. W., & Hay, A. E. (2015). Measuring two-phase particle flux with a multi-frequency acoustic Doppler profiler. The Journal of the Acoustical Society of America, 138(6), 3811-3819.

[6] Wilson, G. W., *et al.* (2024). Sediment Dynamics in the Energetic Nearshore Zone: Acoustic Remote Sensing and Model Validation. Journal of Geophysical Research: Oceans, 129(10), e2024JC021563

In-situ calibration of Acoustic Backscatter Systems for measuring suspended sand concentrations in rivers

Bjarne Vincent[1], Céline Berni[1], Guillaume Dramais[1], Jérôme Le Coz[1],
Benoît Camenen[1]

[1] INRAE, UR RiverLy, River Hydraulics, 5 Rue de la Doua 69100 Villeurbanne, France

Calibrating an Acoustic Backscatter System (ABS) for measuring suspended sediment concentrations usually requires a dedicated experiment in a well controlled environment that may not be easily available. In this article, we report a method for calibrating in-situ a down-looking ABS with a focus on river applications. Our approach combines water samples with the acoustic signals recorded over a vertical by two transducers to evaluate the attenuation and backscattering properties of the suspended sediments, as well as to evaluate the calibration constant k_t of each transducer. When applied to field measurements, our method captures both the shape and order of magnitude of the vertical suspended sand concentration profile. In addition, we assess the sensitivity of our method to the sample locations in the water column. We thus identify the critical parameters that may cause our method to break down, providing useful information regarding the use of uncalibrated ABS during field measurement campaigns.

Keywords: Acoustic Backscatter System, Suspended Sediment Concentration, Rivers

1. Introduction

In rivers, monitoring the suspended-sand concentrations (SSC) and fluxes is key to ensure a proper river management. During the last decades, hydroacoustic methods have aroused considerable interest because of their weakly-intrusive ability to measure suspended-sediment (sand and fine particles) concentrations at high spatial and temporal resolutions. The idea follows that of an active sonar: Acoustic Backscatter Systems (ABS) are placed below the water free surface, pointing towards the river bed. The ABS are then used to insonify the water column and to record the acoustic signals backscattered by the suspended sediments.

Retrieving the vertical profiles of suspended-sediment concentrations from acoustic signals requires inverting a nonlinear sonar equation relating the voltage from each transducer of the ABS to the properties of the sediments (concentration, particle size distribution (PSD) and density) [1]. Two difficulties arise: First, the unknowns outnumber the equations, meaning that the problem is ill-posed and requires additional information to be solved. Second, the sonar equation involves an instrument-specific calibration constant k_t that requires a tailored in-lab experiment to be determined [2]. In this paper, we provide a simple method for retrieving the SSC profiles by combining water samples and signals from uncalibrated ABS, i. e. systems for which k_t is unknown. Our method builds upon that of Vergne *et al.* [3] and combines samples with the signals recorded by two transducers operating at different frequencies. We stress that we do not aim to design a fully robust "k_t-free" method for measuring suspended-sediment concentrations, but rather to provide a simple method for calibrating an ABS in-situ to extract meaningful information until the instrument is better characterised.

The paper is organised as follows. The mathematical problem and its assumptions are outlined in section 2. Section 3 focuses on our in-situ calibration and acoustic inversion method for retrieving the vertical SSC profile; we then apply our method to field measurements in section 4. Concluding remarks are given in section 5.

2. Mathematical formulation of the problem

2.1 Assumptions

We shall assume that the sediments follow a bi-modal PSD, as it is often the case in rivers [4]. The fine mode is made of silt and clay particles, whereas the coarse mode corresponds to sand particles. For the commonly-used frequency range of the ABS (i. e. from 0.3 to 4.0 MHz), the sand particles are expected to be the main source of acoustic backscatter whilst the fine sediments essentially attenuate the sound waves [3,5]. Information regarding the sand fraction can thus be recovered by focusing on acoustic backscatter effects. As usually observed [3], we shall further assume that the PSDs of the fine and sand fractions remain constant in the insonified water column. We stress that the concentrations M_s and M_f of the suspended sand and fine fractions, respectively, vary spatially, and M_s is the main unknown to be determined.

2.2 Sonar equation relating the ABS voltage to the properties of the suspension

Under the assumptions given in section 2.1, the voltage V_i of the i-th transducer of the ABS is related to M_s and M_f through the sonar equation:

$$\overline{V_i(r)^2} = \frac{k_{t,i}^2 k_{s,i}^2}{r^2} M_s(r)\, e^{-4[\alpha_{w,i}+\alpha_{f,i}(r)]r}\,, \qquad (1)$$

where $\overline{\cdot}$ refers to an ensemble average over a large number of pings, r is the distance to the transducer, $\alpha_{w,i}$ is the sound attenuation coefficient due to water estimated using the model of François & Garrison [6], and $k_{s,i}$ is the sediment backscatter constant defined as:

$$k_{s,i} = \left[\frac{\int_0^\infty a^2 f_{\infty,i}(a)^2 n(a) \mathrm{d}a}{\rho_s \int_0^\infty a^3 n(a) \mathrm{d}a} \right]^{1/2} , \tag{2}$$

with a the sand particle radius, $\rho_s = 2650\,\mathrm{kg/m^3}$ its density, $n(a)$ the sand PSD (expressed as the fraction of the total number of particles per unit volume), and $f_{\infty,i}$ is the form factor estimated using the semi-empirical model of Moate & Thorne [7].

In Eq. (1), $\alpha_{f,i}$ is the sound attenuation coefficient due to the fine sediments and is related to M_f through:

$$\alpha_{f,i}(r) = \frac{1}{r} \int_0^r \zeta_i M_f(r') \mathrm{d}r' , \tag{3}$$

where ζ_i is the sediment attenuation constant characterising the sound attenuation properties of the fine sediments due to their PSD and the acoustic frequency. In river applications, the available models for ζ_i often perform poorly due to the irregular shapes of the fine particles [8]; we shall thus estimate ζ_i in-situ.

3. Calibration and acoustic inversion methods

3.1 Estimating the attenuation constants ζ_i and ζ_j

Let r_0 and r_1 be two distances on the acoustic path where M_f and M_s are known from samples. Let Q_i be the signal of the i-th transducer normalised by its magnitude at $r=r_0$. Then, from Eq. (1):

$$\begin{aligned} Q_i(r_1) =& \frac{\overline{V_i(r_1)^2}}{\overline{V_i(r_0)^2}} \\ =& \left(\frac{r_0}{r_1}\right)^2 \frac{M_s(r_1)}{M_s(r_0)} \\ & \times \exp\left[-4\alpha_{w,i}\left(r_1 - r_0\right) - 4\beta_{f,i}(r_1)\right] , \end{aligned} \tag{4}$$

where

$$\beta_{f,i}(r_1) = \int_{r_0}^{r_1} \zeta_i M_f(r') \mathrm{d}r' . \tag{5}$$

The normalisation procedure has three effects: (i) the integration path over M_f is changed, (ii) $k_{s,i}$ cancels out due to the constant sand PSD assumption, and (iii) $k_{t,i}$ is removed from the equations. This last point differs greatly from the single-sample method of Vergne *et al.* [3]: their inversion algorithm involves $k_{t,i}$ at each stage, so that uncertainties on that parameter are likely to propagate over the entire inversion process, including when estimating ζ_i.

As the fine PSD is assumed constant, ζ_i may be taken out of the integral in Eq. (5). Equation (4) can then be rewritten as:

$$\begin{aligned} \zeta_i =& \frac{1}{4\int_{r_0}^{r_1} M_f(r')\mathrm{d}r'} \Bigg(-4\alpha_{w,i}\left[r_1 - r_0\right] \\ & + \ln\left[\left(\frac{r_0}{r_1}\right)^2 \frac{M_s(r_1)}{M_s(r_0) Q_i(r_1)}\right] \Bigg) . \end{aligned} \tag{6}$$

Equation (6) can be directly applied to evaluate ζ_i, with M_s and M_f obtained from samples. One should ideally have several samples between r_1 and r_0 to approximate (e. g. through linear interpolation) and integrate the sampled M_f profile. The same process shall then be repeated for the j-th transducer operating at a different frequency to estimate ζ_j.

3.2 Estimating the vertical M_s profile with unknown ABS calibration constants $k_{t,i}$ and $k_{t,j}$

Knowing ζ_i, ζ_j and $M_s(r_0)$ from samples is actually sufficient to recover the vertical M_s profile. Indeed, computing $\zeta_j \ln[Q_i(r)]$ - $\zeta_i \ln[Q_j(r)]$ gives, using Eq. (4) :

$$\begin{aligned} M_s(r) =& M_s(r_0) \exp\Bigg[-2\ln\left(\frac{r_0}{r}\right) \\ & + \frac{\zeta_j \ln\left[Q_i(r)\right] - \zeta_i \ln\left[Q_j(r)\right]}{\zeta_j - \zeta_i} \\ & + \frac{4\left(r - r_0\right)\left(\zeta_j \alpha_{w,i} - \zeta_i \alpha_{w,j}\right)}{\zeta_j - \zeta_i} \Bigg] . \end{aligned} \tag{7}$$

We shall refer to Eq. (7) as the "k_t-free M_s estimate". Equation (7) shows that the whole M_s profile may be estimated by combining the acoustic signals at two different frequencies with at least two samples. Equation (7) is particularly well suited for a non-moving ABS operating during a sufficiently short time interval so that temporal variations of $M_s(r_0)$ can be neglected. However, Eq. (7) is inadequate for the case of a moving ABS, as samples over the horizontal $r=r_0$ line would be needed to recover the entire vertical M_s profile. In that case, the method of Vergne *et al.* [3] that requires knowing $k_s k_t$ for the two inverted signals is more appropriate.

3.3 Estimating $k_{s,i}k_{t,i}$ and $k_{s,j}k_{t,j}$ for applying the inversion method of Vergne et al. [3]

Using Eq. (3), the sonar equation (1) may be rewritten as:

$$\begin{aligned} k_{s,i}k_{t,i} =& r\sqrt{\frac{\overline{V_i(r)^2}}{M_s(r)}} \exp\Bigg[2\alpha_{w,i} r \\ & + 2\zeta_i \int_0^r M_f(r')\mathrm{d}r' \Bigg] . \end{aligned} \tag{8}$$

Measuring M_s and M_f from N samples, we can thus form N estimates of $k_{s,i}k_{t,i}$ and $k_{s,j}k_{t,j}$. Taking their average value over the vertical, one can finally obtain the M_s profile using [5]:

$$\begin{aligned} M_s(r) =& \exp\Bigg(\frac{\zeta_j}{\zeta_j - \zeta_i} \ln\left[\frac{r^2 \overline{V_i(r)^2}}{k_{s,i}^2 k_{t,i}^2}\right] \\ & - \frac{\zeta_i}{\zeta_j - \zeta_i} \ln\left[\frac{r^2 \overline{V_j(r)^2}}{k_{s,j}^2 k_{t_j}^2}\right] \\ & + \frac{4\left(\zeta_j \alpha_{w,i} - \zeta_i \alpha_{w,j}\right) r}{\zeta_j - \zeta_i} \Bigg) . \end{aligned} \tag{9}$$

In the following, we shall refer to Eq. (9) as the "k_t-

dependent M_s estimate".

Since $k_{t,i}$ is constant over the vertical, Eq. (8) may be used to evaluate the variations of $k_{s,i}$ with r, and thus to determine whether the assumption of constant sand PSD is satisfied. If the samples are also used to measure the sand PSD, then Eq. (8) can be combined with Eq. (2) to directly estimate $k_{t,i}$ and $k_{t,j}$, i. e. to calibrate the ABS in-situ.

4. Application to field measurements

4.1 Study site

We now apply our method to field measurements we made on the 22nd of May 2025, during a five-day field campaign on the Rhône River (France) that took place during a dam-flushing operation [9,10]. During our campaign, we probed the suspended sand under the Pyrimont Bridge, which is a two-pier bridge located 3.6 km downstream of Génissiat Dam. There, the river is approximately 100 m wide and 4 m deep.

4.2 Equipment and methods

The acoustic signals are emitted and recorded by an AQUAscat 1000R, which is a commercial multi-frequency ABS manufactured by Aquatec. The ABS is mounted on a floating board operated from the bridge and points downwards. We use the acoustic signals of two transducers operating one at a time and with a pulse (i. e. ping) repetition frequency of 10 Hz. The first transducer has an active diameter of 24 mm and radiates 0.5 MHz sound waves; the second transducer has an active diameter of 18 mm and emits 1 MHz waves.

We shall consider only the case of the ABS measuring vertical M_s profiles at a fixed position in the middle of the cross section, at approximately 50 m from the left bank. For each transducer, a single vertical profile of V is formed from an average over 2350 pings.

In addition to acoustic measurements, we also collect samples over the insonified column using an US-P6 pointwise sampler. The sampler is fitted with an hydrostatic pressure sensor to accurately measure the sampling depth. The sediments contained in the sampled water volume are then sieved at 63 µm to separate the sand and fine sediments, and determine their respective concentration.

4.3 Vertical profiles of M_s

The vertical profiles of the k_t-free and k_t-dependent M_s estimates are shown in Fig. 1 (a). Both methods capture the shape and order of magnitude of the sampled M_s, except at the point closest to the surface ($r \approx 0.5$ m) where both inversion results overestimate M_s. The k_t-dependent estimates differ by 18.4 % from the samples, whereas that discrepancy reaches 24.5 % for the k_t-free profile. This is caused by the fact that the k_t-free profile is forced to go through the sampled $M_s(r_0)$ (Eq. (7)). Therefore, any noise in the acoustic signals may shift artificially the whole profile and thus lead to either an underestimation or overestimation of the M_s profile.

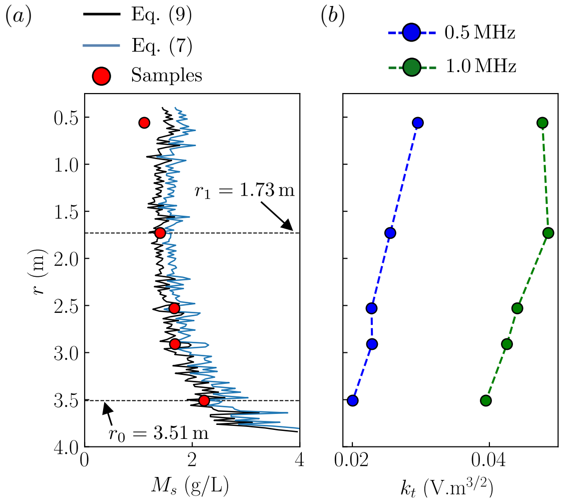

Figure 1: Results of the in-situ calibration and inversion procedure applied to measurements made in the Rhône River at Pyrimont Bridge (France) on the 22nd of May 2025, at approximately 50 m from the left bank. The signals are those of the transducers operating at 0.5 and 1.0 MHz. (a) Vertical profiles of the suspended sand concentration M_s obtained using the "k_t-free" approach (Eq. (7)) and using the $k_s k_t$ estimates (Eq. (9)). (b) Vertical profiles of the transducer calibration constant k_t estimated from the combination of Eq. (8) and Eq. (2).

By measuring the PSD of the sampled suspended sand sediments, we can also evaluate k_s and thus form vertical profiles of k_t for the two transducers (Fig. 1 (b)). The k_t profiles display variations about their mean values: the maximum difference is 22.3 % and 11.2 % for the 0.5 and 1.0 MHz transducers, respectively. Given that k_t is estimated from the pointwise combination of samples and signals, each subjected to their own uncertainties and measurement noise, these differences are rather small and give confidence on the ability of Eqs. (8) and (2) to provide the correct order of magnitude of k_t.

4.4 Sensitivity of the ζ_i and ζ_j estimates to the samples locations

The attenuation constants ζ_i and ζ_j are important parameters involved in all calibration and inversion steps of section 3 (including when estimating $k_{t,i}$ and $k_{t,j}$). The need for samples raises the question of how their locations affect the (ζ_a, ζ_b) estimates, where the subscripts a and b refer to the 0.5 and 1.0 MHz transducers, respectively.

Table 1 shows that the optimum ζ pair (i. e. the pair that minimises the difference between the sampled and the k_t-dependent M_s estimates) is found for (r_0, r_1) = (2.53, 1.73) m. Similar discrepancies between the sampled and k_t-dependent M_s profiles are observed for other (ζ_a, ζ_b), as long as the discrepancies on ζ_a, ζ_b and (ζ_b - ζ_a) remain within 30 %. This is typically the case for (r_0, r_1) = (2.91, 0.56) m for instance. In contrast, although choosing (r_0, r_1) = (1.73, 0.56) m yields only a 1.5 % variation on ζ_a compared with the optimum case, the 30.8 % variation on

ζ_b causes a 93.8 % gap on (ζ_b - ζ_a) and results in extremely poor M_s estimates. Therefore, the error on (ζ_b - ζ_a) is at least as critical as the error on ζ_a and ζ_b when applying our in-situ calibration and inversion procedure.

Finally, the best results are obtained when r_1 and r_0 are separated by at least 0.8 m (Table 1). Furthermore, uncertainties on the sampled concentrations may lead to unrealistic ζ estimates. This is for instance the case for (r_0, r_1) = (2.91, 2.53) m. There, the sampled M_s profile displays a surprising inflection point that is not observed in the raw signals. Such inconsistency can typically lead to unphysical negative ζ (Table 1).

Table 1: Sensitivity of the ζ estimates (m^2.kg^{-1}) to the choice of samples used for estimating M_s and M_f in Eq. (6). In each cell, the first and second lines correspond to the ζ estimates for 0.5 MHz and 1.0 MHz, respectively. The absolute relative difference (%) between the sand concentration profiles M_s obtained from Eq. (9) and samples is given in bold.

r_0 (m) r_1 (m)	0.56	1.73	2.53	2.91	3.51
0.56	-	0.0531 0.0548 **3.16×10^4**	0.0528 0.0647 **51.9**	0.0432 0.0627 **18.2**	0.0513 0.0778 **24.8**
1.73		-	0.0523 0.0792 **18.0**	0.0335 0.0705 **26.5**	0.0501 0.0778 **18.4**
2.53			-	-0.0046 0.0529 **39.9**	0.0482 0.0767 **18.9**
2.91				-	0.0857 0.0937 **292.3**
3.51					-

5. Conclusion

We propose a method for calibrating an ABS in-situ to measure vertical profiles of suspended sand concentration M_s. We show that concentration measurements are sufficient to evaluate the sediment attenuation constant ζ and $k_s k_t$ in-situ for each transducer, so that an existing acoustic inversion method of the literature can be applied to retrieve the vertical M_s profile. If the samples are used to measure the sand PSD, our method can also estimate the calibration constant k_t of each transducer.

We applied our methodology to the measurement of vertical M_s profiles in a 4-meter deep river. The results are promising, as the M_s profile obtained with our methodology typically differs by 18 % from the sampled profile. However, the choice and location of the samples used for calibrating the ABS may significantly alter the results: our best inversion results are obtained for samples separated by at least 0.8 m, and inconsistencies in the sampled concentration profiles (e. g. fictitious inflection points due to measurement errors) may cause our calibration and inversion method to break down. In particular, the estimation of ζ for each transducer and the difference between these two estimates are found to be critical for obtaining accurate M_s profiles.

We are currently planning a thorough calibration campaign to measure k_t for each transducer of our ABS in a controlled environment similar to that of Betteridge *et al.* [2]. It will be particularly interesting to see how the values of k_t estimated from our in-situ method compare to the results of these upcoming experiments, and to further quantify the strengths and weaknesses of our method.

References

[1] Thorne PD & Hurther D: An overview on the use of backscattered sound for measuring suspended particle size and concentration profiles in non-cohesive inorganic sediment transport studies, Cont. Shelf. Res., 73 (2014), 97-118.

[2] Betteridge KFE, *et al.*: Calibrating multi-frequency acoustic backscatter systems for studying near-bed suspended sediment transport processes, Cont. Shelf Res., 28 (2008), 227-235.

[3] Vergne A, *et al.*: Using a Down-Looking Multifrequency ABS for Measuring Suspended Sediments in Rivers, Water Resour. Res., 56 (2020), e2019WR024877.

[4] Agrawal YC & Hanes D M: The implications of laser-diffraction measurements of sediment size distributions in a river to the potential use of acoustic backscatter for sediment measurements, Water Resour. Res., 51 (2015), 8854-8867.

[5] Topping DJ *et al.*: High-resolution measurements of suspended-sediment concentration and grain size in the Colorado River in Grand Canyon using a multi-frequency acoustic system, Proceedings of the 10th International Symposium on River Sedimentation (2007), Moscow, Russia.

[6] François RE & Garrison GR: Sound absorption based on ocean measurements. Part I: Pure water and magnesium sulfate contributions, J. Acoust. Soc. Am., 75 (1982), 896-907.

[7] Moate BD & Thorne PD: Interpreting acoustic backscatter from suspended sediments of different and mixed mineralogical composition, Cont. Shelf Res., 46 (2012), 67-82.

[8] Vergne A, *et al.*: Acoustic Backscatter and Attenuation Due to River Fine Sediments: Experimental Evaluation of Models and Inversion Methods, Water Resourc. Res., 75 (2021), e2021WR029589.

[9] Dramais et al.: Combining sampling and acoustic backscatter profiling for estimating suspended sand concentrations during dam flushing, Proceedings of the 13th River Flow conference (2026), Thessaloniki, Greece.

[10] Pierrefeu et al.: Measurement of fine and sand suspended concentration throughout a river cross-section in the French Upper River Rhône: sampler, pump, acoustics, Proceedings of the 13th River Flow conference (2026), Thessaloniki, Greece.

Bedload & suspended sediment transport process analysis in highly turbulent open-channel flows using ACVP technology: performances & limitations for high inertia sediment flow case

Christophe Reymond[1,2], David Hurther[1], Giovanni De Cesare[2]

[1] Laboratory of Geophysical & Industrial Flows (LEGI), University Grenoble-Alpes, 1009 rue de la Piscine, 38041 Saint-Martin d'Hères, France.
[2] Plateform of Hydraulic Constructions. Ecole Polytechnique Fédérale de Lausanne (EPFL), Switzerland.

Sediment transport under energetic flow conditions remains difficult to quantify or model due to the strong coupling between turbulence and particle dynamics and the lack of high-resolution, co-located measurements of velocity and concentration. This study investigates bedload and suspended sediment transport processes in highly turbulent open-channel flows using the Acoustic Concentration and Velocity Profiler (ACVP). Controlled flume experiments were conducted with low-density, 5-millimeter particles under steady and fully turbulent flow conditions representative of bedload-dominated regimes. The ACVP provides time-resolved vertical profiles of velocity, sediment concentration, and sediment flux by combining Acoustic Doppler Velocity Profiling and Acoustic Backscatter techniques. The measurements highlight significant modifications of the mean flow and turbulence structure induced by the presence of sediments. Sediment flux profiles confirm that transport is primarily concentrated close to the bed, consistent with the high suspension number value. While the ACVP demonstrates strong capabilities for resolving benthic boundary layer sediment transport processes across both bedload and suspension layers, the results also highlight a key limitation of the current single-phase measurement approach for high inertia sediment transport case (*i.e.* when both particle Stokes and suspension numbers are much larger than unity). In this case, the ultrasound measured velocity corresponds to a mixture velocity between fluid and sediment Doppler signals. This limitation hinders explicit distinction between the fluid and the particle phases velocity fields which emphasize the need for two-phase flow acoustic measurement. This measurement ability will improve process-based understanding and modelling of sediment-laden flows. In particular, the ability of direct ultrasonic measurement of turbulent fluid-sediment interactions in the dilute suspension layer and particle-particle interactions within the dense bedload layer will offer new research perspectives.

Keywords: Sediment transport, fluid-particle interactions, Acoustic Concentration and Velocity Profiler, turbulent open-channel flow.

1. Introduction

Sediment transport is a fundamental process in fluvial and coastal systems, governing erosion, entrainment, and deposition, and thereby controlling channel morphology, bedform dynamics, and sediment budgets [1]. These processes are highly intermittent in time, as a large fraction of the annual sediment flux is conveyed during short-duration, high-energy events such as floods or storms, which drive the long-term morphodynamic evolution of natural systems. Accurate quantification of sediment transport under such energetic conditions is therefore essential for predicting morphological changes and managing impacts on hydraulic infrastructure and aquatic environments.

In open channel flows, sediment is transported through distinct modes depending on flow intensity and particle properties. Bedload corresponds to particles moving in contact with the bed under the action of shear stresses, whereas suspended load consists of finer sediments maintained within the flow by turbulent fluctuations [2], [3]. Increasing flow energy promotes a transition from bedload-dominated to suspension-dominated regimes, leading to complex mixed transport conditions. Under highly energetic flows, such as sheet-flow regimes (Shields number $\theta > 0.5$), sediment transport involves strong coupling between dense near-bed particle layers and dilute turbulent suspension, resulting in complex fluid–particle and particle–particle interactions. These conditions are particularly challenging to describe due to the coexistence of multiple transport mechanisms across a wide range of sediment concentrations and turbulent scales.

Despite significant advances in process-based modelling, current sediment transport formulations remain largely empirical and are often associated with large prediction uncertainties, especially under energetic flow conditions. Recent developments in two-phase flow modelling, particularly Eulerian–Eulerian Large Eddy Simulation approaches, have provided new insights into turbulence–particle interactions and sediment transport dynamics [4], [5]. However, their validation remains severely limited by the lack of high-resolution, turbulence-resolved experimental data capturing both fluid and particle phases simultaneously.

From an experimental perspective, the direct measurement of sediment transport fluxes remains a major challenge. Optical techniques are generally unsuitable for dense sediment-laden flows due to opacity, while conventional acoustic systems are limited in their ability to simultaneously resolve co-located velocity and concentration fields across the full range of transport regimes. In this context, the Acoustic Concentration and Velocity Profiler (ACVP) has enabled significant progress by providing turbulence-resolved sediment flux profiles spanning both suspension and bedload layers.

Current ACVP technology allows for detailed single-phase measurements of velocity and concentration profiles under a wide range of environmental conditions. Here, we present novel experimental data involving inertial particles, which further highlight the need for a new generation of ACVP systems capable of resolving the intrinsic two-phase nature of sediment-laden flows.

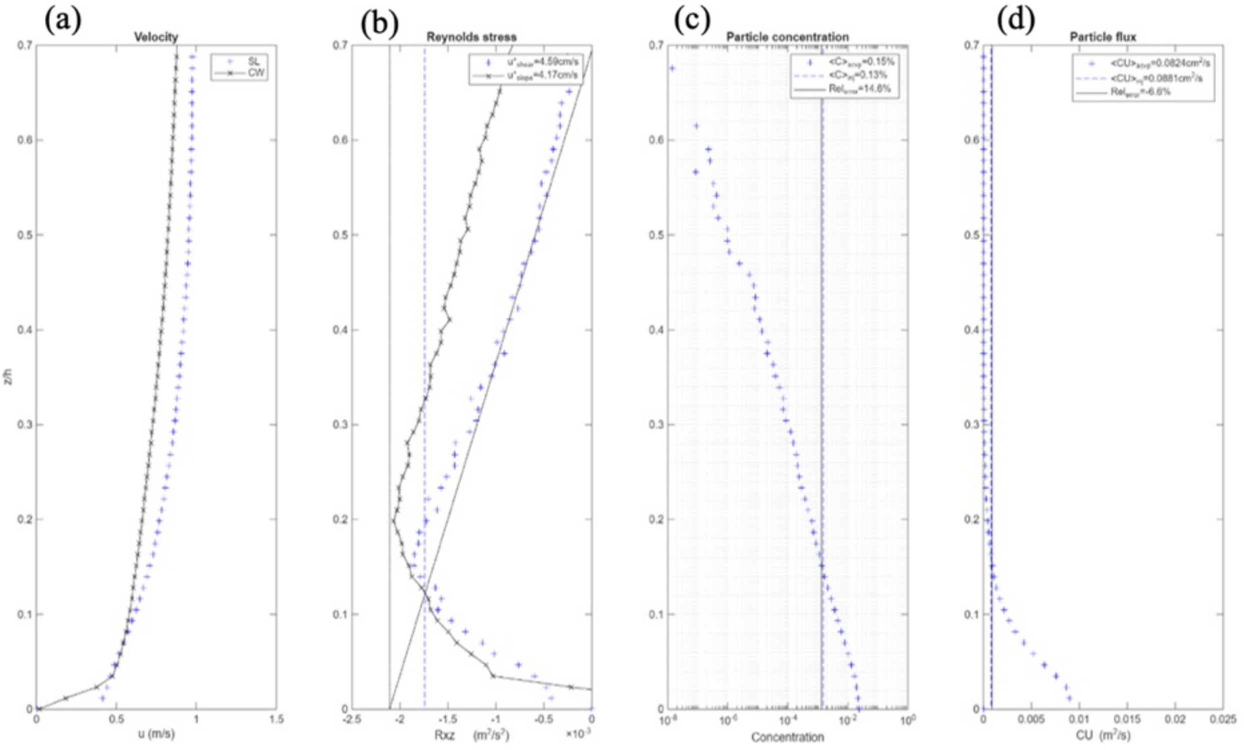

Figure 2: ACVP-measured profiles for the clear-water and sediment-laden flow conditions: (a) mean streamwise velocity, (b) Reynolds shear stress, (c) mean particle concentration, and (d) mean particle flux. Black lines and markers correspond to the clear-water experiment, while blue lines and markers represent the sediment-laden case.

The goal of this study is to investigate sediment transport processes in energetic open-channel flows using a novel experimental approach combining controlled sediment-laden flume experiments with advanced hydro-acoustic measurement techniques. In particular, the work aims to characterise the coupled dynamics of flow and inertial particles under well-defined hydraulic conditions, and to provide high-resolution observations of velocity and sediment transport quantities within both clear-water and sediment-laden open-channel flows under identical hydraulic conditions.

In the context of climate change, the projected increase in the frequency and intensity of extreme hydrological events further reinforces the urgency of advancing our understanding and modelling capabilities. Developing robust two-phase measurement techniques is therefore essential for improving predictive tools and supporting sustainable river and coastal management strategies.

Performances of process-based analysis of Boundary-Layer sediment transport will be addressed with a standard single-phase ACVP measurement approach. Direct measurement of momentum and Turbulent Kinetic Energy budgets will be reviewed for a new set of sediment-laden open-channel flow experiments using large (compared to Kolmogorov microscale), highly inertial PMMA particles as the sediment flow-phase. Current limitations due to standard ultrasonic single-phase measurements will be discussed.

2. ACVP technology

The Acoustic Concentration and Velocity Profiler (ACVP) is a multi-frequency ultrasonic measurement system designed to provide co-located, time-resolved profiles of particle velocity and sediment concentration in sediment-laden flows. It combines the principles of Acoustic Doppler Velocity Profiling (ADVP) and Acoustic Backscatter Systems (ABS) within a single instrument, enabling direct estimation of sediment fluxes over a large fraction of the flow depth.

The velocity measurement is based on the ADVP technique, which uses pulse-coherent Doppler processing of successive acoustic echoes to determine the velocity of insonified scatterers along the acoustic beam. This approach provides high temporal resolution (typically resolving turbulent time scales) and millimetric spatial resolution in the profiling direction. The measured velocity corresponds to the phase velocity of the dominant acoustic scatterers within the sampling volume, which may consist of fluid tracers when their inertial lag is negligible (i.e. for particle Stokes number well below unity), sediment particles, or a mixture of both when both sound scatteres are present in the insonified measurement sample volume.

Simultaneously, sediment concentration is derived from the ABS principle, which relates the amplitude of the incoherently scattered acoustic signal (in bistatic configuration [8], rather than for the standard monostatic mode of ABS, [6]) to the scattering properties and concentration of particles [6], [7], [8]. Multi-frequency (also called wideband, broadband) acoustic transmission can be used when both particle size and concentration profiles are to be estimated [6, 7] or for stabilizing concentration inversion when attenuation losses become non negligible and sediment size distribution is known [7, 9]. The inversion of acoustic intensity profiles relies on particle scattering models in the transition regime between purely Rayleigh and purely geometric scattering regimes but also for attenuation corrections to retrieve vertically resolved concentration profile across the dilute suspension and the dense bedload layers.

The integration of ADVP and ABS measurements within the same sampling volume allows for the direct computation of instantaneous sediment flux profiles as the product of local velocity and concentration. This co-located and simultaneous measurement becomes crucial for resolving turbulent sediment transport processes, as it ensures consistency between velocity and concentration measurements at the relevant spatio-temporal scales. The high-resolution profiling capability of the ACVP enables measurements across both dilute suspension layers and dense bedload regions, including the vicinity of the mobile bed interface. This advanced ultrasonic measurement capability has provided new insights in many river [10, 12, 14] and coastal sediment transport [11, 13] flow studies over the past 15 years.

3. Experimental setup & flow conditions

In this study, a new sediment-laden flow experiment was conducted using low-density PMMA particles (ρ_p = 1193 kg/m^3) with a median diameter of 5 mm. The experiments were performed in the tilting flume at LEGI, which is 10 m long, 0.36 m wide, and 0.5 m deep (Figure 1).

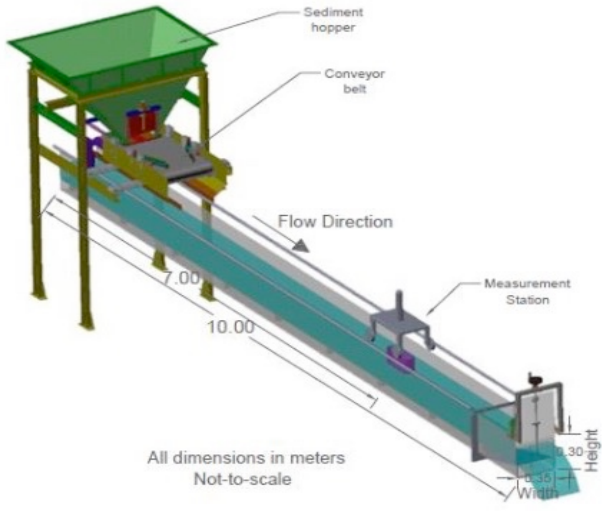

Figure 1: LEGI titling flume.

The applied experimental protocol consists of a sediment-laden run of several minutes, systematically preceded by a corresponding clear-water run. This ensures that the hydraulic conditions are strictly identical between the two configurations. As a result, any observed differences in the flow dynamics is assumed to be attributed to the presence of the sediment phase.

During the sediment-laden runs, PMMA particles are continuously supplied at the upstream end of the flume using a speed-controlled conveyor belt system, allowing precise control of the sediment feed rate and enabling experiments from clear-water (CW) to saturated full-capacity (sediment) transport conditions. Once the sediments enter the channel, they are transported over a fixed granular bed composed of glued particles of similar size (d_p = 5 mm). Both for clear water and sediment-laden runs, micro-bubbles are injected at the upstream end of the flume and are used as passive fluid tracers due to their particle Stokes number value being much lower than unity.

A sufficiently long development length is provided upstream of the measurement section, allowing the flow to reach fully developed turbulent flow and sediment transport conditions (local equilibrium between mean erosive turbulent flux and gravity-driven, mean particle settling flux. Measurements are performed under steady-state conditions, which were systematically verified in terms of both hydraulic and sediment transport conditions. The resulting flow is characterized by fully turbulent (Re > 100’000), fully hydraulically rough (roughness Reynolds number well above 70, not shown in Table 1) and subcritical (Fr < 1) flow conditions and well-established sediment transport state representative of energetic transport regimes (Table 1) with a Shield number value of 0.27. The duration of each run was set to 180 seconds in order to reach well-converged second and third order turbulence statistics (with a statistical bias error of less than 35% for all TKE budget terms).

Table 1: Experimental conditions.

d_p [mm]	w_s [cm/s]	Θ [-]	Q [l/s]	S [%]	U [m/s]	H [m]	q_s
5.0	7.4	0.27	32	0.23	0.28	0.135	$1.19*10^{-4}$

The hydraulic conditions were selected to be consistent with those reported by Guta et al. (2024) [10], in order to facilitate direct comparison between the two datasets and to identify differences induced by particle size and inertia. Indeed, the main difference lies in the PMMA sediment size and the larger sediment response time, with a median grain size of 5 mm instead of 3 mm in Guta et al.

The present particles exhibit higher inertia due to their larger size and higher settling velocity, resulting in a transport regime that is more strongly dominated by bedload dynamics. This is reflected in a lower suspension transport capacity compared to Guta et al., with a suspension number of approximately 1.8 in the present experiments compared to a value of 1.3 for Guta et al. [6], supporting a reduced contribution of suspended load relative to bedload transport.

4. Results and discussion

Figure 2 presents the ACVP-derived profiles for both clear-water and sediment-laden conditions, including velocity, Reynolds shear stresses, concentration, and sediment flux.

The presence of sediment significantly modifies the flow structure, as evidenced by the mean velocity and Reynolds stress profiles (Figures 2a-b). Compared to the clear-water case, the sediment-laden flow exhibits noticeable deviations, particularly in the near-bed region as well as higher up in the water column.

It should be emphasized that the measured velocity corresponds to a single-phase mixture velocity, resulting from the acoustic mixture velocity of both micro air bubble (fluid tracer) and solid particle (sediment phase) scatterers. The relative contribution of fluid tracers (micro-bubbles) and sediment particles velocities to this mixture velocity remains uncertain at present although it can be assumed that for this high suspension number value, the velocity in the dilute (particle) suspension layer can be attributed to the fluid phase. Indeed, it can be shown that the concentration of the micro- air bubbles remains fairly constant in both CW and SL (sediment-laden) conditions. However, this assumption becomes questionable for $z/h<0.2$. Therefore, this single-phase Doppler velocity measurement represents an important limitation of the current ACVP configuration. In the upper part of the flow, the acoustic signal is expected to be dominated by micro-bubbles, which behave as passive tracers and therefore provide a reliable estimate of the fluid velocity phase. In contrast, closer to the bed, the signal is increasingly influenced by sediment particles, especially under the present conditions where transport is predominantly bedload-driven. This transition likely explains the observed modification of the velocity profile in the near-bed region with the presence of a velocity inflexion point around $z/h=0.06$. While the clear-water profile follows the expected logarithmic distribution in the equilibrium region (0.05..0.25), the sediment-laden case shows a marked reduction of velocity near the bed, associated with the presence of moving particles and enhanced momentum exchange. The abrupt decrease of velocity at the bed level corresponds to the detection of the fixed granular bed at $z/h=0$. The absence of a high velocity gradient region for the mean (sediment) velocity over the region $z/h<0.05$ might also be due to the much larger sediment size compared to the micro air bubble size (50um) for the CW conditions. In other words, the sediment velocity results from a vertically integrated fluid velocity over a mean vertical domain of 5mm which corresponds to a relative integration domain $d/h=0.04$. This might explain the more abrupt velocity decrease for the SL flow conditions around $z/h=0$.

The Reynolds stress profiles further highlight the impact of sediment transport on turbulence structure. The presence of particles appears to alter turbulence production and redistribution mechanisms all along the water column. Figures 2c and 2d present the concentration and sediment flux profiles obtained from the acoustic intensity profile inversion of the ACVP. The inverted concentration profiles show good agreement with the injected sediment transport rates, indicating robust concentration and particle velocity estimates in the nearbed flow region. The vertical distribution of particle concentration expected trends, with high concentrations close to the bed and a rapid decay closer the free surface, reflecting the dominance of bedload transport in these experimental conditions [10].

The resulting sediment flux profiles reveal that transport is strongly concentrated in the near-bed region, with limited contribution from suspended load. This is in agreement with the very high suspension number ($S \sim 1.8$), which indicates that gravity driven particle settling dominates over turbulent erosion velocity. The measured flux structure therefore confirms that the present experiments correspond to a bedload-dominated transport regime, despite the highly turbulent flow conditions.

Overall, these results demonstrate the capability of the ACVP to capture key features of sediment transport processes across different flow regions. However, they also highlight an important limitation of the current single-phase velocity measurement approach: the inability to explicitly separate fluid and particle velocities. This limitation becomes particularly critical in energetic flows involving highly inertial particles (Stokes number $St_p>>1$), where strong lag velocity between the fluid and sediment phases occurs. These results therefore reinforce the need for the development of novel two-phase ACVP measurement methods of turbulence-resolved Doppler velocity fields for both fluid and sediment phases.

4. Conclusion

This study investigated sediment transport processes in highly turbulent open-channel flows using single-phase ACVP technology, with a particular focus on large partical Stokes number conditions corresponding to a highly inertial sediment-laden flow condition. The experimental protocol an methodology, combining flume experiments with high-resolution acoustic ACVP measurements, provide detailed insights into process-oriented sediment transport studies under well-controlled hydraulic conditions.

The results demonstrate that the presence of highly inertial sediments significantly alters momentum and TKE budgets. In particular, modifications of the mean velocity and Reynolds shear and normal stress profiles were observed across the whole water column. The concentration and sediment flux profiles confirm that transport is predominantly driven by bedload confirming the high suspension number value of the investigated sediment-laden flow.

The single-phase ACVP is shown to remain a powerful investigation tool for clear-water and sediment transport flows providing unique profile measurements of velocity, concentration, and sediment flux at high spatial and temporal resolutions. However, an important limitation of the current single-phase was put into quantitative evidence: the measured velocity corresponds to an acoustic mixture velocity of unknown weighting between fluid and particle phase velocities over the flow region 0.08<z/h<0.2. This single phase measurement limitation becomes critical in energetic sediment-laden flows when large high inertia sediments. Such complex sediment transport flow conditions imply complex two-way and four way turbulent flow fluid-particle interactions (Finn and Li 2016) for which two-phase turbulence resolved ultrasonic measurements become essential.

Such new measurement developments are aimed in the near future using wideband (multifrequency) ACVP technology currently under design. Validation of recent turbulence-resolved two-phase numerical models are aimed with the objective to improve quantitative predictions of sediment transport under climatic energetic flow conditions.

References

[1] M. Garcia, Éd., *Sedimentation Engineering: Processes, Measurements, Modeling, and Practice*. Reston, VA: American Society of Civil Engineers, 2008. doi: 10.1061/9780784408148.

[2] L. C. Van Rijn, « Sediment Transport, Part I: Bed Load Transport », *J. Hydraul. Eng.*, vol. 110, nº 10, p. 1431-1456, oct. 1984, doi: 10.1061/(ASCE)0733-9429(1984)110:10(1431).

[3] M. Cellino, « Experimental study of suspension flow in open channels », PhD Thesis, EPFL, 1998. Consulté le: 20 juin 2025. [En ligne]. Disponible sur: https://infoscience.epfl.ch/record/32301/files/EPFL_TH1824.pdf;experimental

[4] B. Vowinckel, V. Nikora, T. Kempe, et J. Fröhlich, « Momentum balance in flows over mobile granular beds: application of double-averaging methodology to DNS data », *J. Hydraul. Res.*, vol. 55, nº 2, p. 190-207, mars 2017, doi: 10.1080/00221686.2016.1260656.

[5] A. G. Kidanemariam et M. Uhlmann, « Interface-resolved direct numerical simulation of the erosion of a sediment bed sheared by laminar channel flow », *Int. J. Multiph. Flow*, vol. 67, p. 174-188, 2014.

[6] P. D. Thorne et D. M. Hanes, « A review of acoustic measurement of small-scale sediment processes », *Cont. Shelf Res.*, vol. 22, nº 4, p. 603-632, 2002.

[7] P. D. Thorne, D. Hurther, et B. D. Moate, « Acoustic inversions for measuring boundary layer suspended sediment processes », *J. Acoust. Soc. Am.*, vol. 130, nº 3, p. 1188-1200, 2011.

[8] S. A. Moore et A. E. Hay, « Angular scattering of sound from solid particles in turbulent suspension », *J. Acoust. Soc. Am.*, vol. 126, nº 3, p. 1046-1056, 2009.

[9] D. Hurther, P. D. Thorne, M. Bricault, U. Lemmin, et J.-M. Barnoud, « A multi-frequency Acoustic Concentration and Velocity Profiler (ACVP) for boundary layer measurements of fine-scale flow and sediment transport processes », *Coast. Eng.*, vol. 58, nº 7, p. 594-605, 2011.

[10] H. Guta, D. Hurther, et J. Chauchat, « Bedload and Concentration Effects on Turbulent Suspension Properties in Heavy Particle Sheet Flows », *J. Hydraul. Eng.*, vol. 148, nº 7, p. 04022012, juill. 2022, doi: 10.1061/(ASCE)HY.1943-7900.0001988.

[11] Grossmann, F., Hurther, D., van der Zanden, J., Sánchez-Arcilla, A., & Alsina, J. M. Near-bed sediment transport processes during onshore bar migration in large-scale experiments: Comparison with offshore bar migration, 2023, *Journal of Geophysical Research: Oceans*, 128, e2022JC018998.

[12] Naqshband S, Ribberink, J. S, Hurther D., Barraud, P.A., and Hulscher, S.J.M.H. Experimental evidence for turbulent sediment flux constituting a large portion of total sediment flux along migrating sand dunes, 2014, *Geophysical Research Letters*. doi: 10.1002/2014GL062322.

[13] Fromant, G., Hurther, D., Van Der Zanden, J., Van Der A, D. A., Caceres, I., O'Donoghue, T., et al., Wave Boundary Layer Hydrodynamics and Sheet Flow Properties under Large-Scale Plunging-Type Breaking Waves, 2019, *Journal of Geophysical Research: Oceans*, 124(1),75-98.

[14] Revil-Baudard, T., Chauchat, J., Hurther, D. and Eiff, O. Turbulence modifications induced by the bed mobility in intense sediment laden flows, 2016, *Journal of Fluid Mechanics*. 808, 469-484.

Wave Boundary Layer Dynamics around Onshore-Migrating Bars

Florian Grossmann[1,3], David Hurther[2], Rafael Almar[1], and Jose Alsina[3]

[1]Laboratory of Space Geophysical and Oceanographic Studies (LEGOS), Midi-Pyrénées Observatory, Toulouse, France; [2]Laboratory of Geophysical and Industrial Flows (LEGI), Université Grenoble Alpes, Grenoble, France; [3]UPC BarcelonaTech, Barcelona, Spain

An Acoustic Concentration and Velocity Profiler (ACVP) measured near-bed velocity fields over onshore migrating sandbars in near prototype-scale wave flume experiments (Grossmann et al. 2023, 10.1029/2022JC019299). The low energy waves (H_s<0.25m) propagated over the bars without breaking. Offshore, on top of and onshore of bars the ACVP measured wave boundary layer (WBL) dynamics and near-bed velocity attenuation $K_b(z)$. Idealized attenuation as a function of a WBL width (δ_{WBL})-normalized vertical coordinate (Dunbar et al. 2023, 10.1016/j.coastaleng.2022.104242), represented most measurement locations well (Figure 1). However, bar geometry influenced δ_{WBL} and attenuation. Considering cross-shore dependent, geometry-related WBL effects on sediment transport may improve morphological models (Grossmann et al. 2026, 10.1029/2025GL119305).

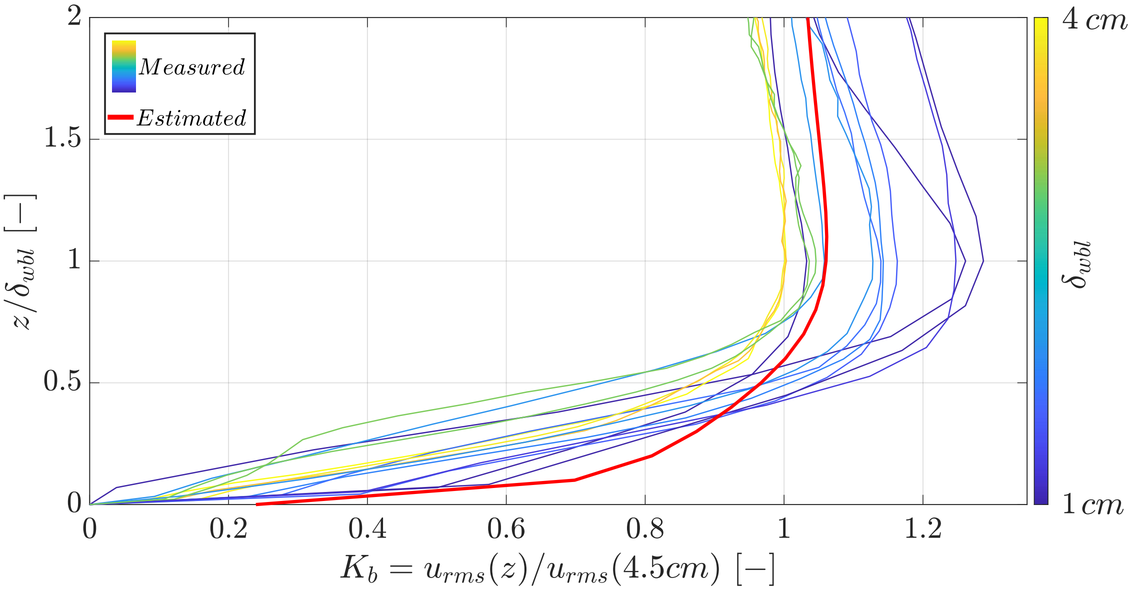

Figure 1 Wave flume measurements of attenuation $K_b(z)$ (root-mean-squared velocity inside the boundary layer normalized by free-stream root-mean squared velocity) as a function of distance from the seabed normalized by wave boundary layer width. Curves in blue to yellow (color representing measured boundary layer width, color bar on the right) are from different cross-shore positions around onshore migrating bars under low energy wave conditions. The thick red curve is the idealized model of Dunbar et al. 2023.

ADV measurements in an aerated Denil fish pass

J. Schneider, A. Hussin, S. Haun

November 28, 2025

Institute of Hydraulic Engineering and Water Resources Management,
Graz University of Technology, Stremayrgasse 10, A–8010 Graz

Email: schneider@tugraz.at

Abstract: This study aimed to investigate the hydraulic behaviour of the standard Denil fish pass, with a focus on the impact of aeration and flow dynamics. The tests were conducted in the hydraulic laboratory at Graz University of Technology as part of a master's thesis (Hussin, 2024). The tests were conducted at a scale of 1:1; the flume was 4.75 metres long and had a longitudinal slope of 20%. To control the aeration as precisely as possible, the fish pass was adapted to be fully covered. This prevented any air from entering through the water's surface. ADV measurements were performed using Nortek Vectrino sensors, with air added in a controlled manner via an SMC flow controller at a rate of about 10 l/min. Two measurement planes were defined approximately in the middle of the flume: one directly in the baffle plane (12 x 6–9 measurement points) and another between two baffles (15 × 12 measurement points). Additionally, the results were compared with numerical calculations of the Denil Pass (Oguah, 2022), for which the fish pass was not covered.

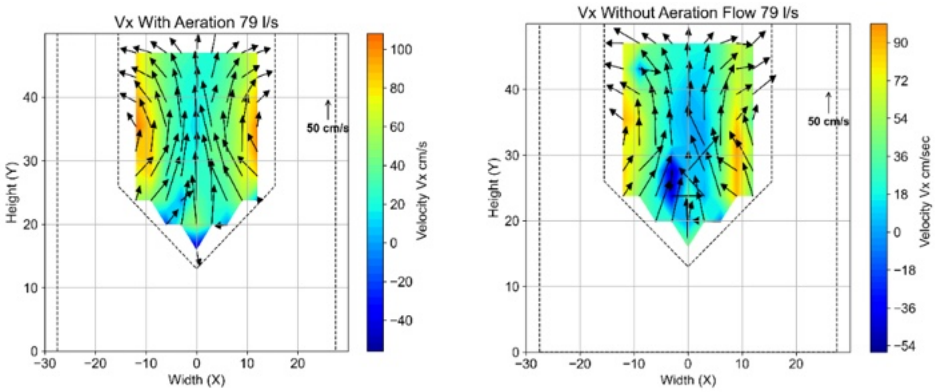

Figure 1: Velocity V_x, with and without aeration (Hussin, 2024)

In the study, the prevention of aeration resulted in a notable reduction in velocity, ranging from 20 to 30%, particularly observed at the middle and edges of the fish pass. Conversely, the introduction of aeration contributed to the enhancement of flow dynamics. Controlled aeration introduced into the model significantly influenced flow dynamics, resulting in altered velocity distributions and turbulence patterns. Aeration increased mean velocities and TKE, with notable variations observed across different sections of the fish pass.

Keywords: ADV, vectrino, Denil fish pass, aerated flow

Effect of Submerged Vane Field on Flow Characteristics in a Mobile-bed Channel with 30° Water Diversion

Zehra Büyüker[1], Gökçen Bombar[2]
[1,2] Civil Engineering Department, İzmir Kâtip Çelebi University, Türkiye.

Diversion channels often exhibit a disproportionate sediment-to-water diversion ratio, with sediment being diverted more efficiently than flow. This imbalance creates serious engineering challenges. Submerged vane fields in bifurcation zones offer a potential mitigation strategy; however, the hydro-morpho-dynamic behavior of vane-controlled mobile-bed diversions is still not well understood. To investigate the effect of submerged vane field on the flow characteristics and morpho-dynamics, two experiments (uncontrolled and controlled with a submerged vane-field) were conducted in a rectangular channel system composes of a rectangular main channel and a smaller diversion until bed equilibrium was reached. The diversion channel is connected to the main channel through the diversion angle of θ = 30°, skew angle of the vanes, equal to 10°. For the equilibrium deformed bed, 3D velocity measurements were made using an Acoustic Doppler Velocimeter (ADV). According to results, no distinct scour holes formed without vanes, whereas the vane-field induced a continuous scour trench along the vanes. The vane-field generated a continuous vortex system that diverted bed particles away from the diversion entrance by forming a scour trench (both upstream and downstream of diversion) along the inner wall. In the uncontrolled case, a vortex formed in the diversion channel originating from the main channel, whereas the vane-field effectively suppressed its formation.

Keywords: Diversion, Submerged vane field, Three-dimensional flow

1. Introduction

Diversions in natural and man-made movable bed channels affect and characterize the division of water and sediment in channel bifurcations. In nature, bifurcations frequently occur in braided rivers and deltas. Man-made lateral diversions include the entrance to a secondary channel, used as a by-pass for flood alleviation, integrated into a navigation or irrigation project, or connected to a settling basin designed to reduce the sediment load passing to a water system. In such natural and man-made diversion channels, an imbalance exists between the amounts of diverted sediment and water, the sediment diversion being disproportionately higher than the water diversion. This imbalance can lead to significant engineering challenges that must be addressed.

Flow at a diversion juncture is complex and has been the subject of extensive studies [1,2]. Asymmetrical bifurcations, defined by a given diversion angle (downstream angle between the main axes of the diversion channel and the main channel), θ, induce specific three-dimensional flow structures. Some of these flow structures were first documented by Rao et al. (1968) for θ = 90° in a smooth, fixed-bed channel. Their findings showed that flow separation at the upstream corner of the diversion channel generates a recirculation zone extending over approximately half of the upstream width of the lateral diversion (Figure 1). The study conducted by [3] also identified the following flow regions: a potential secondary separation zone in the main channel on the opposite side of the juncture, and a contraction flow zone in the side channel.

Recent works by [4-6] further illustrated that lateral flow diversions induce some complex vortical systems. These vortices can be altered by a vane field, strongly impacting the performance of vanes as devices used to control sediment diversion [2,6].

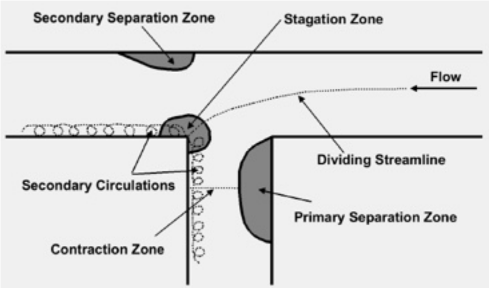

Figure 1: Flow structures at a flow juncture according to [1,4]

When examining the literature, although studies exist on the effects of vane field in movable-bed diversions under live-bed conditions, knowledge of the hydro-morpho-dynamics of vane-controlled movable-bed diversions remains limited.

The purposes of the present work were (i) to research the flow field described in the literature in the diversion zone in the absence of vanes, and (ii) most importantly, to identify the changes in the flow field induced by the vanes and relate them to possible alterations in bed morphology. In both cases, the velocity field was measured at the equilibrium stage, enabling the bed morphology at equilibrium to be characterized.

2. Experimental Set-up and Procedure

Two laboratory experiments were performed: one refers to a diversion with no vanes (hereafter, named NV) and the other one to a diversion with a vane-field in front of the entrance (named VF). Both experiments were conducted in a rectangular channel system composes of a rectangular main channel and a smaller diversion at the Hydraulics

Laboratory of Instituto Superior Técnico (Figure 2). The diversion channel is connected to the main channel through the diversion angle of θ = 30°, with no bed discordance.

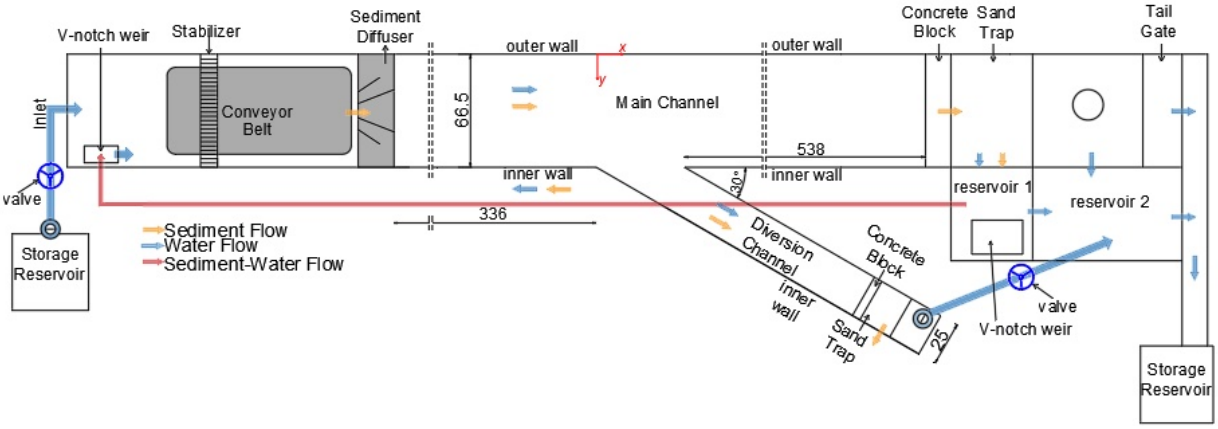

Figure 2: Schematic plane view of experimental set-up

The vane-field comprised two parallel rows of seven vane-arrays. The vanes, made of PVC, were 0.10 m long and 0.01 m thick, protruded vertically h = 0.03 m into the flow column above the initial sand bed and exhibited a 10° skew angle (Figure 3).

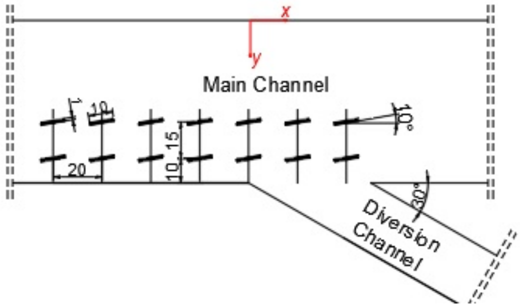

Figure 3: Detail of vane-field

Water is pumped from the laboratory storage reservoir through a pressure pipe into the upstream flume chamber. Sand was added to the main channel through a constant-speed (12 kg/h) conveyor belt which was operated upstream of the main channel. The flow depth, along the main channel was controlled by a tailgate.

During each experiment, the bed topography and the water level were frequently surveyed, in both channels, with mini-echo-sounder and ultrasonic sensor, respectively.

Each experiment was run until the equilibrium bed was reached. For the equilibrium deformed bed, 3D velocity measurements were made using an Acoustic Doppler Velocimeter (ADV) attached to the robotic arm (Figure 4). Since velocities were measured at each point for 180 s with a sampling frequency of 100 Hz, every record included 18,000 values per point of each velocity component. Taking the average of these values, the time average velocities in the x, y, and z directions, respectively, u, v, and w, were obtained.

Figure 4: Acoustic Doppler Velocimeter (ADV)

3. Results and Discussion

Figure 5 shows the velocity $u (\mathrm{m\,s^{-1}})$ as a color scale and the direction and magnitude of the velocity components (v, w) $(\mathrm{m\,s^{-1}})$ as vector arrows for both the NV and VF cases.

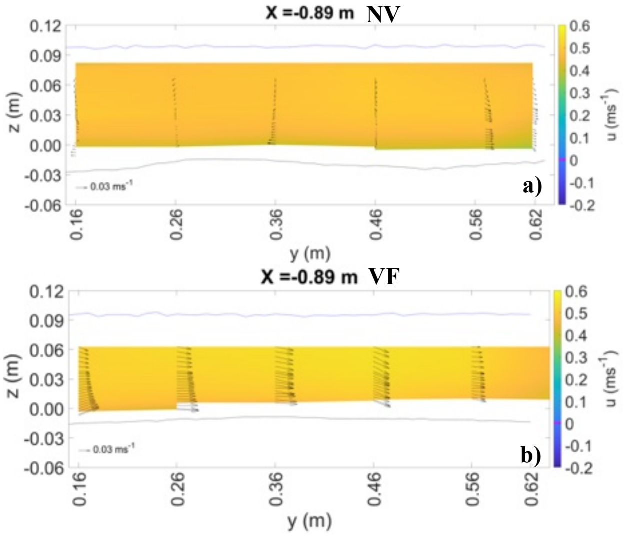

Figure 5: Velocity field at x=-0.89 m: a) NV experiment b) VF experiment

In NV, the flow velocity was predominantly oriented downstream at 0.89 m upstream of the diversion (Figure 5a), displaying a comparatively small crosswise component. Since this section corresponds to the beginning of the vanes in the VF case, it is clearly observed that the v velocity component is higher here compared to the NV case (Figure 5.b).

Reaching the vane-field, at x = -0.24 m (Figure 6), the flow was altered when compared with the flow in the most upstream cross-sections of the VF case, with a circulation created around the vanes (red arrow around the vanes). The streamwise velocity, u, also decreased significantly close and slightly below to their tips.

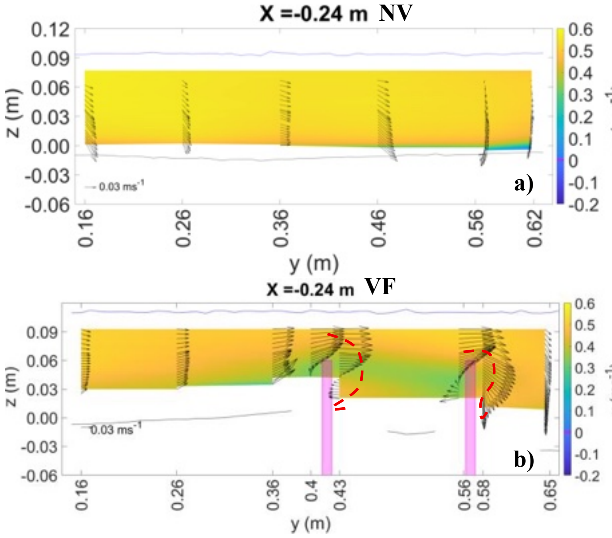

Figure 6: Velocity field at x=-0.24 m: a) NV experiment b) VF experiment

The downward flow generated near the vanes for $z < 0.03$ m likely contributed to the local scour observed around them. According to results, no distinct scour holes formed without vanes, whereas the vane-field induced a continuous scour trench along the vanes consistent with the findings of [7] (Figure 6).

Figure 7 shows the velocity field cross sections at x=0.04 m, x=0.18 m, x=0.31 m and x=0.40 m for the NV case. Diversion entrance is indicated with black dashed line at y=0.65 m.

In the NV experiment, the increase in the v component near the bed at the diversion entrance promotes the formation of a vortex within the diversion channel, originating from the main channel. This vortex is highlighted with a red dashed line at x=0.18 m and x=0.31 m.

The flow structure can drive a large amount of the main-channel bed load with the diverted water in NV case (Figure 7).

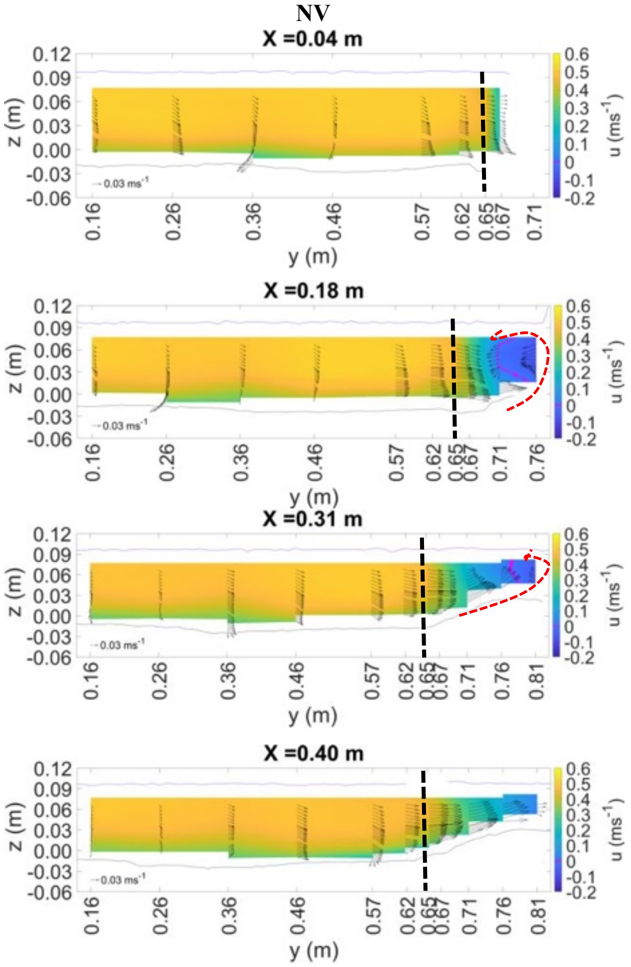

Figure 7: Velocity field of NV experiment between x=0.04 m and x=0.40 m

At x=0.10 m there is no vortex for y=0.65 m (mouth of the diversion), meaning that the vane-field inhibited its development, thus reducing the amount of sediment entering the diversion.

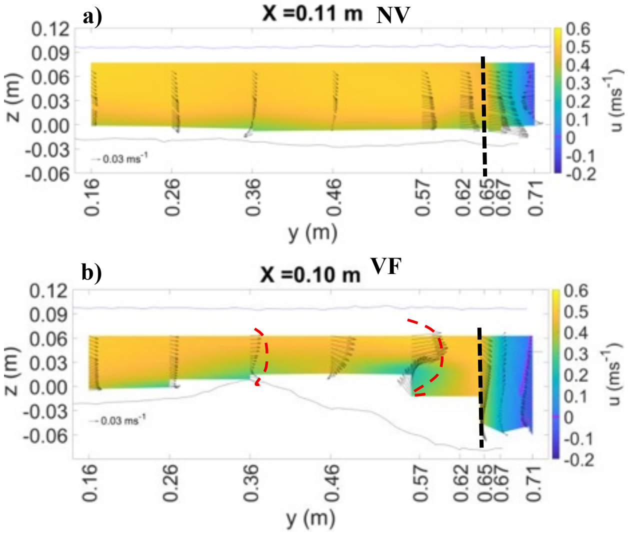

Figure 8: Velocity field at x=0.10 m: a) NV experiment b) VF experiment

The cross section at x=0.11 is located downstream of the vanes y=0.36 cm and y=0.57 cm, exhibits circulation generated around the vanes. Particularly noteworthy was the vane-field's ability to inhibit sediment transport into the diversion channel (Figure 8)

The near-bed *v* velocity component decreases progressively in the downstream of the diversion along inner wall of the mail channel for NV case (Figure 9).

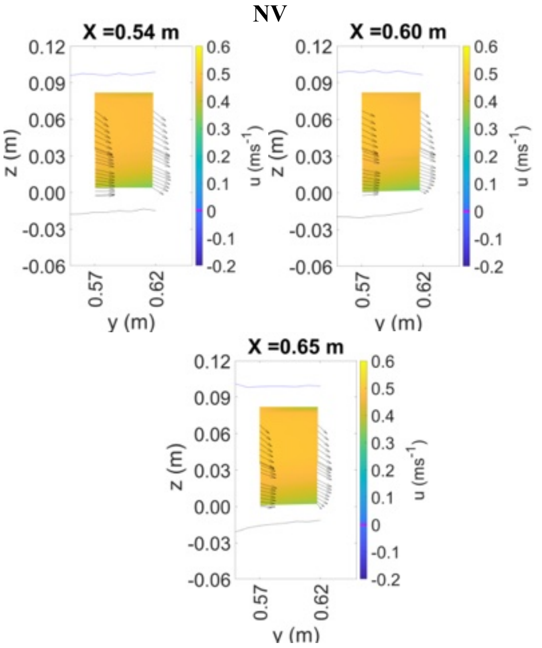

Figure 9: Velocity field downstream of diversion in NV case

The vane-field generated a continuous vortex system along its entire length, extending downstream, which effectively deviated a significant portion of the main channel bed particles from the diversion entrance (Figure 10). The formation of a scour trench along the main channel's inner wall, downstream of the diversion channel including its entrance, was clearly observed consistent with the findings of [6] (Figure 10).

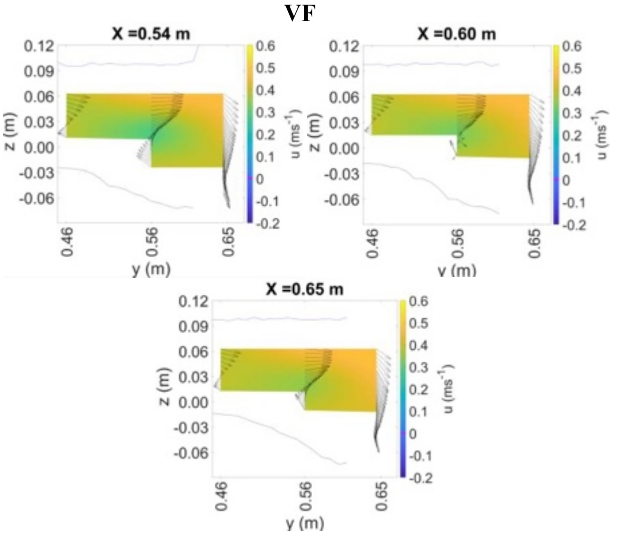

Figure 10: Velocity field downstream of diversion in VF case

4. Conclusions

The flow field and the bed morphology of an equilibrium 30° mobile-bed bifurcation with and without vane field are presented.

In the uncontrolled experiment, a vortex formed within the diversion channel originating from the main channel; notably, the vane field effectively prevented the formation of such a vortex. The vane-field generated a continuous vortex system along its entire length, extending downstream, which effectively deviated a significant portion of the main channel bed particles from the diversion entrance. This was achieved through the formation of a scour trench between the inner row of the vane-field and the main channel inner wall, both upstream and downstream of the diversion channel, including its entrance.

References

[1] Rao NL, et al: Experimental study of the division of flow in an open channel, In Proc. Conf. Hydraulic and Fluid Mechanics, Washington, DC (1968), 139–142.
[2] Barkdoll BD, et al: Sediment control at lateral diversions: Limits and enhancements to vane use, J. Hydraul. Eng., 125 (1999), 862–870.
[3] Neary VS & Odgaard AJ. Three-dimensional flow structure at open channel diversions, J. Hydraul. Eng., 119 (1993), 1223–1230.
[4] Hsu CC, et al: Subcritical 90° equal-width open-channel dividing flow, J. Hydraul. Eng, 128 (7) (2002), 716–720.
[5] Herrero A, Bateman A, Medina V: Water flow and sediment transport in a 90° channel diversion: An experimental study, J. Hydraul. Res., 53 (2015), 253–263.
[6] Baltazar JE, et al: Effect of a submerged vane field on the flow pattern of a movable bed channel with a 90° lateral diversion, Water, 13 (6) (2021), 828.
[7] Gumgum F &Cardoso AH: Effect of diversion angle and vanes' skew angle on the hydro-morpho-dynamics of mobile-bed open-channel bifurcations controlled by submerged vane-fields, Physics of Fluids, 36(7) (2024).

Spatial configurations of submerged roughness elements influence sediment erodibility similarly to their density: a case study of common cockles

Maxime Laukens[1], Christian Schwarz[1,2]

[1] Hydraulics and Geotechnics, Department of Civil Engineering, KU Leuven, Kasteelpark Arenberg 40 - box 2448, 3001 Leuven, Belgium.
[2] Geography and Tourism, Department of Earth and Environmental Sciences, KU Leuven, Celestijnenlaan 200e - box 2411, 3001 Leuven, Belgium.

Bed topography in natural sedimentary environments – including rivers, estuaries, floodplains, and tidal flats – varies across a wide range of spatial scales, from individual grains to larger bedforms such as ripples and dunes. The influence of these large-scale bedforms on flow dynamics and sediment transport has been extensively studied. In contrast, the hydrodynamic and transport effects of roughness generated by biological activity, commonly referred to as bioroughness, remain comparatively understudied despite being widespread in fluvial, estuarine, and coastal environments.

This study uses common cockles as a template biogenic roughness structure to investigate how spatial arrangement, combined with two distinct organism densities, affect sediment transport magnitude in controlled flume experiments. Measurements combine the UB-Lab 2C Acoustic Doppler Velocity Profiler (ADVP) (Ubertone) velocity profiling, with optical backscatter sensors, and structure-from-motion morphological surveys. Results indicate that roughness pattern configuration, specifically inter-cockle and inter-cluster spacing, produces substantial variability in sediment transport magnitude under increasing uniform flow conditions compared to organism density alone. ADVP measurements further reveal links between local (element-scale) and cluster-scale turbulence intensities and observed erosion patterns. This study represents a first step toward improving understanding of biologically mediated sediment transport processes in riverine and estuarine environments.

Keywords: Biogenic roughness, Sediment transport, Flow field monitoring, Spatial configuration

1. Introduction

Coastal and estuarine ecosystems rely on bio-stabilization, i.e. the process by which biological structures – such as bivalves, tube builders or vegetation patches – modify near-bed flow and thereby influence sediment stability. While the role of roughness-element density in altering near-bed hydrodynamics has been well-documented [1], the impact of spatial configuration, i.e. the clustering of these roughness elements, remains poorly understood, especially for fully submerged structures.

Previous studies have demonstrated that sediment erodibility depends on size and density [2], yet in natural landscapes, organisms exhibit complex, multi-scale clustering rather than uniform coverage [3]. This spatial heterogeneity determines whether flow is deflected at the crest level or penetrates the structure to mobilize sediment within clusters. High-density or tightly packed configurations can induce a skimming flow regime, where shear is concentrated above the canopy and turbulence is prevented from reaching the bed. In contrast, porous or fragmented configurations may sustain substantial vertical momentum exchange above the crest (z/h>1) [4], enhancing internal scour. A key challenge in understanding these mechanisms is the ability to resolve changes in turbulence intensity and near-bed velocity gradients, which requires high-resolution acoustic measurements.

In this study, we combine controlled flume erosion experiments with bistatic Acoustic Doppler Velocity Profiler (ADVP) measurements to quantify how both density and spatial configuration of submerged bivalve shells influence sediment erodibility. We introduce a new clustering index (ϕ_c) to quantify spatial relationships and show that ϕ_c provides a first-order predictor of configuration-specific erosion behavior, beyond what can be inferred from density alone. This extended abstract presents the clustering framework, outlines the methodological approach and experimental setup (Section 2), summarizes key relationships between clustering and erodibility (Section 3.1), and illustrates ADVP-derived velocity, Reynolds stress, and TKE profiles we relied on to interpret the erosion results (Section 3.2).

2. Methods

2.1 Clustering index

To characterize the spatial arrangement of roughness elements beyond density alone, we introduce a clustering index (ϕ_c), defined as the ratio of the first (d_w) and second (d_b) medians of the multi-modal distribution of all pairwise inter-element distances:

$$\phi_c = \frac{d_w}{d_b} \tag{1}$$

The first median, d_w, is dominated by shorter inter-element distances and thus is representative of the average within-cluster distance. The second median, d_b, is dominated by longer distances between clusters and therefore is representative of the average between-cluster distance.

A larger ϕ_c indicates larger and more closely spaced clusters, while a smaller ϕ_c represents smaller clusters separated by wider gaps. The proposed metric captures both cluster size (via d_w) and inter-cluster spacing (via d_b), providing proxy measures to link spatial organization to erosion response.

2.2 Erosion experiments

Erosion experiments were conducted in a 9-m rectangular flume containing a 0.4 m × 0.6 m muddy (~42% mud) sediment bed. Dead *Cerastoderma edule* shells were used as model roughness elements and inserted into the sediment surface. Two densities were tested:

- High density (H): 550 ind.m^{-2}
- Medium density (M): 140 ind.m^{-2}

For each density, shells were arranged into a series of controlled spatial configurations, ranging from fully dispersed (H0, M0) to a single aggregated cluster (H1$_c$, M1$_c$), including intermediate multi-cluster patterns (Fig.1a). Density was kept constant within each density class; thus roughness density (as reported by [1]) also remained constant, while cluster size and spacing, and therefore ϕ_c varied systematically.

Flow velocity was increased stepwise from 0.25 to 0.55 ± 0.015 m s^{-1}. Suspended sediment concentration (SSC) was measured continuously using an optical backscatter sensor (Campbell Scientific, ClariVue) to derive the critical velocity for erosion, following [5]. After the maximum velocity was reached, morphological change was quantified by reconstructing the eroded sediment volume using photogrammetric 3D models generated in Agisoft Metashape. Total eroded volumes were computed for the full test section and separated between inside and outside the cluster boundaries to separate within-cluster scour from edge/outer scour; these areas are delineated in Fig.1a.

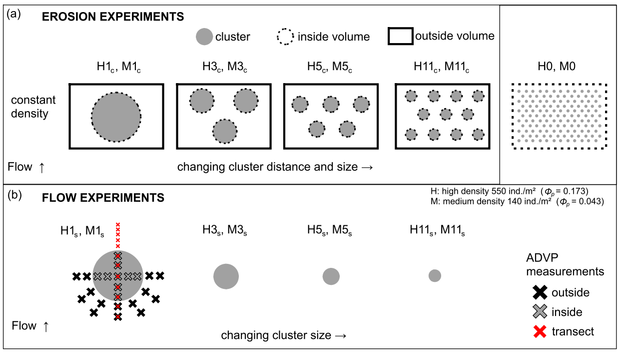

Figure 1: (a) Spatial configurations used in the erosion experiments. Density is constant within each configuration series (constant roughness density ϕ_p cf. [1]). Cluster size and inter-cluster spacing vary, which changes the clustering index ϕ_c. Solid and dashed masks delineate the zones used to separate eroded volume inside and outside cluster boundaries. (b) Setup for flow experiments with single clusters matching the diameters in (a). ADVP profile locations (upstream edge, inside, and transect) are illustrated for one example configuration; the same sampling scheme was applied to all cluster sizes.

2.3 Flow experiments

To isolate the hydrodynamic mechanisms underlying the observed erosion patterns, single-cluster flow experiments were conducted without sediment, using identical cluster sizes as in the erosion runs (Fig.1b). This design removes cluster-cluster wake interactions and provides insight into how individual clusters modify flow.

Flow fields were measured using the UB-Lab 2C ADVP (Ubertone) providing ~2 mm vertical resolution profiles of velocity, turbulent kinetic energy (TKE), and Reynolds shear stress, derived from the streamwise and vertical velocity components. Profiles were collected along concentric half-circles around the cluster (covering the upstream and laterally exposed edges) as well as at locations inside the cluster (Fig.1b). Additionally, we measured longitudinal centerline transects across single clusters, from upstream to downstream in the streamwise direction, allowing reconstruction of local flow attenuation, shear-layer development, and turbulence penetration within and around clusters.

3. Results

3.1 Erosion experiments

Results indicate that total eroded volume depended on both spatial configuration and roughness-element density (Fig.2). Spatial configuration exerted an effect on total eroded volume comparable in magnitude to density (Fig.2a). Increasing density from medium (M) to high (H) reduced eroded volumes by up to 6.3 times. Yet, at constant density, changing the spatial configuration alone altered erosion by up to 8.2 times, demonstrating that configuration can have a similar effect as density on sediment erodibility.

Separating volumes into inside vs. outside the cluster boundaries reveals distinct mechanisms. In high-density patterns, only ~2-6% of the total eroded volume occurred inside clusters, and scour concentrated outside the edges, which is consistent with skimming flow shielding. In medium-density patterns, ~12-45% of the total eroded volume occurred inside clusters, indicating deeper turbulence penetration and internal scour.

The fully dispersed configurations (M0, H0) behaved differently from the clustered patterns. H0 exhibited the highest total eroded volume of all high-density cases, despite showing lower local intensities than the intermediate clustered patterns (M3$_c$, H3$_c$) (not shown). Without aggregation, numerous isolated elements eliminate inter-cluster wake interference and instead produce more spatially uniform, yet less locally focused, erosion than in patterned configurations.

When plotted against clustering index ϕ_c, the total eroded volume increased approximately linearly for both densities (separate regressions), with peak erosion at the highest clustering index (ϕ_c ~ 0.35-0.40) (Fig.2b). At these intermediate configurations (M3$_c$, H3$_c$), eroded volumes were 2.7-8.2 times greater than in the single, highly aggregated configurations ($M1_c$, $H1_c$), reflecting the combined effect of clusters that are large enough to deflect flow while remaining close enough to enhance inter-cluster wake interference.

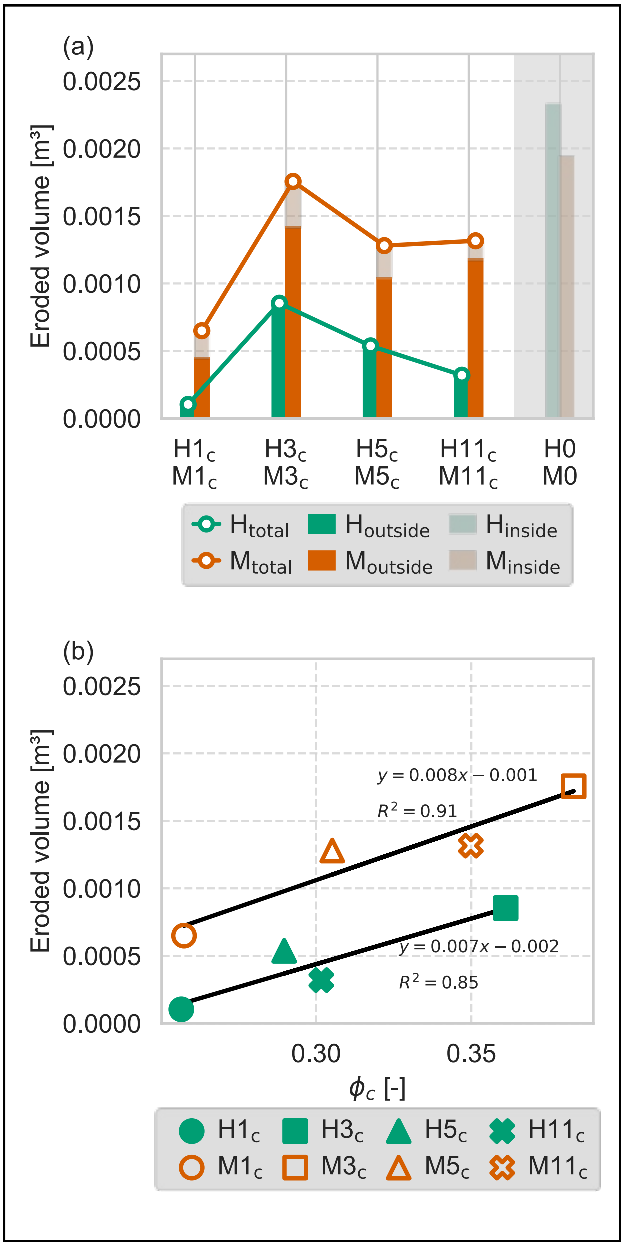

Figure 2: (a) Total eroded volumes (H_{total}, M_{total}), separated into inside (light bars) and outside (dark bars) regions relative to cluster boundaries, for medium- (orange) and high-density (green) configurations. (b) Linear regression of the total eroded volume vs. clustering index ϕ_c for medium- and high-density configurations.

3.2 Flow experiments

To understand the mechanisms driving the erosion patterns in Section 3.1, we analyzed spatially averaged ADVP profiles of velocity, TKE and Reynolds shear stress for all cluster sizes and both densities, normalized by the spatially averaged depth-averaged incoming flow velocity, $\langle U_0 \rangle$ (Fig.3). These profiles capture the inflection and turbulence maximum at the crest level (z/h=1), near-bed velocity attenuation inside clusters, and edge acceleration outside clusters.

Inside clusters, high-density cases exhibit near-zero velocities below the crest, and low near-bed TKE, confirming skimming flow shielding and explaining the minimal internal erosion in Section 3.1. In contrast, medium-density cases maintain higher near-bed TKE and Reynolds shear stress, consistent with deeper turbulence penetration, which may explain the observed internal scour. Outside clusters, both densities show edge acceleration, and below-crest-level turbulence maximum.

Profiles also reveal a configuration dependence: intermediate cluster sizes ($H3_s$, $M3_s$) generate the strongest crest-level turbulence and steepest velocity gradients, aligning with the peak erosion at intermediate clustering, reported in Section 3.1.

Summarizing message:

- High element density → skimming flow regime : crest shear layer isolates the bed; outside-cluster scour dominates.
- Medium element density → wake-interference regime : turbulence penetrates below the crest; internal and edge scour both contribute.

Results from single-cluster experiments suggest that at intermediate clustering, corresponding to the highest clustering index ϕ_c, clusters are large enough to deflect flow yet close enough to potentially enhance inter-cluster wake interaction, which may explain the maximum erosion observed at these ϕ_c levels.

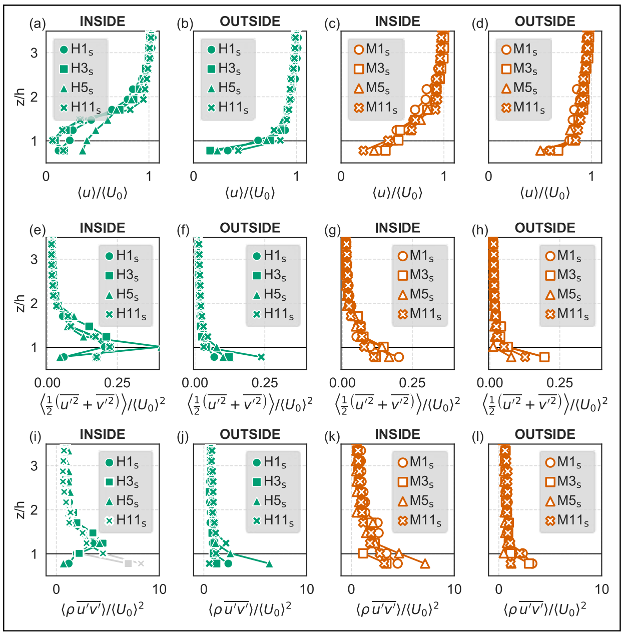

Figure 3: Spatially averaged, normalized profiles of (a-d) streamwise velocity $\langle u\rangle/\langle U_0\rangle$, (e-h) turbulent kinetic energy $\langle \frac{1}{2}(\overline{u'^2}+\overline{v'^2})\rangle/\langle U_0\rangle^2$, and (i-l) Reynolds shear stress $\langle \rho\overline{u'v'}\rangle/\langle U_0\rangle^2$, for all cluster sizes and both densities, separated into inside and outside profiles. The horizontal line at z/h=1 indicates the cluster crest height h. Grey markers denote data points where

ADVP signal quality was insufficient below z/h<1.

4. Summary

This study demonstrates that the bio-stabilization potential of submerged beds is a non-linear function of spatial configuration and roughness-element density. Using the clustering index ϕ_c, we distinguish stable and vulnerable regimes: low ϕ_c corresponds to more shielded configurations, whereas higher ϕ_c aligns with more erosion-prone patterns.

These observations potentially align with the hydrodynamic behavior: high-density clusters generate a skimming flow regime that suppresses near-bed turbulence, while medium-density clusters allow deeper turbulence penetration and increased sediment exposure. At intermediate clustering, corresponding to the highest ϕ_c values within our tested range, clusters appear large enough to deflect flow yet close enough to potentially enhance inter-cluster wake-interaction, producing the strongest crest-level turbulence and the highest erosion.

This ϕ_c framework provides a practical tool for evaluating sediment-transport vulnerability. Estimating ϕ_c from imagery or remote sensing can help assess whether a roughness pattern is likely to promote accretion or scour. For nature-based solutions, this highlights the importance of strategic spatial aggregation, designing cluster arrangements that maximize flow shielding while minimizing erosive wake interactions.

References

1. Park, H.; Nepf, H. Turbulence in a Channel with a Patchy Submerged Canopy: The Impact of Spatial Configuration. *J. Fluid Mech.* **2025**, *1006*, doi:10.1017/jfm.2025.12.
2. Coco, G.; Thrush, S.F.; Green, M.O.; Hewitt, J.E. Feedbacks between Bivalve Density, Flow, and Suspended Sediment Concentration on Patch Stable States. *Ecology* **2006**, *87*, 2862–2870, doi:10.1890/0012-9658(2006)87[2862:FBBDFA]2.0.CO;2.
3. Rietkerk, M.; van de Koppel, J. Regular Pattern Formation in Real Ecosystems. *Trends Ecol. Evol.* 2008, *23*, 169–175.
4. Nepf, H.M.; Vivoni, E.R. Flow Structure in Depth-Limited, Vegetated Flow. *J. Geophys. Res. Oceans* **2000**, *105*, 28547–28557, doi:10.1029/2000jc900145.
5. Jacobs, W. Sand-Mud Erosion from a Soil Mechanical Perspective, Technische Universiteit Delft, 2011.

Three-dimensional flow structures identified over three-dimensional dunes with the UB-Lab 3C

Stephen M. Simmons[1], Robert E. Thomas[1], Richard J. Hardy[2], Daniel R. Parsons[3], and Stéphane Fischer[4]

[1] Energy & Environment Institute, University of Hull, Hull, UK. s.simmons@hull.ac.uk; r.e.thomas@hull.ac.uk
[2] Department of Geography, Durham University, Durham, UK. r.j.hardy@durham.ac.uk
[3] Geography and Environment, Loughborough University, UK. d.parsons@lboro.ac.uk
[4] Ubertone, Schiltigheim, France. stephane.fischer@ubertone.fr

Dunes are ubiquitous features on the beds of sandy rivers and have received significant attention. However, there is a dearth of datasets quantifying the velocity and suspended sediment concentration fields above three-dimensional, morphodynamically active, bedforms. This paper reports upon a series of experiments conducted with a three-component Acoustic Concentration and Velocity Profiler, the UBERTONE UB-Lab 3C, sampling velocities and backscatter over three-dimensional mobile dunes in a unidirectional, recirculating, flume. Backscatter data acquired with the ACVP were compared against those acquired with an Aquascat Acoustic Backscatter System and supplemented with bed morphological data collected with 20 Ultrasonic Ranging System probes. Experiments were run for up to four hours. We found a clear improvement in the temporal resolution of the backscatter data acquired with the ACVP compared with the ABS. This improvement, together with three-component velocity data, suggests the presence of large-scale coherent flow structures in the three-dimensional velocity data. Although dunes are often thought of as a 2D phenomenon, the velocity fields above them are strongly three-dimensional, emphasizing the need for an instrument capable of sampling three-component velocities.

Keywords: Acoustic Concentration and Velocity Profiler, dunes, three-component velocities, laboratory flume, mobile beds, acoustic backscatter

1. Introduction

Dunes are the most common bedform on sandy riverbeds and exert a significant control on flow, sediment transport, and the evolution of channel morphology. Their dynamics and morphology have received significant attention over the past 100 years [e.g., 1, 2, 3, 4]. However, their morphology typically comprises three-dimensional topography across multiple scales and, to date, neither experimental nor numerically modelled velocity fields have been obtained over mobile dune beds [4]. To better understand the complex interactions between flow, sediment transport and bedform morphology, there remains a need to measure high-resolution 3-component velocities and suspended sediment concentrations above three-dimensional, morphodynamically active, bedforms.

Sediment-laden flows preclude the application of optics-based techniques such as Particle Image Velocimetry or Particle tracking Velocimetry to quantify velocity fields. Conversely, acoustic-based techniques are ideally suited. Recently, Abroug *et al.* [5] employed a two-component Acoustic Concentration and Velocity Profiler (ACVP; UB-Lab 2C, UBERTONE) to investigate flows over two-dimensional fluvial dunes that migrated under the combined actions of a unidirectional current and monochromatic waves. They measured co-located high-resolution profiles of streamwise (u-) and vertical (w-) velocity components and calculated Reynolds stresses and statistical moments of flow (skewness and kurtosis) in relation to dune geometry. Their downward-looking deployment used a Pulse-Repetition Frequency (PRF) of 900 Hz, with mean velocities derived from 45 consecutive samples giving an acquisition frequency of 20 Hz in 3 mm range bins. Their results demonstrated that migrating dunes can produce non-Gaussian streamwise velocity statistics as a function of location relative to the bedform morphology.

Multiple-frequency ultrasonic Acoustic Backscatter Systems (ABS) have been developed to measure suspended sediment concentration by deriving an average grain size of a suspended sediment grain size distribution throughout the profiling range from an examination of the ratios of backscatter on the different acoustic frequencies [6]. ABS have been deployed in the marine environment [e.g. 7], rivers [e.g. 8] and in laboratory flumes [e.g. 9]. These systems tend to be limited by reverberation effects when deployed in enclosed environments such as a flume, limiting the PRF to a value that prevents the echoes from the previous ping interfering with the next ping. The temporal resolution of the backscatter/concentration profiles is further limited by the need to average across a number of independent samples to reduce the standard error of the profile.

Here, we present some results to quantify velocities and suspended sediment concentration over migrating three-dimensional dune bedforms in a recirculating laboratory flume using a three-dimensional version of UBERTONE's ACVP (UB-Lab 3C). We (a) demonstrate that the UB-Lab 3C is capable of resolving three component velocities over complex mixed two- and three-dimensional bedforms and (b) show synoptic results that demonstrate improved backscatter profiles in comparison to narrowband ABS.

2. Methods

Experiments were conducted in a 10 m long, 0.5 m wide, 0.5 m deep tilting recirculating hydraulic flume (Figure 1) filled with medium sand (d_{50} 850 μm) to an initial thickness of 0.15 m and an initial (still) water depth of 0.2 m. Previous trials had established that two- and three-dimensional dunes would form at an equilibrium gradient of 0.18% and a cross-sectional average velocity of 0.5 to 1.0 m s^{-1}, matching the bedform phase diagram [10]. The flume was run for 18 hours to enable the formation of an equilibrium dune field prior to experimentation. Trials were conducted with the Ubertone UB-Lab 3C installed 6.5 m downstream from the flume outlet over mobile three-dimensional dunes with 20 distributed SeaTek Ultrasonic Ranging System (URS) probes and an Aquascat ABS to independently monitor topography and suspended sediment concentration, respectively.

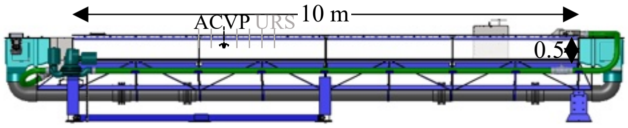

Figure 1. Sketch of the flume. Flow is from right to left. The position of the Ubertone UB-Lab 3C (ACVP) and the 20-probe URS array (URS) are indicated. Please note that experiments with the ABS were not conducted concurrently with those conducted with the UB-Lab 3C.

2.1 Instrument settings

The UB-Lab 3C was set to acquire data within a 300 mm-long profile divided into 200, 1.5 mm-high, bins beneath a blanking distance of 17.3 mm. An acoustic frequency of 1.0 MHz was used for the data presented herein. PRF was set to 1400 Hz, yielding a streamwise-spanwise velocity range of ± 2.072 m s^{-1}. Velocity vectors and backscatter were processed over 60 successive pings to give a profiling rate of 23.33 Hz. The ABS was set to acquire data within a 250 mm-long profile divided into 100, 2.5 mm-high, bins beneath a blanking distance of 38.8 mm. PRF was set to 25 Hz. The instrument internally averaged the backscatter profiles over 64 successive profiles to reduce the standard error of the backscatter measurements, which are Rayleigh distributed for independent samples. The effective profiling rate was therefore 0.39 Hz. The ABS data were corrected for spherical spreading and water attenuation to give backscatter, as a comparison with the output from the UB-Lab 3C software, which was already corrected for spreading and attenuation. The 2 MHz URS probes measured the range to the bed with a resolution of 1 mm every 1 s throughout the duration of the experimental runs to capture the evolution of the bedforms up- and across-stream from the location of the UB-Lab 3C.

2. Results

2.1 Comparison with ABS over a mobile bed

Figure 2 shows the flow speed, derived from the three velocity components, and acoustic backscatter from receive transducer number 2 of the UB-Lab 3C. The bed elevation is determined as the first bin with 90% of the maximum backscatter value, and data from that range are screened out. Over a period of one hour (panels (a) and (b)), several dunes of different amplitude and wavelength migrated past the instrument. Flow speeds were generally higher over bedform crests and lower in the leeside troughs. Elevated acoustic backscatter levels due to higher suspended sediment concentration were often seen in the bedform lee, but also in some locations over bedform crests. High-frequency pulsing of flow and sediment concentration can also be observed and this is highlighted in panels (c) and (d) which show a snapshot of time between 30 and 150 seconds into the acquisition. Higher backscatter levels indicate the entrainment of suspended sediment from the bedform crest and deposition into the low velocity leeside trough.

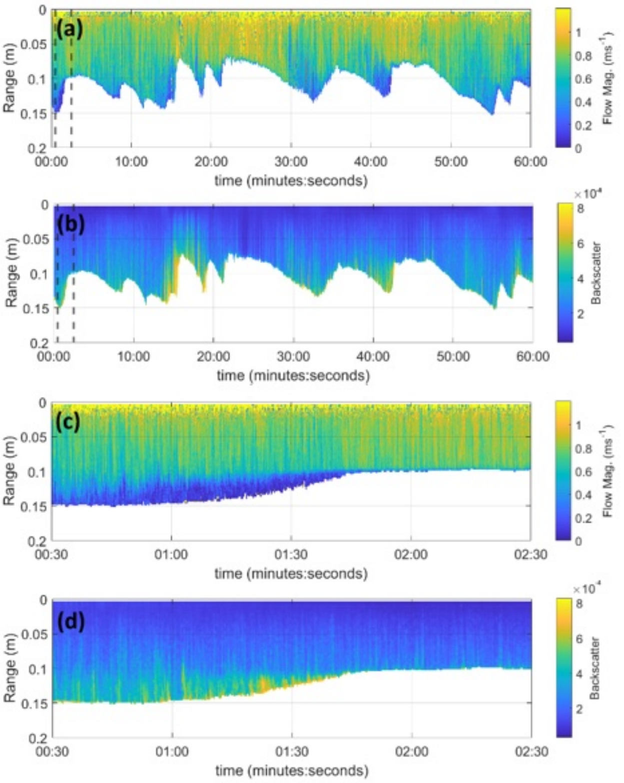

Figure 2. (a) Flow magnitude and (b) backscatter collected over a one-hour period with the UB-Lab 3C emitting at 1MHz. Dashed lines indicate the 120 second snapshot shown in (c) and (d), which focus on a location at and downstream of a bedform crest. Over the one-hour experimental duration, cross-sectional average velocity was 0.645 (range 0.465 to 1.054) m s^{-1}.

As a comparison with the UB-Lab 3C data in Figure 2, Figure 3 shows ABS data acquired during a one-hour acquisition under the same flow conditions at a location further downstream. Panels (a) and (b) show corrected backscatter acquired at acoustic frequencies of 1.85 MHz and 4.0 MHz, respectively. At both frequencies, values of acoustic backscatter tend to be elevated in the leeside troughs, and this can be seen more clearly in panels (c) and (d) which show a 120-second duration snapshot of the data in (a) and (b). Comparison with the UB-Lab 3C data in Figure 2(d) demonstrates a clear improvement in temporal resolution compared with the ABS data over an equivalent sampling duration. Shorter-duration pulses of higher concentration near-bed suspended sediment can be seen in Figure 2(d) that are not adequately resolved with the ABS (Figure 3(d)).

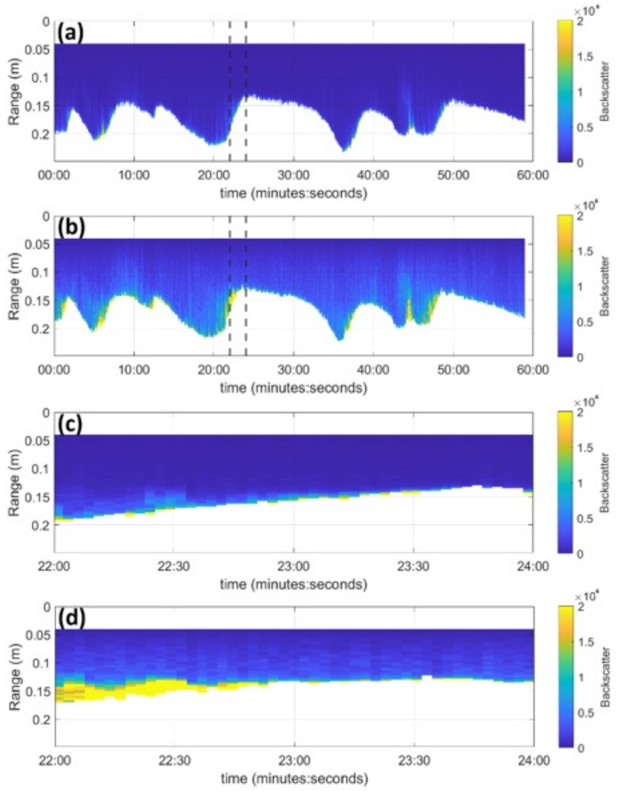

Figure 3. Acoustic backscatter collected over a one-hour period with the Aquascat ABS emitting at (a) 1.85 MHz and (b) 4.0 MHz. Dashed rectangles indicate the 120 second snapshot shown in (c) and (d), which focus on a location downstream of a bedform crest.

2.2 3D flow over a mobile bed

Four hours of continuous UB-Lab 3C data are displayed in Figure 4. A train of approximately 20 bedforms passed through the sampling volume during acquisition. Streamwise velocities (Fig. 4a) show acceleration at bedform crests, and deceleration in the leeside troughs, with some flow-reversal. Negative vertical velocities generally occur immediately downstream of crests, and extend throughout the water depth, from the bed to the water surface (Fig 4c). There is some evidence of occasional ejections of sediment laden fluid at reattachment points (Fig. 4c). Positive spanwise velocities (directed towards the true right of the flume) at bedform crests are balanced by negative velocities (directed towards the true left of the flume) in the following bedform troughs (Fig. 4b), and *vice versa*. These patterns suggest a complex series of interacting coherent structures that are likely forced by the three-dimensional bedform morphology [e.g. 11]. These features would not be captured by a two-dimensional velocimeter measuring streamwise and vertical velocities. It is noticeable that there is a region of decorrelation in the near-field of the probe (Fig. 4) that extends further from the probe in the spanwise component (Fig. 4b). We suspect that this is due to geometric steering of the flow by the ACVP, resulting in lateral shearing within the sampling volume, local acceleration of spanwise velocity, and exceedance of the ambiguity velocity. Figure 5 shows ensemble-averaged streamwise and vertical velocity fields computed for the 20 identified dunes observed in the data. The flow data and bed location are averaged by locating the bedform crests and troughs and then re-sampling by interpolation to a normalised wavelength. The mean bedform morphology clearly relates to the dimensions of a dune. The ensemble average streamwise velocity field (Fig. 5a) indicates that near-bed velocities accelerate over the stoss but then decrease slightly at the crest. This coincides with deceleration from a local vertical velocity maximum at a non-dimensional distance of ~0.7 to a local vertical velocity minimum at and downstream of the crest (Fig. 5c), albeit with a narrow zone of positive vertical velocities, and locally decelerated streamwise velocities, extending predominantly downstream from a non-dimensional distance of ~0.4. Higher up in the water column, streamwise velocities continue to accelerate (Fig. 5a). The spanwise velocity field (Fig. 5b) indicates strongly negative near-bed spanwise velocities on the stoss side, transitioning to positive velocities just upstream of the crest and extending into the lee. However, these regions are isolated to the near-bed region and extend no higher than 5 mm above the bed. Midway down the lee face, spanwise velocities again transition to negative values, followed by a further transition to positive spanwise velocities in the trough. These patterns agree with the conceptual model of [3]. The region of decorrelation in the near-field of the probe (Fig. 5) again extends further from the probe in the spanwise component (Fig. 5b).

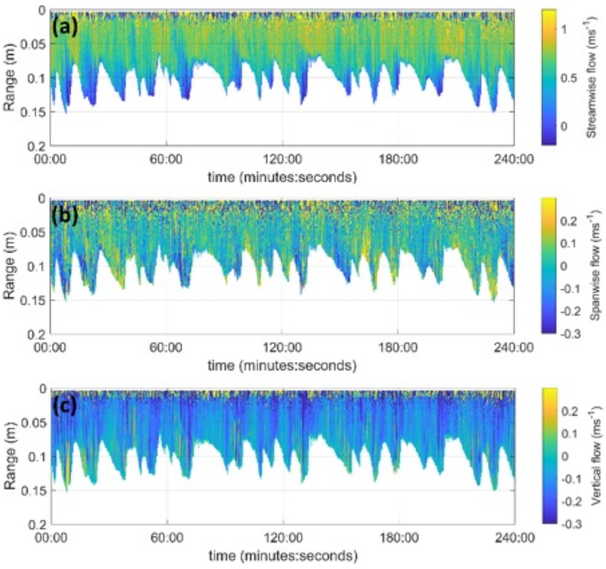

Figure 4. Four hours of UB-Lab 3C data over the mobile sediment bed showing (a) streamwise velocity, (b) spanwise velocity, and (c) vertical velocity. Cross-sectional average velocity was 0.579 (range 0.417 to 0.912) m s^{-1}.

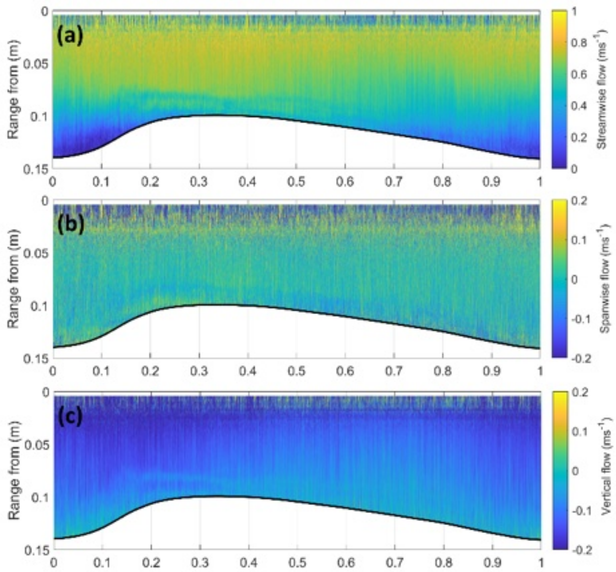

Figure 5 (a) mean streamwise, (b) mean spanwise and (c) mean vertical components averaged over 20 bedforms observed over the four-hour acquisition period. Cross-sectional average velocity was 0.579 (range 0.417 to 0.912) m s^{-1}.

4. Discussion

The data herein help to highlight the feedback between three-dimensional dune morphology and velocity fields, which is key to advancing our understanding of bed form dynamics at a range of spatial scales [3]. Our experimental observations are similar to the experimental observations of Best [11] and field observations of Parsons *et al.* [13], who used aDcp data to suggest a link between crest line shape, vertical velocity fields and separation zone size, and between dune three-dimensionality and crest line curvature of upstream dunes. In particular, our data support the hypothesis of Best [11] that the vertical vortices that form as boils erupt at the water surface are associated with inrushing near-bed fluid.

The backscatter data acquired by the UB-Lab 3C display an improved temporal resolution compared with the ABS instrument. The single frequency of the UB-Lab 3C in this configuration prevents measurement of the median grain size in suspension, whereas the ABS can resolve time-averaged median grain size using an assumption about the shape of the grain size distribution. However, it should still be possible to fit the time-averaged backscatter data to water column samples of concentration and resolve for concentration in the time-series under an assumption that grain size remains constant. There is also a need to determine a near-field correction for the transducers in a similar manner to the monostatic piston transducers used for the ABS [11].

5. Conclusions

The three-component ACVP, the UBERTONE UB-Lab 3C, holds considerable promise for quantifying turbulent velocity fields, suspended sediment concentrations and grain size distributions over morphologically complex regions. Herein, this instrument has been used to shed light on the turbulent flow fields around downstream migrating dune bedforms. Future work aims to:

1. Compare flow fields acquired with the UB-Lab 3C over fixed three-dimensional bedforms with those from a tomographic Particle Tracking Velocimetry system; and
2. Fit the backscatter data recorded by the UB-Lab 3C to sediment concentration samples and compare with derived concentration measurements made by the Aquascat ABS.

References

1. Simons D & Richardson E: Resistance to flow in alluvial channels. USGS Prof. Pap. 422 (1966). DOI: 10.3133/pp422J.
2. Nelson JM & Smith JD: Mechanics of flow over ripples and dunes. J. Geophys. Res. 94 (1989), 8146–8162. DOI: 10.1029/jc094ic06p08146.
3. Best JL: The fluid dynamics of river dunes: A review and some future research directions. J. Geophys. Res. 110 (2005), F04S02. DOI: 10.1029/2004JF000218.
4. Hardy RJ, *et al.*: The influence of three-dimensional topography on turbulent flow structures over dunes in unidirectional flows. J. Geophys. Res. Earth Surf. 126 (2021), e2021JF006121. DOI: 10.1029/2021JF006121.
5. Abroug I, *et al.*: Experimental investigation of the effect of wave-current interactions on the morphology and dynamics of subaqueous dunes. J. Geophys. Res. Earth Surf. 130 (2025), e2023JF007623. DOI: 10.1029/2023JF007623
6. Thorne PD & Hurther D: An overview on the use of backscattered sound for measuring suspended particle size and concentration profiles in non-cohesive inorganic sediment transport studies, Cont. Shelf Res. 73 (2014), 97-118. DOI: 10.1016/j.csr.2013.10.017.
7. Thorne PD, *et al.*: Acoustic scattering characteristics and inversions for suspended concentration and particle size above mixed sand and mud beds, Cont. Shelf Res. 214 (2021), 104320. DOI: 10.1016/j.csr.2020.104320.
8. Vergne A, *et al.*: Using a down-looking multifrequency acoustic backscatter system (ABS) for measuring suspended sediments in rivers, Water Resour. Res. 56 (2020), e2019WR024877. DOI: 10.1029/2019WR024877
9. Wren DG, *et al.*: Measurements of the relationship between turbulence and sediment in suspension over mobile sand dunes in a laboratory flume, J. Geophys. Res. 112 (2007), F03009. DOI: 10.1029/2006JF000683.
10. Southard JB & Boguchwal LA: Bed configuration in steady unidirectional water flows; Part 2, Synthesis of flume data, J. Sediment. Res. 60(5) (1990), 658-679. DOI:10.1306/212F9241-2B24-11D7-8648000102C1865D
11. Best JL: The kinematics, topology and significance of dune-related macroturbulence: Some observations from the laboratory and field, In: Blum MD, *et al.* (eds.) Fluvial Sedimentology VII, Spec. Publ. Int. Assoc. Sedimentol. 35 (2005), 41-60.
12. Downing A, *et al.*: Backscattering from a suspension in the near field of a piston transducer. The J. Acoust. Soc. Am. 97(3) (1995), 1614-1620. DOI: 10.1121/1.412100.
13. Parsons DR, *et al.*: Morphology and flow fields of three-dimensional dunes, Rio Paraná, Argentina: Results from simultaneous multibeam echo sounding and acoustic Doppler current profiling, J. Geophys. Res. 110 (2005), F04S03, doi:10.1029/2004JF000231.

Recent activities in ultrasonic flow measurements for liquid metal Rayleigh-Bénard convection

T. Vogt[1], F. Schindler[1], N. Kim[1], S. Su[2], M. Sieger[1], T. Wondrak[1], S. Eckert[1]

[1] Department of Magnetofluiddynamics, Helmholtz-Zentrum Dresden-Rossendorf (HZDR), Germany
[2] Universite Rouen Normandie, France

For about 10 years, the Department of Magnetohydrodynamics at the HZDR has been increasingly involved in the experimental investigation of Rayleigh-Bėnard convection in liquid metals at very low Prandtl numbers, $Pr \sim 10^{-2}$ - 10^{-3}, which is of great interest for geo- and astrophysics. The thermally driven convective flow dynamics of liquid metals are very different from moderate-*Pr* fluids, such as water. Owing to the large discrepancies in the diffusion of heat and momentum, significant differences between velocity and temperature fields occur. The large-scale convection (LSC) in liquid metals exhibits a significantly more pronounced intermittent behavior and higher turbulence at comparable Rayleigh numbers, *Ra*. Here, the thermal boundary layer (BL) thickness exceeds that of the viscous BL, exposing it to direct interaction with the turbulent flow. It is well-known that the intermittent behavior of the viscous and thermal BL's increase significantly at small *Pr*. The viscous BL in a liquid metal becomes turbulent at smaller *Ra* than comparable convection in gases or water. Thus, a stronger influence of the LSC on the thermal BL thickness and, furthermore, on the local properties of the heat transport is likely.

While conventional optical measurement methods do not work in opaque liquid metals, the ultrasonic Doppler method has proven to be a very effective tool for flow characterization in liquid metal convection. Here, we present investigations in cylindrical convection cells of aspect ratio 1 and 0.5 as well as in a rectangular cell with a square base area of 1 m^2 and an aspect ratio of 25. Our flow measurements demonstrate that the reduction of the aspect ratio in the cylindrical cells increases the volatility of the LSC, one can even describe this as a collapse of the coherent LSC. Here, the single-roll structure of the LSC alternates in short succession with double-roll and triple-roll structures in time periods smaller than the turn-over time. Temperature measurements within the thermal BL reveal strong fluctuations of the BL thickness and increasing deviation from the Prandtl–Blasius–Pohlhausen profile with increasing *Ra*. Furthermore, we will show measurements of the temperature and velocity fields in the shallow convection cell. These experiments focus on the search for so-called turbulent superstructures with their special characteristics in low-*Pr* fluids. Here too, the use of ultrasound Doppler technology is a key factor in identifying the flow pattern and tracking its dynamics.

Identification of Flow States in the DRESDYN Precession Experiment Using Ultrasound Doppler Velocimetry

Kunal K. Jani[1], André Giesecke[1], Thomas Gundrum[1], Frank Stefani[1]

[1] Magnetohydrodynamics in Geophysics and Astrophysics, Institute of Fluid Dynamics, Helmholtz-Zentrum Dresden-Rossendorf, Bautzner Landstraße 400, 01328 Dresden, Germany.

The precession-driven flow in a rapidly rotating cylinder undergoes abrupt, hysteretic transitions between inertial mode states. Using a 1:6 downscaled water model of the DREsden Sodium DYNamo (DRESDYN) precession experiment, transition thresholds are identified for the appearance of an axisymmetric double-roll circulation (m_0k_2) from the Kelvin-mode dominated state (m_1k_1). Nine Ultrasound Doppler Velocimetry (UDV) transducers provide axial velocity profiles, decomposed via Fast Fourier Transform-based and block-wise modal analysis as the Poincaré number (Po) is swept at fixed Reynolds number (Re) using stepwise and continuous ramping protocols. Velocity modal amplitudes, end-cap pressure harmonics, and three-phase electrical power all consistently identify a hysteretic transition whose onset and recovery thresholds differ with the direction of the Po sweep. The double-roll state is metastable, persisting when Po is held within the transitional interval, and carries a measurably higher energetic cost than the Kelvin-mode regime. Comparing modal amplitudes across the distributed UDV network further enables reconstruction of the global flow organisation, providing a robust multi-diagnostic framework for identifying and characterising flow state transitions relevant to the forthcoming DRESDYN sodium experiment.

Keywords: Experimental Fluid Mechanics, Axial Precession, Inertial Modes, Hysteresis, Ultrasound Doppler Velocimetry (UDV)

1. Introduction

Precessing flows occur when a rotating container filled with liquid changes the orientation of its rotation axis over time. In this configuration, the fluid experiences both the usual Coriolis force and a time-dependent Poincaré force due to the precessional motion. This leads to a three-dimensional flow, strongly constrained by rotation, and supports a spectrum of inertial waves that can cascade into instabilities and eventually turbulence [1-3]. Beyond their fluid-dynamical interest, precession-driven flows are significant for engineering applications, such as efficient mixing of viscous fluids, and for geophysical and astrophysical systems.

In geophysics, precession has been proposed as a potential energy source for planetary dynamos, with the Earth's and the ancient lunar core's precession potentially driving large-scale flows and magnetic field generation [4-6]. These considerations have motivated laboratory experiments and numerical models exploring precession's role in driving large-scale flows and magnetic field generation.

The DRESDYN (DREsden Sodium facility for DYNamo and thermohydraulic studies) [7,8] program at Helmholtz-Zentrum Dresden-Rossendorf is aimed at conducting experiments to study precession-driven liquid sodium dynamos. In this context, a precession-driven liquid sodium dynamo experiment is being commissioned, where a large cylindrical vessel with aspect ratio $\Gamma = 2$ (radius $R = 1$ m, height $H = 2$ m) will rotate rapidly while precessing at a substantial angle between the rotation and precession axes. The present work focuses on the identification of flow states for the DRESDYN precession experiment, with a preliminary focus on using a distributed network of Ultrasound Doppler Velocimetry (UDV).

2. Water Precession Experiment

2.1 Setup

The mini-water experiment, shown in figure 1, is a 1:6 scale model of the DRESDYN precession experiment and serves as a test bed to understand the flow states that arise in precessional motion and to develop measurement and analysis techniques before the sodium experiment becomes operational. The setup consists of a rotating acrylic cylinder of aspect ratio $\Gamma = 2$ (radius $R = 163$ mm and height $H = 326$ mm) filled with distilled water as the test fluid mixed with tracer particles for UDV.

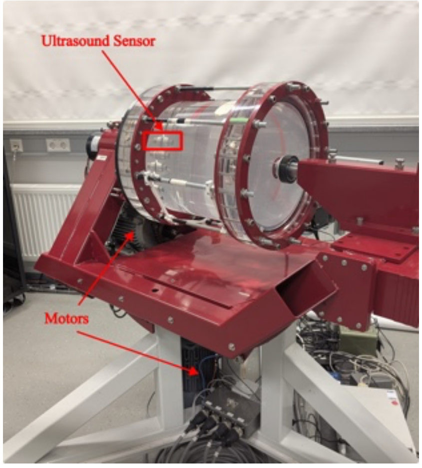

Figure 1: Setup of Water Precession Experiment at DRESDYN

A frame structure with solid screw clamps at the end caps running parallel to the side-wall provides stability and tightness. The cylinder rotation is powered by an asynchronous motor (maximum power 3600 W) and the turntable rotation for precession is powered by another asynchronous motor (maximum power 2200 W). Thus, both motors can be controlled independently with a maximum rotation frequency of $f_c \leq 10$ Hz and a maximum precession frequency of $f_p \leq 1$ Hz. Assuming the kinematic viscosity of distilled water as $\nu = 10^{-6}$ m^2/s, the maximum achievable Reynolds number ($\mathrm{Re} = \Omega_c R^2/\nu$) is of the order 2×10^6. The precession ratio (Poincaré Number) is defined as $\mathrm{Po} = \Omega_p/\Omega_c$. The nutation angle α describes the relative orientation of the rotation axes Ω_c and Ω_p and is kept at 90° for the scope of this study.

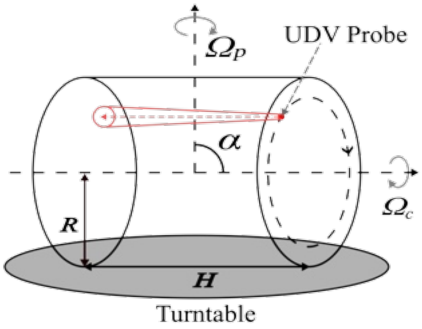

Figure 2: Schematic of the 1:6 downscaled water model

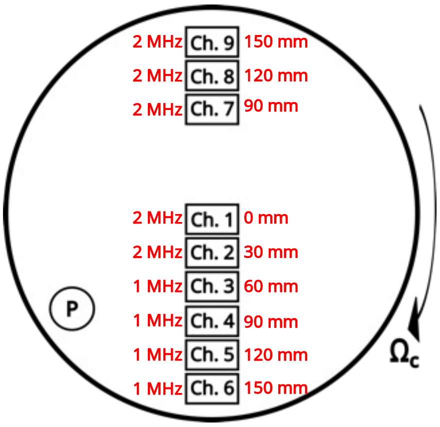

Figure 3: Position of the UDV channels and pressure sensor P on the cylinder end cap

For flow field measurements, velocity is measured using UDV as shown in figure 2. Nine ultrasound transducers (channels) are placed on one end cap of the cylinder. Each of these transducers can produce an ultrasound beam parallel to the cylinder's axis of rotation, enabling the measurement of axial velocity profiles. The position and characteristics of the ultrasound sensors are shown in figure 2. A pressure sensor is placed at radial position r = 150 mm on the same end cap. Power is calculated by measuring the current and voltage from the linear amplifiers of the motors for each of the three phases separately.

2.2 Measurement Techniques

Building on prior characterisations [9-11] of inertial modes and their dependence on the Poincaré number and Reynolds number this work targets the transition regimes, associated hysteresis and the emergence of large-scale structures. Particular focus is given to the axisymmetric double-roll mode (azimuthal wave number $m = 0$, and axial wave number $k = 2$), which can be linked to the onset of dynamo action [12]. The upper and lower transition thresholds in Poincaré number for different Reynolds numbers remained insufficiently constrained in previous investigations, yet are essential for the forthcoming DRESDYN experiment.

To probe path dependence and hysteresis in the transitional regime, two control protocols are applied that keep Re fixed while sweeping Po both upward and downward. In the first protocol, a stepwise averaging approach, six Poincaré numbers are selected spanning the laminar, transitional, and turbulent regimes. The experiment begins at the lowest Po with a ten-minute settling period to reach a quasi-steady state, after which axial velocity profiles are recorded for ten minutes, yielding smooth ensemble-averaged profiles suitable for identifying the double-roll mode. The Poincaré number is then incremented stepwise, with five-minute settling intervals between steps. Once the highest Po is reached, the sweep is reversed, thereby constituting a hysteresis study in which transition thresholds are compared between the ascending and descending branches.

The second protocol employs a continuous ramping strategy, in which Po is varied smoothly through the laminar, transitional, and turbulent regimes and back, following an initial ten-minute settling period at the lowest value. This allows uninterrupted monitoring of the flow as the forcing parameter traverses all dynamic states, without the discretisation inherent to stepwise protocols. Different ramp rates are tested to balance temporal fidelity with the flow adjustment timescale, identifying an optimal configuration for capturing the onset, development, and decay of coherent structures. A further variant of this approach involves pausing the ramp within the transitional regime, enabling direct assessment of whether the double-roll mode can be sustained at a fixed Po or whether it spontaneously evolves into an alternative flow state.

Throughout both protocols, UDV measurements are synchronised with end-cap pressure sensors and three-phase electrical power measurements of the drive motors. Simultaneous acquisition of these diagnostics allows flow transitions to be correlated with changes in mechanical power consumption, providing complementary insight into the effective dissipation associated with each flow regime. This multi-diagnostic approach is particularly valuable at higher Reynolds numbers, where UDV signal-to-noise ratios decrease and the power and pressure signals offer a more robust means of identifying regime transitions reliably.

2.3 Analysis Techniques

The axial velocity profiles $u_z(t_n, z_i)$ acquired by the UDV channels are first cleaned by a median-filter echo removal step, after which they are projected onto axial sine modes. Interpolating each cleaned profile onto a uniform axial grid of N_z points, the type-I discrete sine projection gives the k-th axial modal coefficient

$$\hat{u}_k(t_n) = \frac{2}{N_z - 1} \sum_{q=0}^{N_z - 1} \tilde{u}_z(t_n, z_q) \sin\left(\frac{qk\pi}{N_z - 1}\right) \qquad (1)$$

where $\tilde{u}_z$ denotes the echo-cleaned field. This becomes the basis of two techniques of amplitude analysis.

For the Fast Fourier Transform-based approach, the key flow state diagnostics are defined from the one-sided amplitude spectrum $A_k(f)$ as: $m_1k_1 = \max A_{k=1}(f)$ and $m_0k_2 = A_{k=2}(0)$. Here m_1k_1 tracks the oscillatory amplitude of the directly forced Kelvin mode ($m = 1$, $k = 1$), while m_0k_2 measures the mean axisymmetric double-roll contribution ($m = 0$, $k = 2$).

For slowly evolving flows, a period-locked block-wise decomposition is used instead, computing block-averaged means and RMS amplitudes over successive windows of N_{per} rotor periods, which resolves the slow hysteretic evolution as Po is swept.

The end-cap pressure is demodulated in synchronisation with the cylinder rotation. Using the rotor synchronisation edges to reconstruct the instantaneous phase $\varphi(t)$, blockwise harmonic amplitudes are computed as $|m|^{(k)} = (a^2_m + b^2_m)^{1/2}$, where a_m and b_m are the cosine and sine projections of the fluctuating pressure onto the m-th harmonic of the rotor phase within each block.

The total three-phase electrical power is computed as $P_{tot}(t) = \Sigma\, S\, U_Ø\, I_Ø$, summed over phases $Ø \in \{A, B, C\}$, where S is a calibration scale factor. The period-averaged power $\langle P_{tot} \rangle$ is reported alongside the velocity and pressure diagnostics throughout this study, enabling direct assessment of the energetic cost associated with each flow regime.

3. Results

3.2 Time Averaged Amplitude

Measurements at fixed Re = 1 × 10^5 sweep Po upward and downward (figure 4). As Po increases into the transitional interval, m_1k_1 collapses while m_0k_2 grows. On the down-sweep, m_0k_2 persists to substantially higher value at the Po where growth was observed for up-sweep, producing a pronounced separation between the two branches. This confirms that the observed flow state depends on the direction of the parameter sweep and the presence of hysteresis.

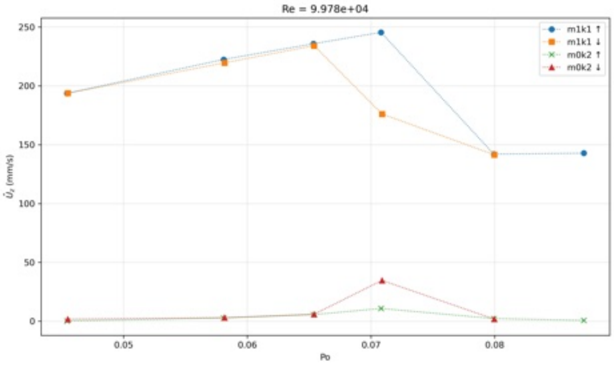

Figure 4: Fixed Re = 1 x 10^5 at r = 150 mm (Channel 6): modal amplitudes as functions of Po for increasing and decreasing Po

3.2 Block-wise Decomposed Amplitude

The continuous ramping protocol at Re = 2 × 10^5 resolves the same transition observed in figure 4 at finer temporal detail (figure 5). m_1k_1 drops sharply upon entering the transitional interval, while m_0k_2 rises appreciably only on the descending branch, consistent with the hysteretic separation seen in section 3.1. Holding Po fixed within the transitional interval shows the double-roll state to be metastable, persisting without spontaneously reverting to the Kelvin-mode dominated state. The period-averaged (here N_{per} is taken as 1) power rises as Po increases into the transitional interval, stabilises at an elevated level while the double-roll state is sustained during the hold, and drops sharply once Po is reduced and m_0k_2 collapses confirming that the double-roll regime carries a measurably higher energetic cost than the Kelvin-mode dominated state.

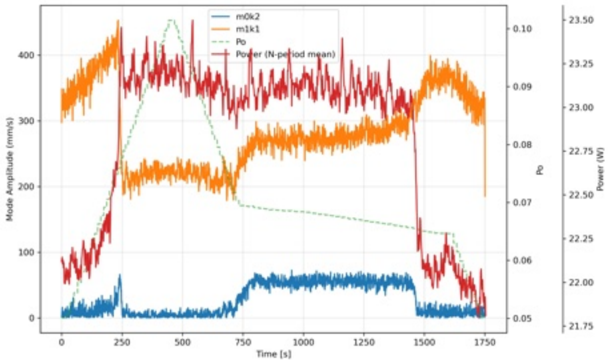

Figure 5: Sustained double-roll at Re = 2 x 10^5 (at r = 150 mm; Channel 6) with a stepwise Po protocol and a subsequent hold within the transitional interval. m_1k_1, m_0k_2, Po(t), and the period-averaged total three-phase power are shown.

3.3 Pressure

Figure 6 shows harmonic pressure amplitudes alongside continuous ramping Po for a full ramp at Re = 2 × 10^5. At low Po the signal is sporadic; as Po rises, the first harmonic grows slowly before collapsing sharply at the transition. On the downward sweep, the amplitude recovers as the flow re-enters and exits the transitional regime. The pressure diagnostics independently confirm the double-roll transition identified from velocity, and the sweep-direction dependence corroborates the metastability of the transitional regime. The zeroth harmonic follows an oscillatory behavior throughout the experimental run, independent of the Po, only showing small drop or small rise when it enters and exits the transition regime during the up-sweep and down-sweep respectively.

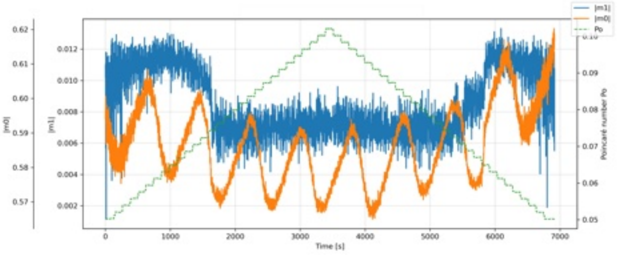

Figure 6: Harmonic pressure amplitudes for Re = 2×10^5

4. Summary

A 1:6 downscaled water model of the DRESDYN precession experiment is used to identify flow states and transition thresholds in precession-driven flow. The setup employs nine UDV transducers on the cylinder end cap to measure axial velocity profiles, complemented by end-cap pressure sensing and three-phase electrical power monitoring. Two control protocols: stepwise averaging and continuous ramping, sweeping the Poincaré number (Po) at fixed Reynolds number (Re) in both directions, targeting the hysteretic transition between the Kelvin-mode dominated regime (m_1k_1) and the axisymmetric double-roll circulation (m_0k_2). Modal amplitudes are extracted via FFT-based and block-wise decomposition techniques, while pressure harmonics are obtained through rotor-synchronised demodulation, enabling a fully corroborated multi-diagnostic characterisation of each flow regime.

At all inputs, all three quantities: velocity, pressure, and electrical power, consistently identify a hysteretic transition between the Kelvin-mode and double-roll states whose onset and recovery differ depending on the direction of the Po sweep. The double-roll mode, once established, is shown to be metastable, persisting when Po is held within the transitional interval. By cross-correlating the velocity modal amplitudes, harmonic responses of pressure, and power consumption across both ascending and descending sweeps, precise upper and lower thresholds of the transitional regime can be defined. This multi-diagnostic approach provides a robust framework for reliably identifying flow state transitions, particularly at higher Re where UDV signal quality degrades and pressure and power signals serve as independent indicators. The distributed network of UDV channels at different radial positions provides spatially resolved velocity information across the cylinder. Comparing modal amplitudes across channels allows the spatial structure of each flow regime to be reconstructed. This enables the global flow organisation within the cylinder, whether Kelvin-mode dominated, transitional, or double-roll, to be identified and tracked as forcing parameters evolve.

Acknowledgments

This project has received funding from Deutsche Forschungsgemeinschaft (DFG) under the research project 532905681 "Real-time identification of flow states in the DRESDYN precession experiment using distributed ultrasound sensors".

References

[1] McEwan AD: Inertial oscillations in a rotating fluid cylinder, J. Fluid Mech. 40 (1970), 603.

[2] Manasseh R: Breakdown regimes of inertia waves in a precessing cylinder, J. Fluid Mech. 243 (1992), 261.

[3] Herault J, et al.: Subcritical transition to turbulence of a precessing flow in a cylindrical vessel, Phys. Fluids 27 (2015), 124102.

[4] Malkus WVR: Precession of the Earth as the Cause of Geomagnetism, Science 160 (1968), 259.

[5] Loper DE: Torque balance and energy budget for the precessionally driven dynamo, Phys. Earth Planet. Int. 11 (1975), 43.

[6] Tilgner A: Precession driven dynamos, Phys. Fluids 17 (2005), 034104.

[7] Giesecke A, et al.: Numerical simulations for the DRESDYN precession dynamo, Magnetohydrodynamics 51 (2015), 293.

[8] Stefani F, et al.: Towards a precession driven dynamo experiment, Magnetohydrodynamics 51 (2015), 275.

[9] Giesecke A, et al.: Kinematic dynamo action of a precession-driven flow based on the results of water experiments and hydrodynamic simulations, Geophys. Astrophys. Fluid Dyn. 113 (2019), 235.

[10] Giesecke A, et al.: The global flow state in a precessing cylinder, J. Fluid Mech. 998 (2024), A30.

[11] Gundrum T. et al.: Nonlinear large-scale flow transition in a precessing cylinder and its potential for hydromagnetic dynamo action. ISUD14 Conference Proceedings, (2023).

[12] Giesecke A, et al.: Nonlinear large scale flow in a precessing cylinder and its ability to drive dynamo action, Phys. Rev. Lett. 120 (2018), 024502.

FUNDAMENTAL STUDY ON ULTRASONIC PULSE RECEPTION BASED ON LIGHT DEFLECTION EFFECTS

Riku Hirai[1], Shuntaro Kozaka[1], Weichen Zhang[2], Hiroshige Kikura[2], Naruki Shoji[3], Hideki Kawai[3]

[1] Institute of Science Tokyo, Tokyo, Japan
[2] Laboratory for Zero-Carbon Energy, Institute of Integrated Research, Institute of Science Tokyo, Tokyo, Japan
[3] Muroran Institute of Technology, Hokkaido, Japan

This research explores the feasibility of an ultrasonic receiver relying on a photoacoustic probe for the in-situ observation of fuel debris at the Fukushima Daiichi Nuclear Power Plant (1F). Throughout the dismantling process, standard optical cameras and piezoelectric transducers encounter severe hurdles caused by elevated radiation, cutting-induced opacity, and limited reach. To bypass these barriers, we concentrate on a photoacoustic approach capitalizing on the optical deflection phenomenon, mapping ultrasonic waves to refractive index shifts within a laser beam. This design yields a broad bandwidth and genuine omnidirectional sensitivity without requiring electronic components in the sensor head. This manuscript assesses the setup's resilience in murky water. A solid-type probe equipped with a protective casing was introduced and effectively preserved a strong waveform correlation (R=0.74) in highly turbid environments (400 ppm), significantly outperforming standard open-type counterparts. Additionally, the concurrent observation of the surrounding environment via Ultrasonic Velocity Profiling (UVP) was examined, successfully mapping both the target's profile and the adjacent fluid dynamics. These outcomes illustrate that the presented architecture is exceptionally viable for consistent, real-time acoustic sensing in the cloudy, severe conditions inherent to 1F decommissioning.

Keywords: Photoacoustic probe, Ultrasonic reception, Fuel debris, Decommissioning, UVP

1. Introduction

The extraction of fuel debris stands as a paramount and formidable challenge throughout the decommissioning phase of the Fukushima Daiichi Nuclear Power Plant (1F). Recent initiatives are transitioning toward both experimental and full-scale debris removal utilizing extended robotic arms. However, the mechanical cutting and processing of these materials will unavoidably produce massive volumes of particulate matter and cloudy water. Moreover, the reactor's interior features exceptionally high radiation doses, severely restricting human entry and shortening the functional life of standard electronics. As a result, standard optical cameras used for visual tracking, along with typical piezoelectric acoustic sensors, frequently encounter profound measurement obstacles stemming from hardware degradation and constrained reach.

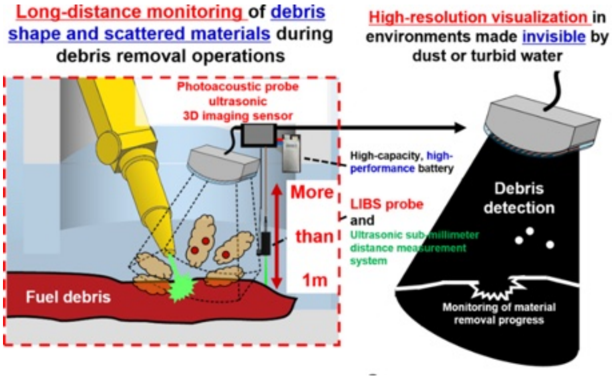

Figure 1: Conceptual diagram of long-distance monitoring for fuel debris shape and scattered particles during retrieval operations using a photoacoustic ultrasonic imaging sensor.

Although standard acoustic imaging methods relying on divergent wave emission and the Synthetic Aperture Focusing Technique (SAFT) are utilized to survey underwater geometries, they encounter significant limitations over extended distances. SAFT determines the spatial positioning of reflectors by mapping the received signal strength against acoustic transit times. Yet, as the measurement range expands, focal point ambiguity rises, leading to blurred image reconstructions and a drastic reduction in azimuthal clarity. Enhancing this resolution theoretically dictates an expansion of the aperture dimensions to broaden the acceptance angle. Despite this, standard piezoelectric transducers exhibit intrinsic mechanical directivity, restricting their ability to capture echoes beyond their predefined sensitivity cones, regardless of physical aperture enlargement.

Consequently, engineering an omnidirectional acoustic receiver is absolutely vital for realizing high-fidelity, long-range visualization within these extreme settings. To bypass the directivity constraints native to standard devices, this research emphasizes an ultrasonic receiver utilizing a photoacoustic probe. This core mechanism senses acoustic waves by monitoring refractive index shifts within a projected laser beam.

2. Principle of the Photoacoustic Probe

The foundational concept of this architecture capitalizes on the localized density variations induced in a fluid as acoustic waves travel through the medium.

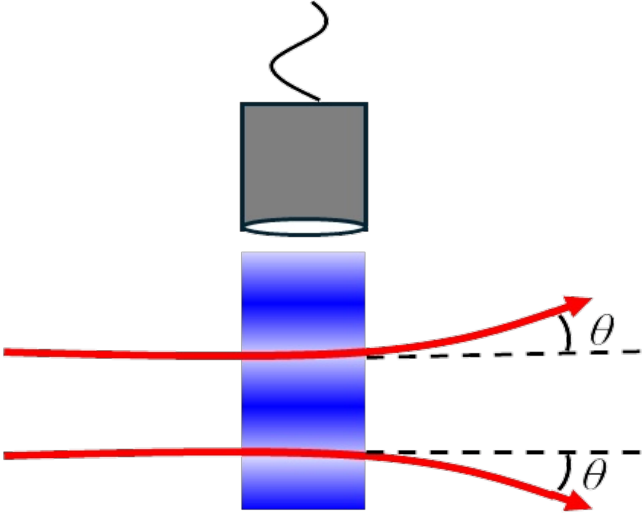

Figure 2: Schematic diagram of the optical deflection phenomenon.

As a laser traverses this sound field, the regional density shifts force the light to experience momentary refraction, an effect termed the optical deflection phenomenon (Figure 2). By accurately positioning an optical fiber along the beam's axis, the apparatus records ongoing fluctuations in light intensity as the acoustic pulses cross the target zone.

These shifts in optical power are subsequently channeled via the receiving fiber into a photoelectric converter and a high-pass filter, enabling the precise recreation of the initial acoustic waveform. Since this technique apprehends sound via optical means, it functions completely independent of the mechanical and structural directivity boundaries governing classic transducers. Such a configuration delivers authentic omnidirectional receptivity and an intrinsically broad frequency spectrum. Additionally, because the submerged sensor head houses solely optical elements without vulnerable electronic parts, it is uniquely qualified for reliable, sustained deployment within the intensely radioactive spaces typical of the 1F primary containment vessels.

3. System Configuration and Fabrication

Drawing on the aforementioned acousto-optic theory, we constructed prototype sensors to practically assess their baseline receiving capabilities. The primary hardware of the prototype incorporates a semiconductor laser functioning as the illuminator, a right-angle prism for steering and reflecting the beam, optical fibers for transmitting and receiving light across the remote sensor head, and a photodetector unit. This photodetector links to an analog-to-digital converter alongside an oscilloscope, facilitating rapid signal capture and data digitization.

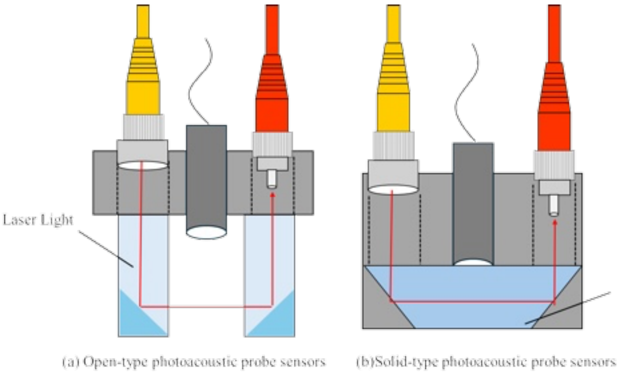

(a) Open-type photoacoustic probe sensors (b)Solid-type photoacoustic probe sensors

Figure 3: Schematic diagram of the photoacoustic probe sensors: (a) Open-type photoacoustic probe sensor, (b) Solid-type photoacoustic probe sensor.

To guarantee adaptability and durability across diverse testing conditions, we engineered two separate sensor designs—specifically, an open-type and a solid-type—as depicted in Figure 3. The open-type variant presents a straightforward layout wherein the optical probe beam passes straight through the ambient fluid (water). This direct contact permits the highly responsive, omnidirectional capture of acoustic pulses.

Nevertheless, in severely murky fluids, floating particulates can scatter and absorb the exposed laser, deteriorating the overall signal-to-noise ratio. To mitigate this drawback, the solid-type photoacoustic receiver was formulated. Within this setup, a Dove prism fulfills a twofold role: it spatially directs the optical trajectory while concurrently serving as a physical shield for the sensing light. This guarantees that the emitted laser reaches the receiving optics safely, avoiding direct contact with the cloudy external fluid. Such a sealed architecture is explicitly designed to minimize the drastic light attenuation induced by external particle interference, thereby securing highly steady acoustic reception even in optically impenetrable liquids.

4. Performance Evaluation in Turbid Water

To systematically gauge the effect of dense turbidity on the captured acoustic waveforms, an experimental rig was assembled featuring an acrylic block—acting as a baseline specular reflector—positioned at the base of a tank containing artificially clouded water.

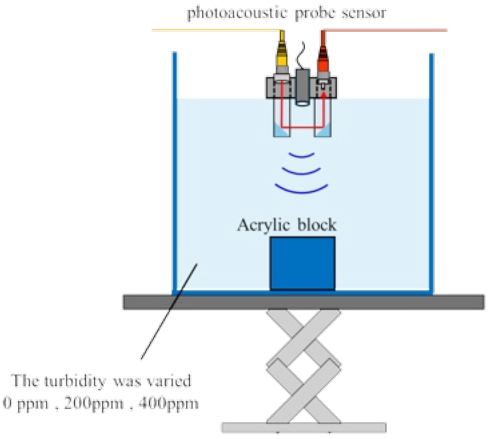

Figure 4: Schematic of the experimental setup for evaluating the

performance in turbid water.

Field observations from the 1F dismantling sites reveal that standard camera visibility is often restricted to mere centimeters owing to floating debris and iron oxides. To faithfully replicate this extreme optical obstruction, the peak particulate concentration for this trial was established at 400 ppm.

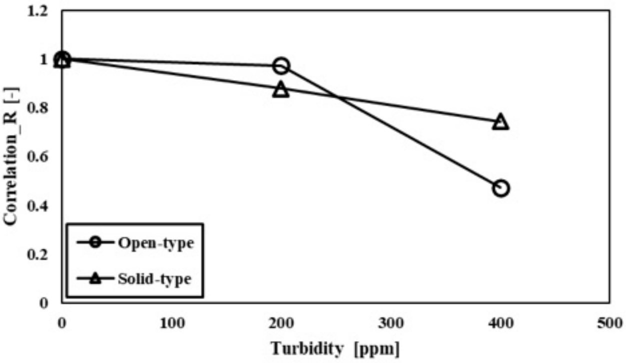

Figure 5: Relationship between turbidity and waveform correlation coefficient.

To measure the extent of signal loss, the normalized cross-correlation (Correlation R) for the acquired waveforms was computed against a reference signal recorded in pristine water (0 ppm). As demonstrated in Figure 5, the open-type sensor's correlation coefficient R sustained a strong level of 0.97 up to a 200 ppm concentration. However, its efficacy declined abruptly, falling to an R value of merely 0.47 at the 400 ppm mark. This substantial decrease physically signifies that the phase data and amplitude of the incoming wave suffered severe distortion from scattering interference and light attenuation driven by the dense particulate matter.

In contrast, the solid-type instrument exhibited outstanding durability, preserving an R value of 0.74 even at the peak 400 ppm turbidity. By securing the optical route inside the Dove prism, the solid-type variant effectively neutralized the scattering impacts. These numerical outcomes conclusively validate that the solid-type receiver facilitates the dependable capture of acoustic waves with markedly greater consistency, establishing its effectiveness as a durable diagnostic instrument in severe, murky aquatic environments where traditional optics break down.

5. Simultaneous Measurement of Target Shape and Ambient Flow Field

Throughout the real-world extraction of fuel debris, mechanical cutting procedures will trigger intricate fluid dynamics and thermal-hydraulic shifts. Consequently, monitoring the ambient fluid environment concurrent with debris shape profiling was explored by incorporating Ultrasonic Velocity Profiling (UVP) into the developed photoacoustic framework. We concurrently executed target echo logging via an open-type photoacoustic sensor and UVP fluid tracking via a conventional acoustic transducer inside a voluminous water tank. Although future trials are planned using mock debris featuring intricate shapes to more accurately simulate reactor internals, this preliminary phase employed a stone block possessing a basic surface finish as the focal target.

To physically emulate the turbulent fluid conditions anticipated during cutting and coolant circulation, an angled water stream aimed directly over the block was created using a side-mounted hose and pump system. Positioned above the target, the combined sensor apparatus was utilized to synchronously record the stone's surface echoes and map the spatiotemporal velocity gradients through UVP. Gathering surface echoes for topographical assessment required mechanically sweeping the target zone, spanning a spatial range from -40 mm to 40 mm across the horizontal x-axis with 1 mm step precision. Simultaneously, UVP sampling was performed at five predetermined, strategic coordinates along this trajectory: -40 mm, -20 mm, 0 mm, 20 mm, and 40 mm.

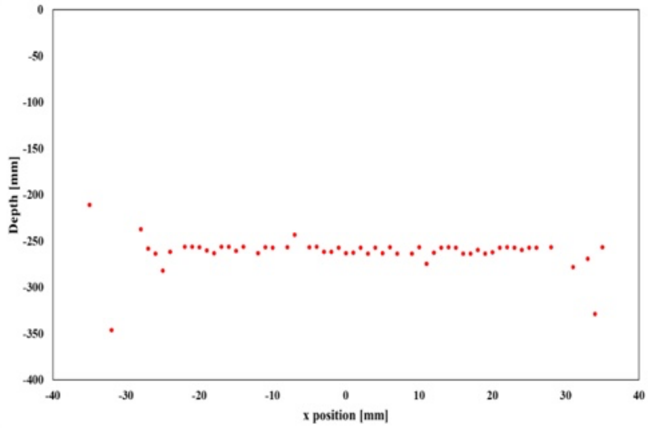

Figure 6: Spatial distribution of the reflection signals obtained by the photoacoustic probe.

Figure 6 illustrates the spatial mapping of the echo signals captured by the photoacoustic instrument over the scanned region. Robust echo signatures were consistently and distinctly acquired precisely at the depth matching the block's exterior boundary. This verifies that, regardless of the active fluid turbulence, the target's boundary and fundamental macroscopic relief were reliably and accurately mapped leveraging the optical deflection principle.

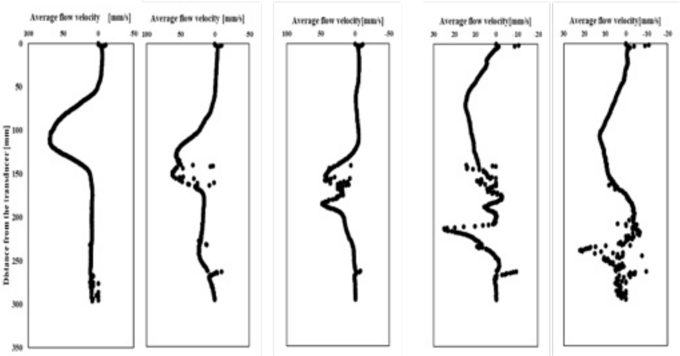

Figure 7: Results of the UVP measurements at the specified positions.

Figure 7 portrays the in-depth findings from the associated UVP assessments. Clear velocity signatures, unmistakably corresponding to the propelled water jet from the hose, were effectively detected. In the zones immediately following the hose outlet, the aquatic flow proved highly erratic, displaying substantial velocity shifts and broad turbulence directly over the target. Yet, as this fluid structure progressed laterally toward the left edge of the monitored space, the flow pattern progressively steadied, allowing the primary upward-directed flow component to be easily recognized.

Based on these thorough findings, we have effectively validated the foundational viability of a fully integrated platform that synchronously conducts accurate shape modeling via a photoacoustic receiver and dynamic fluid tracking via UVP. Although this early proof-of-concept phase relied on streamlined techniques for both topographical plotting and UVP data handling, we anticipate that more sophisticated upgrades—including 3D flow reconstruction and the integration of the solid-type probe into this joint array—will be essential for impending field applications.

6. Performance Evaluation in Turbid Water

This research comprehensively examined a diagnostic framework employing a solid-type photoacoustic receiver, assessing its capacity to deliver stable and dependable acoustic readings within the intensely turbid settings projected for nuclear site dismantling. Empirical trials verified that the suggested solid-type instrument preserved an exceptionally high waveform correlation ($R=0.74$) even when subjected to an extreme 400 ppm turbidity level. Under these same conditions, marked signal decay and phase warping were noted in the standard open-type device, highlighting the superior resilience of the shielded optical pathway architecture.

Additionally, the innovative merging of UVP technology with the photoacoustic detection array highlighted the vital capacity for real-time observation of the adjacent thermal-hydraulic environment concurrently with debris profiling. These discoveries firmly propose that the integrated platform can function as a highly proficient, radiation-hardened instrument for in-situ observation within the visually blocked and physically punishing conditions typical of 1F cleanup efforts.

Regarding upcoming deployments, the native wideband properties of the photoacoustic receiver will be extensively exploited. By incorporating frequency-multiplexed acoustic emission methods, we intend to engineer a sophisticated wideband three-dimensional (3D) visualization array to attain substantially finer azimuthal resolution and expanded spatial reach. Subsequent experimental endeavors will likewise encompass thorough validations utilizing more intricate debris geometries and active fluid scenarios that better reflect the true internal reactor atmosphere.

References

[1] Zhang K, et al.: Towards safe, efficient long-reach manipulation in nuclear decommissioning: a case study on fuel debris retrieval at Fukushima Daiichi, J. Nucl. Sci. Technol. 62 (2025), 1-16.

[2] Porcheron E, et al.: Fukushima Daiichi fuel debris retrieval: Results of aerosol characterization during laser cutting of non-radioactive corium simulants, J. Nucl. Sci. Technol. 58 (2021), 87-99.

[3] Shoji N: High-resolution, wide-area underwater object shape imaging using ultrasonic diverging wave transmission and laser-deflection-based echo reception, Meas. Sci. Technol. 36, no. 10, 105113, 2025.

[4] Editorial Committee of Ultrasound Handbook, Ultrasound Handbook, Maruzen Publishing, 2010 (in Japanese).

[5] The Society of Materials Science, Japan, Ultrasound and Materials, Advanced Materials Series, 2010 (in Japanese).

Experimental study of ultrasound-driven jets in liquid metal

Elio Guillon[1,2], Sophie Miralles[1], Valéry Botton[1], Gilles Despaux[3], Emmanuel LeClézio[3], Sven Eckert[4], Klaus Timmel[4]

[1] INSA Lyon, CNRS, Ecole Centrale De Lyon, Universite Claude Bernard Lyon 1, LMFA, UMR5509, 69621, Villeurbanne France.
[2] Fluid and Complex Systems Research Center, Coventry University, Coventry CV15FB, United Kingdom
[3] IES, Univ Montpellier, CNRS, Montpellier, France.
[4] Institute of Fluid Dynamics, Helmholtz-Zentrum Dresden-Rossendorf, 01328 Dresden, Germany

We present velocity measurements of jets driven by ultrasound beams in the eutectic alloy GaInSn. To our knowledge, this is the first direct quantification of acoustic streaming flow in a liquid metal. Acoustic streaming in liquid metals has been shown to be of particular interest in the context of solidification processes. However, most of the existing studies either use a numerical approach or rely on model experiments in water, and the current literature is missing a direct experimental observation and characterization of acoustic streaming in a liquid metal. The experiment consists of velocity measurements of a jet generated by a 22 MHz transducer in a 50 x 50 x 200mm rectangular vessel, using Ultrasound Doppler Velocimetry (UDV). The ability of UDV to accurately measure peak jet velocities is examined through an analysis of the bias introduced by the finite size of the sampling volume. This analysis is supported by a direct comparison between UDV and Particle Image Velocimetry (PIV) measurements performed in a complementary water experiment using the same experimental configuration. The velocity measurements obtained in the liquid metal are then used to assess the validity of a dimensional-analysis-based model of acoustic streaming jets established using a time-scales separation method combined with linear acoustics.

Keywords: Acoustic streaming, Liquid metal flow, Ultrasound velocimetry

1. Introduction

Though acoustic streaming has been known for decades, the minimum set of dimensionless parameters required to characterize a jet driven by ultrasound through this phenomenon is not yet established in the international community. It is generally admitted that the time scales of the wave and of the mean flow differ so significantly (Statnikov [1], Moudjed et al. [2], Baudoin and Thomas [3]) that a one-way coupling occurs between the mean flow driven by acoustic streaming and the acoustic wave field, which remains unaffected by the mean flow. The coupling term is a body force originating from the acoustic field through a Reynolds-stress like mechanism. Vincent et al. [4]) recently proposed a minimal set of 6 dimensionless parameters to describe acoustic streaming jets in the limit of linear acoustic propagation. In their approach, the key parameters are the acoustic attenuation coefficient α and the ratio of the acoustic-power injected into the fluid medium, P_{ac}, to the sound celerity, c_S, which has been shown to bound the mean-flow momentum (Lighthill [5]). As the vast majority of experimental observations of acoustic streaming are usually performed in water and sometimes in air, assessing the validity of this approach from the existing literature is not straightforward.

The attenuation coefficient of acoustic waves in a Newtonian fluid is given by the following relation (Kinsler [6]):

$$\alpha = \frac{\omega^2 \nu}{2c_s^3}\left(\frac{4}{3} + \frac{\nu_B}{\nu} + \frac{\gamma - 1}{Pr}\right), \tag{1}$$

with $\omega, \nu, \nu_B,\ \gamma$ and Pr being respectively the angular frequency, kinematic viscosity, kinematic bulk viscosity, specific heat ratio and Prandtl number. As can be seen from this expression, the attenuation coefficient depends on the Prandtl number, which varies greatly between water and liquid metals. Beyond its interest for metallurgical applications, observing acoustic streaming in liquid metals has thus a fundamental interest.

A first objective of the observation should be to recover previously identified scaling laws that have been observed in water experiments and numerical models. One of these concerns the accelerating region of the jet, located between the transducer and the position of peak jet velocity. In this region, inertia is expected to balance the acoustic streaming force, which yields the following scaling for the velocity on the axis of the jet (Moudjed et al. [2], Vincent et al. [4]):

$$u(x) = \sqrt{Gr_{ac} x}\ , \tag{2}$$

where u is the non-dimensional velocity (scaled by the kinematic viscosity and transducer diameter), x is the longitudinal coordinate (scaled by the source diameter) and the acoustic Grashof number, $Gr_{ac} = 32\alpha P_{ac} D_s / \pi\rho c_s \nu^2$ is the intensity of the dimensionless forcing, proportional to the input acoustic power P_{ac}.

To our knowledge, such a direct quantification of acoustic streaming flow in a liquid metal is still lacking in the literature. In this study, we present ultrasound Doppler velocimetry (UDV) measurements of jets driven by an ultrasonic beam in the eutectic alloy GaInSn.

2. Experimental setup

The principle of the experiment is simple: an elongated parallelepipedal cavity is filled with GaInSn (the physical properties of which can be found in Plevachuk et al. [7]). An ultrasonic acoustic source is mounted flush in the middle of one of the end-walls and produces a continuous-wave ultrasound beam that drives the expected acoustic streaming jet. In practice, several difficulties arise: i) the kinematic viscosity is small, so observing significant acoustic streaming requires relatively high frequencies that are not so easy to produce in liquid metals, ii) this necessitates a technical solution that optimizes impedance matching of the sound source with the medium while avoiding corrosion issues, iii) standing waves due to reflection of the beam on the end-wall should ideally be avoided, iv) velocimetry in such a liquid metal is classically performed by UDV, but interference with the sound field that generates the flow could be detrimental. An additional issue is that the typical diameter of the jet has the same order of magnitude as the achievable size of UDV probing volume.

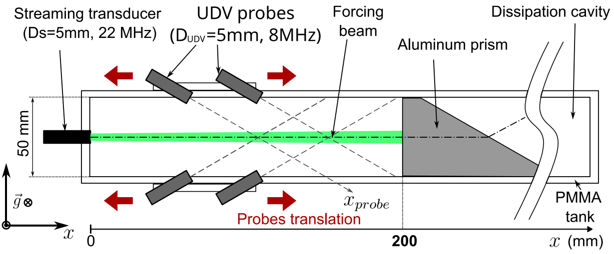

Figure 1: Sketch of the experimental setup, the acoustic beam forcing the flow is represented in green. The expected flow is a very elongated circular jet along x.

The set-up we designed is sketched in Figure 1. A PMMA tank of cross section 50 x 50 mm^2 is split into two areas. The observation area, in which the acoustic streaming jet is generated and measured, is 200 mm long. The forcing circular beam represented in green on the figure is generated by a circular 22MHz transducer of active surface diameter $D_s = 5$ mm. These characteristics have been chosen to be in good similarity with the water experiment described in Moudjed et al. [2]. The forcing beam axis is denoted the x-axis, while the z-axis is opposite to gravity. UDV measurements are performed from the side walls using two pairs of 8 MHz probes with active diameter $D_{UDV} = 5$ mm (TR0805LS, Signal Processing©, Switzerland). They are mounted on supports that can be moved along the x-direction between runs. Their axes are located in the x-y plane, forming a 45° angle with the x-axis, allowing the dominant velocity component in the x-direction to be recovered.

The boundary condition at the end of the observation area is ensured by an aluminum prism used to achieve both a no-slip vertical wall condition for the streaming flow and no reflection/pure transmission of the acoustic waves. Indeed, the acoustic impedance of aluminum closely matches that of GaInSn ($z_{GaInSn} = 17.37 \times 10^6$ Pa.s/m, $z_{Al} = 17.01 \times 10^6$ Pa.s/m). Because of the aggressive chemical reaction between aluminum and GaInSn, the aluminum prism was coated with a thin layer of nickel. The thickness of the coating layer, approximately 10 µm, was kept smaller than the ultrasound wavelength so as not to disrupt impedance matching. The second area of the vessel, represented on the right-hand side of the prism on the sketch, is also filled with GaInSn and constitutes a trap for acoustic waves that are dissipated after multiple reflections on the PMMA walls.

Particular attention has been paid to the design of the custom-made forcing transducer: we opted for a 22 MHz PZT piezoelectric transducer with a silica (SiO_2) matching layer. Silica acoustic impedance is indeed close to that of GaInSn ($z_{SiO2} = 13.1 \times 10^6$ Pa.s/m) and showed good wetting behaviour and chemical compatibility with GaInSn. The transducer was made at the *Institut d'Electronique et des Systèmes* (IES) in Montpellier, France.

To generate the acoustic streaming flow, the transducer is fed with a continuous 22 MHz sinusoidal signal. This signal is generated by a high-frequency generator, amplified, and monitored using a wattmeter. A feedback loop is used to keep the input electric power constant and stable at the required value in the range 0.1 W to 1 W. Below these values, the electronic chain is not able to accurately measure and maintain a stable input power, whereas higher powers risk overheating and damaging the piezoelectric element. Figure 2 shows a picture of the experimental setup mounted at the HZDR facilities.

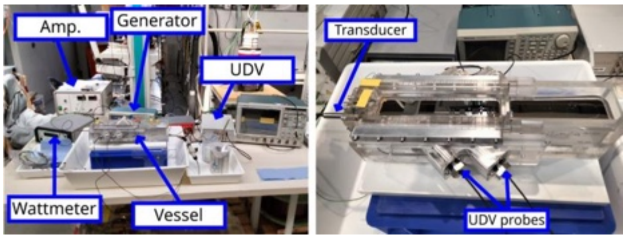

Figure 2: Picture of the experimental setup.

Measured velocities ranged from 1 to 10 mm/s, so that relatively low pulse repetition frequencies (PRF) were used in the UDV system, leading to acquisition frequencies of the order of 1 Hz. No seeding particles were introduced in the liquid since existing oxides were sufficient.

3. Ability of UDV to measure jet flows

Because of the relative size of the jet and of the UDV measurement volume, accurate velocity measurements may prove to be a challenge. Indeed, velocity gradients are expected to evolve sharply over a length scale comparable to the jet radius, which is roughly given by half the diameter of the transducer $D_{jet} \approx \mathrm{D_s}$ (Moudjed et al. [2]). As, in our particular experimental conditions, the diameters of the forcing transducer and the UDV probes are the same ($D_s = D_{UDV}$), we can expect strong bias in the velocity measurements due to averaging effects.

Biased UDV measurements due to the finite size of the sampling volume have been reported for flows with velocity gradients strongly varying in space (Kikura et al. [8], Ashour et al. [9]). The velocity measurements obtained with UDV can be seen as the average of the velocities of the particles inside a measurement volume delimited by the beam width and the length of the ultrasound burst. A first approximation of the measurement volume is a cylinder of length $n\lambda_{UDV}/2$ and diameter D_{UDV}, where n is the number of wavelengths in the ultrasound pulse and λ_{UDV} is the wavelength of the UDV probe.

In the case of a 1D parallel flow, Kikura et al. [8] have shown that the bias is proportional to the curvature of the velocity profile and the square of the projection of the measurement volume length on the direction of the velocity gradients. In our case, the error can thus be expected to be largest at the peak of the jet where the second derivative is maximal. The jet is however 3D, which makes estimating the bias more complicated.

Another situation where the bias can be estimated is when numerical simulations are compared to UDV experimental data. In this case, the simulated velocity field can be numerically integrated over the measurement volume to reproduce the bias introduced by UDV. A refined model of the UDV acoustic beam can be used for this purpose. Ashour et al. [9] used an analytical solution of the Rayleigh integral to weight the integration with the local acoustic intensity, leading to more accurate correction of the results. Such a correction however cannot be applied to experimental data alone.

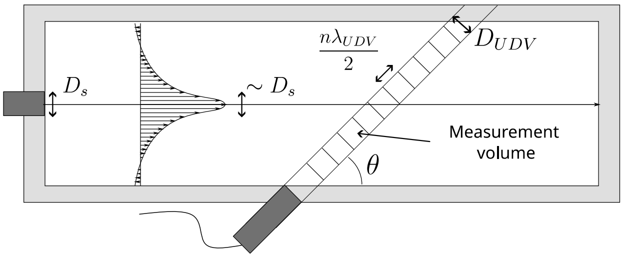

Figure 3: Schematic representation of the UDV measurement volume and acoustic streaming jet.

To investigate the measurement bias directly on acoustic streaming jets, we devised a modified experimental setup allowing simultaneous UDV and PIV measurements in water. The modified setup uses the same vessel as the liquid metal experiment described above, but the metal is replaced by water and the UDV probes on one side of the vessel are removed to provide optical access. A laser sheet is generated in the *x*-*y* plane and a camera is placed on top (see figure 4), allowing the acquisition of PIV velocity fields in the same plane as the UDV beams. The results are shown in figure 5. The typical thickness of the laser sheet was below 0.5 mm and typical interrogation areas of 4x4 mm^2 were used. Though not bias-free, PIV measurements are thus considered as the reference.

We performed velocity measurements with UDV number of pulse wavelength n from 4 to 32, leading to measurement volumes lengths compared to the characteristic jet size, $\frac{n\lambda_{UDV}}{2D_s}$, ranging from 0.15 to 1.18. We should note that the measurement volume has two dimensions $n\lambda_{UDV}/2$ and D_{UDV}, so that the projected length on the radial direction does not evolve linearly with the measurement volume length.

Figure 5 (a) shows the velocity profile of an acoustic streaming jet probed on the same 45° axis with PIV and UDV measurements. It shows that UDV underestimates the peak jet velocity, whereas it successfully measures velocities further away from the jet center, thus faithfully reproducing the shape and diameter of the jet. This behaviour is consistent with the study from Kikura et al. [8], although the dependence on the second derivative and projected volume length cannot be directly retrieved in this more complex geometry.

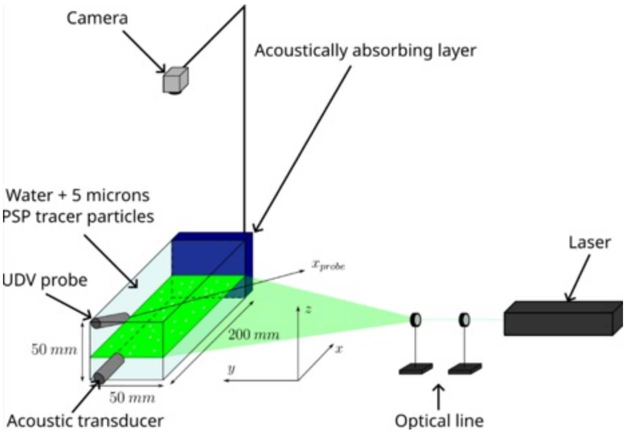

Figure 4: Schematic representation of the setup modified for the simultaneous measurement of velocities via PIV and UDV in water.

As expected, we observe a decrease in the measured peak velocity value with the number n of wavelengths in the pulse (figure 5 (b) and (c)). The liquid metal measurements were therefore performed using the smallest burst length, namely 4. In this particular setup, the UDV measured velocities ranged from 60% to 80% of the peak velocity. However, this value depends on the jet structure. As the jet width and curvature are expected to evolve along the *x*-axis, longitudinal profiles and scaling laws will be distorted by the bias, which cannot be undone using experimental data only.

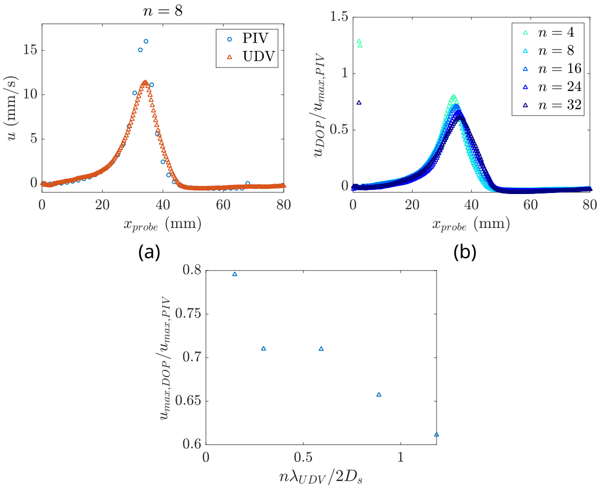

(a) (b)

(c)

Figure 5: Comparison of UDV and PIV measurements of acoustic streaming jets in water for different UDV probing volume length to forcing transducer diameter, $n\lambda_{UDV}/2D_s$. (a) Velocity profiles along the UDV probe axis in the case $n = 8$.

(b) UDV velocity profiles normalized by the corresponding maximum PIV velocity (c) Ratio of UDV over PIV velocity maxima.

4. Results

Figure 6 shows velocity measurements of the acoustic streaming jet along the UDV probe axis at two different positions inside the vessel ($x = 43$ mm and $x = 107$ mm, where x is taken at the intersection of the UDV probe axis and the streaming transducer axis). The first position lies within the expected accelerating inertial region of the jet (where (Eq. 2) scaling is expected), while the second is located downstream, where acoustic forcing is balanced by viscous effects (Vincent et al. [4]). The different profiles are for electrical power (forcing magnitude) ranging from 0.1 to 1 W.

We can clearly observe the acoustic streaming jet. The jet is centered, symmetric, and its amplitude and width evolve with the forcing amplitude and position on the x-axis. But although the streaming jet has been clearly measured over a few tens of seconds, the steady flow couldn't be observed for longer durations. The reason is the emergence of a thermal convection cell arising from heat generated by the piezoelectric element of the transducer, with the fluid rising from the acoustic source and recirculating on the opposite wall (not appearing in figure 6). Indeed, because the transducer has a limited efficiency, the electrical power P_e supplied to it is partitioned between acoustic radiation (P_{ac}) and heat generation (the value of which couldn't be measured but the efficiency is estimated to lie in the range from 0.5 to 0.8). The presence of the convection cell was confirmed experimentally using an additional UDV probe measuring profiles in the vertical plane through the free surface.

The convection flow velocity was found to be comparable in magnitude to the streaming jet velocity, leading to significant interaction between the two flows and consequently altering the jet structure. One way to mitigate this effect, without modifying the setup, is to rely on the different transient times of the acoustic streaming jet and of the convection cell. The characteristic timescale of the jet transient regime was found to be shorter than that of the convection flow, allowing measurements to be taken before convection was fully established. For each measurement, data acquisition began 10 seconds after activating the transducer in an initially quiescent fluid, allowing the streaming jet to develop. Fifty velocity profiles were then recorded and averaged to produce the results shown in Figure 6. This protocol helped to reduce the interference of the convection flow without however suppressing it.

Using this protocol, figure 6 (a) shows an excellent agreement between measurements and Eq. 2. The evolution of the on-axis velocity of the jet behaves as the square-root of the acoustic power, as expected with the scaling. It is the first confirmation of this scaling in liquid metal. Due to the convection flow however, the structure and scaling laws of the jet in the downstream region could not be recovered.

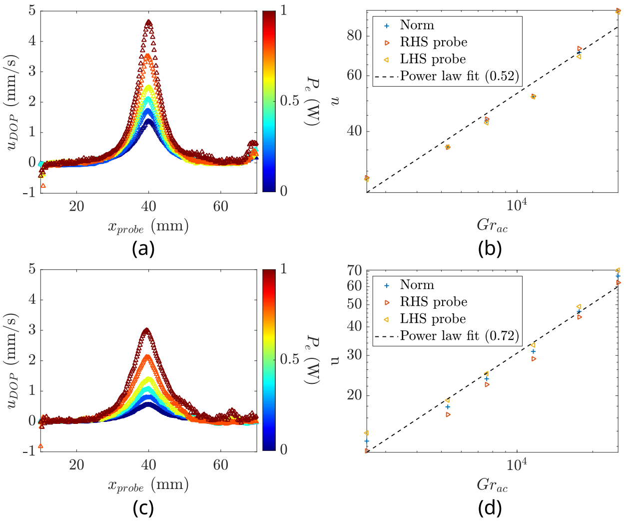

Figure 6: Liquid metal experimental results. (a) and (c): averaged UDV velocity profiles at respectively x=43mm and x=107mm, for electrical powers ranging from 0.1W to 1W, measured by the right-hand side probe. (b) and (d): scaling of the non-dimensional jet peak velocity with the acoustic Grashof number. The RHS (resp. LHS) data series corresponds to the peak velocity from the average velocity profiles measured by the right-hand side probe (resp. left-hand side). The norm is calculated from both values.

5. Summary

In this paper, we presented an experimental setup capable of observing acoustic streaming jets in liquid metal for the first time. The UDV measurements were found to be biased toward lower velocity values in regions of high jet curvature. Good agreement with theoretical predictions was obtained in certain regions; however, the presence of a thermally driven convection cell interacting with the jet prevented full recovery of its overall structure.

References

[1] Statnikov, Y. G. 1967 Flow currents generated by finite amplitude sound. Akust. Zh. 13, 146–148. 13, 14, 168.

[2] Moudjed, B, *et al.* "Scaling and dimensional analysis of acoustic streaming jets." *Physics of Fluids* 26.9 (2014).

[3] Baudoin, M, and J-L. T. "Acoustic tweezers for particle and fluid micromanipulation." *Annual Review of Fluid Mechanics* 52.1 (2020): 205-234.

[4] Vincent, B, *et al.* "Phenomenology of laminar acoustic streaming jets." *Physical Review Fluids* 10.11 (2025): 114103.

[5] Lighthill, J. "Acoustic streaming." *Journal of sound and vibration* 61.3 (1978): 391-418.

[6] Kinsler, L. E., *et al. Fundamentals of acoustics*. John wiley & sons, 2000.

[7] Plevachuk, Y, *et al.* "Thermophysical properties of the liquid Ga–In–Sn eutectic alloy." *Journal of Chemical & Engineering Data* 59.3 (2014): 757-763.

[8] Kikura, H, Gentaro Y, and Masanori A. "Effect of measurement volume size on turbulent flow measurement using ultrasonic Doppler method." *Experiments in Fluids* 36.1 (2004): 187-196

[9] Ashour, R. F., *et al.* "Competing forces in liquid metal electrodes and batteries." *Journal of Power Sources* 378 (2018): 301-310.

Flow Profile Reconstruction of Hydrothermal Fluid Using Experimental Buoyant Jet Model

Tomonori Ihara, Satomi Ueno

Department of Marine Electronics and Mechanical Engineering, Tokyo University of Marine Science and Technology, 2-1-6 Etchujima, Koto, Tokyo 135-8533, Japan.

Measuring fluid flow at hydrothermal vents is challenging due to its extreme conditions that prohibit the use of conventional flowmeters. To overcome these harsh conditions, a novel measurement approach utilizing UVP combined with an experimental buoyant jet model was developed. Regression analysis of an axisymmetric buoyant jet model is employed to reconstruct the full flow profile and accurately estimate total flowrates. The proposed model-based reconstruction technique was first validated through laboratory experiments. Using an ethanol jet in a water tank to simulate buoyancy effects, the model showed good agreement with reference flowmeters and successfully captured buoyancy effects. Subsequently, the method was deployed for field experiments at deep-sea. The flowrate estimations from the field data correlated well with visual velocity observations.

Keywords: Hydrothermal fluid, Flow rate, Fluid modeling

1. Introduction

Hydrothermal vent fluids exhibit interesting characteristics where the transportation of heat, fluid and material takes place involving the precipitation of minerals due to a sudden temperature drop. Clarifying this complicated process is challenging since vent typically occurs at depth greater than 1,000 m. High pressure and high temperature conditions prohibit the application of conventional flow measurement techniques. We have been developing the UVP based measurement technique for such conditions and successfully acquired field data [1, 2]. The UVP is basically one-dimensional one-component measurement, and thus, some modelling approach is required to reconstruct flow profile. We employed an experimental buoyant jet model [3] to reconstruct the velocity profile regressively. This paper demonstrates flowrate estimation with the developed model-based flow reconstruction approach for both laboratory experiment and field experiments.

2. Hydrothermal vent fluid flow

2.1 Flow characteristics

The hydrothermal vent fluid originates from seawater, which penetrates down to the crust and is then heated up by a heat source (magma or hot rocks) [4]. Water-rock reaction takes place under the seabed, and the fluid exits to the seafloor where the ambient temperature is 2 to 4°C. Due to the rapid change of conditions for the fluid, chemical deposition occurs and forms a unique vent structure. A “black smoker” chimney is the most iconic structure as shown in Figures 1 (a). The fluid temperature from “black smokers” typically exceeds 300°C and it contains sulfide deposits, which make the fluid “black”. As hot fluid discharges, the chimney grows together with replacement of composition, and some of them reportedly even grow a few tens of centimeters a day. Vent orifice shape also alters in time as the chimney structure itself changes as well as its flow path inside. Active chimneys discharge high flowrate fluids, and flow characteristics around the orifice are momentum dominated regime and then transition to a buoyant dominated regime. Depending on the chimney structure or interior state, some of them become the “diffuser” type (Figures 1 (b)); the chimney itself does not have obvious flow path but the fluid percolates slowly. Temperature of the chimney surface is rather low (typically less than 100° C) and flow regime is buoyant dominant. Another type is the “flange” (Figures 1 (c)); the flow discharges under the flange-like chimney structure and it develops in time. As the flow discharges to the sea like spilling from the flange, the flow regime is rather buoyant dominant. In addition to those types, we can also observe diffusing hot water from crusts [5] as shown in Figure 1 (d). Fluid is slowly diffusing from the cracks in the crust, and the flow regime is buoyant dominant. Outside of those classifications for natural vents, there is also artificial hydrothermal vents (Figures 1 (e)), which is made by drilling, and some of them have very active discharge and rapid growth of chimneys [6]. As a whole, hydrothermal vent fluid flow regime is normally buoyant dominant but momentum dominant just around the orifice when the flowrate is high.

2.2 Flow modelling

Given the discussion above, the velocity profile is modelled by axisymmetric equations using experimental buoyant jet model. Axial velocity can be expressed:

$$u = A_{\mathrm{u}}\left(\frac{u_0}{(z - z_0)^{\mathrm{n}}}\right)(1 + B\eta^2)\exp(-\eta^2) \qquad (1)$$

See reference [3] for the details of the parameters as well as radial velocity equation. As explained before, we can only obtain one dimensional one component profile from the vent due to the practical difficulties for deploying multiple ultrasonic transducers. Therefore, we applied this flow model to the measurements by regression analysis to obtain equation parameters. Then, the flowrate can be estimated by integrating the model equation:

$$Q = A_{\mathrm{u}}\left(\frac{u_0}{(z - z_0)^{\mathrm{n}}}\right)(\pi\,(B + 1)c^2(z - z_0)^2) \qquad (2)$$

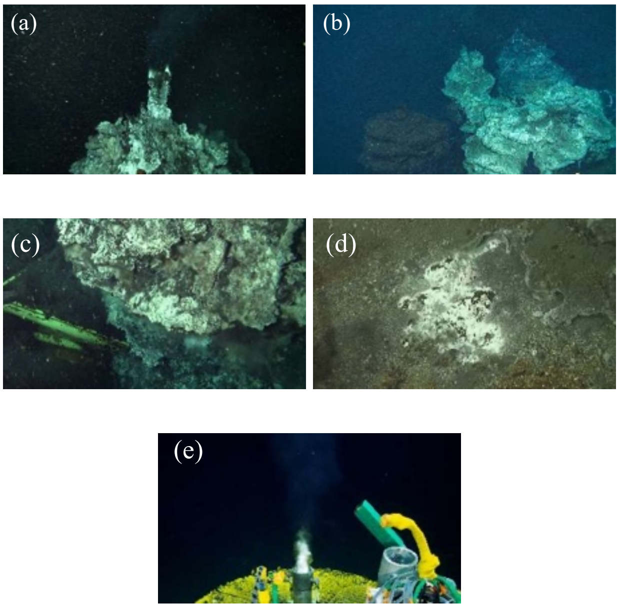

Figures 1: Types of hydrothermal vents. (a) black smoker type at mid-Okinawa trough, (b) diffuser type at Myojin-sho caldera, (c) flange type at mid-Okinawa trough, (d) diffusing type at Myojin-sho caldera, (e) artificial vent at mid-Okinawa trough. Copyrights of all pictures belong to JAMSTEC.

3. Experimental results and discussion

3.1 Laboratory experiment

A laboratory experiment was conducted to validate the developed approach. The flowrate of the jet increases after the orifice due to the entrainment. Note that axial kinematic momentum decreases along the jet since radial kinematic momentum increases as the jet develops. An ethanol jet into a water tank was measured in the experiment to simulate the buoyancy effect [2]. The orifice diameter was 8 mm and ultrasonic beam height at the jet center was 10.5 mm. Water was pumped to the nozzle at the fixed flowrate (0.5 L/min.) until the jet developed, and switched to ethanol so that we can measure both a momentum jet and a momentum-buoyancy jet.

3.2 Field experiment

We have performed several research cruises for the field experiments for submarine hydrothermal vents at Izu-Bonin arc (island arc) and at mid-Okinawa trough (back-arc basin). Selected results for Sunrise deposit at Myojin knoll, Izu-Bonin arc are discussed in this extended abstract. The measurement of vent flow was performed with Peacock UVP (Ubertone) and specially designed measurement setup [1]. A picture taken during the measurement is shown in Figure 2.

3.3 Results and discussion

The estimated flowrates, initial velocities u_0 and determination factors R^2 are shown in Table 1. Compared with the initial flowrate for the laboratory experiment (0.5 L/min.), an increase in the flowrate can be confirmed as discussed before, especially under buoyant conditions (ethanol). This agrees with the fact that buoyancy plays one of the key roles and enhances "entrainment". Results for the field experiment at Sunrise deposit does not have a reference flowmeter nor known discharge flow velocity. Yet, comparing with the flow velocity observed by video footage with a remotely operated vehicle during the measurement, estimated initial velocity shows fair agreement. Flowrate for the mildly active hydrothermal vents are also reported as a few tens of L/min, which also shows fair agreement.

Figure 2: Photo during the field measurement. Ultrasonic transducers with heat protectors (marked with yellow tapes) were oriented toward the vent fluid (can be seen as Schlieren).

Table 1: Estimated flowrate and selected parameters.

Condition	Flowrate Q [L/min.]	Initial velocity u_0 [mm/s]	R^2
Lab. normal	0.563	166	0.927
Lab. buoyant	0.696	166	0.906
Sunrise deposit	13.5	41.6	0.934

4. Summary

Flow profile reconstruction using an experimental buoyant jet model was demonstrated. Flowrate was calculated by integrating the profile and it showed a good agreement in the laboratory experiment with the reference flowmeter. Further results and discussion are presented in the symposium. This study was supported by Cooperative Research Program of Atmosphere and Ocean Research Institute, The University of Tokyo (R/V Shinsei Maru, JURCAOSS22-16, 23-6, 24-24 and 25-39) as well as JSPS KAKENHI Grant Numbers JP18K13937, JP21K14360 and JP26K07891.

References

[1] Ueno S, *et al.*: Investigation of the influence of the background ocean current on flow measurements using the UVP method, ISUD14 (2023), 1-4.

[2] Ihara T, *et al.*: Effects of inhomogeneous fluid field on UVP measurement, ISUD13 (2021), 1-4.

[3] El-Amin MF, *et al.*: Analysis of a turbulent buoyant confined jet modeled using realizable k–ε model, Heat Mass Trans. 46 (2010), 943-960.

[4] Tivey MK: Generation of seafloor hydrothermal vent fluids and associated mineral deposits, Oceanogr. 20 (2007), 50-65.

[5] Wheeler B, *et al.*: Diffuse venting and near seafloor hydrothermal circulation at the Lucky Strike vent field, Mid-Atlantic Ridge, Geochem. Geophys. Geosyst. 25 (2024), e2023GC011099.

[6] Nozaki T, *et al.*: Rapid growth of mineral deposits at artificial seafloor hydrothermal vents. Sci. Rep. 6 (2016), 22163.

15th International Symposium on Ultrasonic Doppler Methods for Fluid Mechanics and Fluid Engineering
LEGI, Univ. Grenoble Alpes, France (3.-7. May 2026)

Evaluation of Flow Regime and Wetness Fraction in Two-Phase Flows using a Clamp-on Ultrasonic Technique

Hideki Murakawa[1], Yuya Kojima[1], Kodai Kondo[1], Katsumi Sugimoto[1]
[1] Dept. of Mechanical Engineering, Kobe Univ., 1-1 Rokkodai, Nada, Kobe, Japan.

In various energy-related fields, it is necessary to evaluate the flow conditions within metal pipes. The clamp-on ultrasonic technique transmits and receives ultrasonic signals between a pair of sensors installed outside the piping; thus, it is effective for evaluating flow conditions in existing pipes. In this study, the clamp-on ultrasonic technique was applied to evaluate the flow regimes in wet steam flows in a horizontal pipe and in bubbly and slug flows in a vertical pipe. The temporal changes in the received ultrasonic waveform are caused by changes in the path of the ultrasonic waves owing to changes in the gas–liquid interface. To evaluate the temporal change in the waveforms, standard deviation distributions were calculated. Based on the distribution, it was demonstrated that flow regime identification was possible for wet steam flows and for bubbly and slug flows. Furthermore, it was demonstrated that the wetness fraction in the wet steam flow can be evaluated using the gas flow rate and flow regime conditions. Thus, the clamp-on ultrasonic technique is effective for evaluating flow conditions inside existing metal pipes.

Keywords: Clamp-on ultrasonic technique, Flow regime, Two-phase flow, Wetness fraction

1. Introduction

Two-phase flows occur in many industrial pipes. For instance, wavy or annular mist flows may appear owing to heat loss in supplying steam pipes. Understanding the wetness fraction in wet steam flows is crucial for optimizing energy savings. In liquid CO2 (LCO2) pipelines, gaseous and solid phases (dry ice) may be generated by pressure loss. Phase changes lead to changes in the fluid volume, which can cause problems with LCO2 transport. During methane hydrate extraction, gas–liquid two-phase or solid–gas–liquid three-phase flows occur. In these cases, understanding the flow regimes is crucial for ensuring equipment safety and efficiency and minimizing energy waste. These pipes are typically made of opaque steel and therefore cannot be visualized. Generally, the flow conditions can be evaluated by installing equipment such as pressure gauges and flow meters in the pipes in advance. However, it may sometimes be necessary to evaluate the flow conditions within existing piping in locations where measurement equipment is not installed beforehand.

Clamp-on ultrasonic technique is an effective method for this purpose. This is typically used in ultrasonic flowmeters. An ultrasonic flow meter transmits and receives ultrasonic waves between a pair of sensors installed on the outside of a pipe and determines the flow rate in the pipe based on the difference in the propagation time of the ultrasonic waves from upstream to downstream and from downstream to upstream. The authors applied this method to measure wet steam flows [1-3]. The authors found that the received waveforms of clamp-on ultrasonic flowmeters changed over time, depending on the flow patterns in a horizontal pipe [2]. It is known that the flow pattern changes depending on the gas and liquid flow rates, that is, the flow rate of the gas phase and the wetness fraction. Wavy and annular mist flows are expected to occur for wet steam flow in horizontal pipes. The wetness fraction can be evaluated based on the gas-phase flow rate and flow pattern in wet steam flows in pipes.

In this study, we aimed to predict the flow regimes in wet steam flow in a horizontal pipe and bubbly and slug flows in a vertical pipe using the clamp-on ultrasonic technique. A method for evaluating flow patterns based on ultrasonic waveforms obtained under various pressures, wetness fractions, and flow rate conditions is proposed herein. The wetness fraction in the steam flow is evaluated based on the steam flow rate and flow conditions. Furthermore, this method is applied to two-phase flows in a vertical pipe. The target flow conditions are bubbly and slug flows which are the continuous phase of liquid. The possibility of evaluating the flow regime based on changes in the received waveforms is discussed.

2. Wet steam flows in a horizontal pipe

2.1 Experimental conditions and method

In this study, the flow pattern in wet steam flow was evaluated using ultrasonic waveforms obtained in wet steam flow experiments conducted by the authors [3]. For details of the experiment, please refer to the cited study. A brief explanation of the experiment is provided below. The experimental setup consisted of an SGP65A carbon steel pipe (outer diameter: 76.3 mm, inner diameter: 67.9 mm) as the test section, with ultrasonic sensors mounted horizontally on the outer surface of the pipe at the upstream and downstream positions, facing each other. Ultrasonic transmission and reception were performed using a laboratory-made measurement system consisting of a pulser/receiver, digitizer, and PC. The sensor frequency was 1 MHz, and burst signals were pulsed at 1 MHz. The experimental conditions are listed in Table 1. The experiments were conducted under conditions of absolute pressure P = 0.2–0.8 MPa, reference area-average gas velocity V_{ref} of 10–30 m/s, and steam wetness fraction $\beta = 2.0$–21%. For each condition, 5,000 ultrasonic received waveforms were used for evaluation.

Table 1: Experimental conditions for wet steam flows

Pressure, P [MPa]	Reference area-average velocity, V_{ref} [m/s]	Wetness fraction, β [%]
0.21	27.3–39.4	3.60–21.47
0.33	20.0–31.6	3.44–17.47
0.50	20.1–30.2	3.13–19.31
0.70	10.5–30.1	2.00–18.49
0.80	10.2–20.5	3.91–7.43

2.2 Received waveforms

Figure 1 shows examples of the ensemble average and their standard deviations (SDs) calculated from 1,000 instantaneous waveforms in the wet steam flow at $P = 0.50$ MPa. The transmitted ultrasonic signals are shown to move from upstream to downstream. Based on the empirical models of Weisman et al. [4] for the stratified-annular transition boundary in horizontal two-phase flow, Figures 1(a) and (b) show the conditions for wavy and annular mist flows, respectively. The horizontal axis represents the time elapsed t from pulse emission. High-intensity signals are confirmed at $t < 5$ µs, which are noise associated with the pulse emission as the transmitter and receiver transducers were connected to the same pulser/receiver. Therefore, these signals are neglected. High-intensity signals appear at $t > 50$ µs. The speed of sound in carbon steel is considerably higher than that in steam. Thus, ultrasonic waves propagated in the pipe wall, which are referred to as guided waves, appeared earlier than those propagated in the steam. Figure 2 shows a schematic of ultrasonic transmission in the pipe cross-section. To measure the steam flow rate, the guided wave was more significant than the ultrasonic waves that transmitted into the steam owing to the large difference in the acoustic impedance between the steam and the pipe. Because there are many propagation paths inside the pipe wall, the guided waves were confirmed over a wide range of elapsed times. The target ultrasonic signals propagating through the wet steam flow were confirmed at approximately 175 µs.

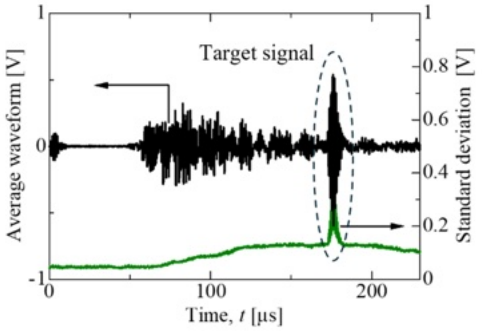

(a) Wavy flow ($V_{\mathrm{ref}} = 20.5$ m/s, $\beta = 9.2\%$).

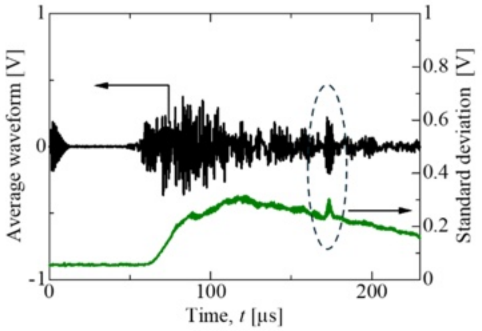

(b) Annular mis flow ($V_{\mathrm{ref}} = 30.2$ m/s, $\beta = 9.2\%$).

Figure 1: Average waveforms and their standard deviations for wet steam flows at $P = 0.50$ MPa.

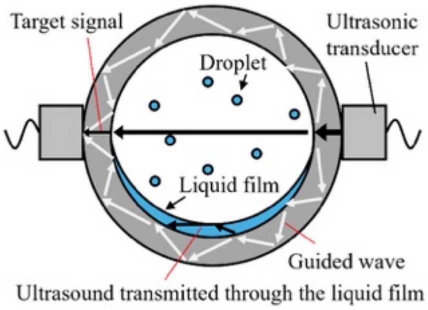

Figure 2: Schematic of ultrasonic transmission in a pipe cross-section for wet steam flow.

2.3 Flow pattern recognition using machine learning

The guided waves change as they propagate inside the liquid film with time, resulting in variations in the SDs. To distinguish the flow patterns from the SDs, machine learning using a support vector machine (SVM) is introduced. Wavy and annular mist flows at $P = 0.50$ MPa, as shown in Figure 1, were used as training data. A total of 5,000 waveforms were acquired for each condition. One SD distribution was calculated from 50 waveforms, resulting in 100 SD distributions for each condition. These 100 data were used to train the waveforms for each flow pattern.

Similarly, the SD distributions were calculated for the other conditions, and the flow patterns were identified using the learned model. Wavy flow was scored as 0 and annular mist flow was scored as 1. The average value of the flow pattern identification results for 50 data in each condition was obtained. Figure 3 shows the flow pattern recognition scores as color plots on a flow pattern map at $P = 0.50$ MPa. The horizontal and vertical axes indicate the superficial gas and liquid velocities, respectively. The teaching data are shown in the figure. As shown in the results, the recognition score changes as the flow pattern changes. Under the transition conditions, which are approximately the transition boundary proposed by Weisman et al. [4], intermediate scores between wavy and annular mist flows are obtained, demonstrating that the use of the SD distribution makes it possible to accurately distinguish the flow patterns.

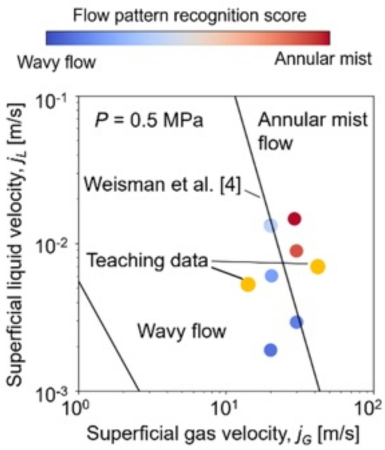

Figure 3: Flow pattern recognition score plotted on the flow pattern map at P = 0.50 MPa.

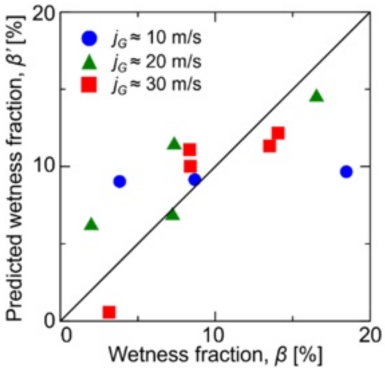

Figure 4: Prediction of the wetness fraction by multiple regression analysis using the gas-phase flow rate and the obtained flow pattern recognition score as parameters.

2.4 Wetness fraction prediction

As can be seen from the flow pattern map in Figure 3, it can be said that the flow pattern roughly changes from the wavy to annular mist flow at a constant superficial gas velocity, j_G, with increases of superficial liquid velocity, j_L. j_G can be determined based on the basic principle of a time-of-flight ultrasonic flowmeter. Thus, if the flow pattern can be evaluated based on the ultrasonic waveforms under these conditions, j_L or the wetness fraction β can be evaluated. Note that the measured flow rate is not identical to the flow rate of the gas phase owing to the presence of the liquid. The uncertainty in the flow rate increases with the wetness fraction. Therefore, the effect of the liquid volume fraction on the flow rate is negligible.

To verify the above assumption, a multiple regression analysis was performed to evaluate the measured wetness fractions β' and β using the gas-phase flow rate and the obtained flow pattern recognition score as parameters. Figure 4 shows the results of the wetness fraction prediction. The horizontal axis represents β, which was set during the experiment, and the vertical axis represents the predicted wetness fraction. For $j_G \approx 20$ and 30 m/s, it can be confirmed that β' increases with β, resulting in the wetness fraction being approximately predicted. However, for $j_G \approx 10$ m/s, the dependence of β' on β could not be confirmed. For a lower j_G, the flow pattern is wavy, even with a higher j_L. Thus, the change in the flow pattern recognition score owing to differences in j_L is small. Consequently, the prediction of the wetness fraction was difficult at $j_G \approx 10$ m/s.

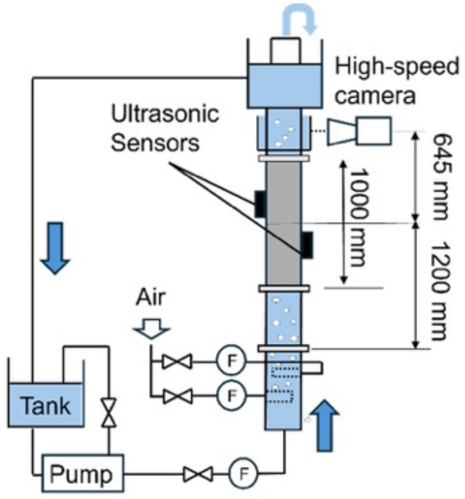

Figure 5: Schematic of experimental apparatus for two-phase flows in a vertical pipe.

In this study, only one condition, namely, wavy and annular mist flows, was used as training data for the flow pattern. With an increase in the condition of the training data, the results of predicting the wetness fraction in wavy flow should improve.

3. Bubbly and slug flows in a vertical pipe

3.1 Experimental conditions and method

Figure 5 shows the experimental setup for two-phase flow experiments in a vertical pipe. Water was circulated from the bottom to the upper tanks, and air was injected through porous materials. A diffuser plate with multiple holes with a diameter of 4 mm was installed downstream of the bubble injection section. The test section was SUS 50A Sch10S pipe (outer diameter: 60.5 mm, inner diameter: 54.9 mm) with 1 m in length. Ultrasonic transducers were set on the outer surface of the test section. The incident angle of the transducer was 45°, which was determined through preliminary experiments using variable-incident-angle transducers. The other measurement system was similar to that for the experiment with wet steam flows.

Two-phase flow experiments were conducted in the ranges of j_L = 0.012–0.43 m/s and j_G = 0.05–0.72 m/s. Flow visualization using a high-speed camera was performed in the observation section installed downstream of the test section. It was confirmed that the flow regime was from bubble to slug flows in this condition.

3.2 Received waveforms

Figure 6 shows examples of the ensemble average and their standard deviations calculated from 10,000 instantaneous waveforms in bubbly and slug flows. The propagation time of the target signal, which traveled directly through the liquid, is shown by the red dotted line

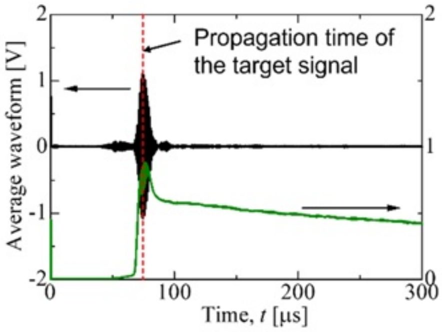

(a) Bubbly flow (j_L = 0.1 m/s, j_G = 0.05 m/s)

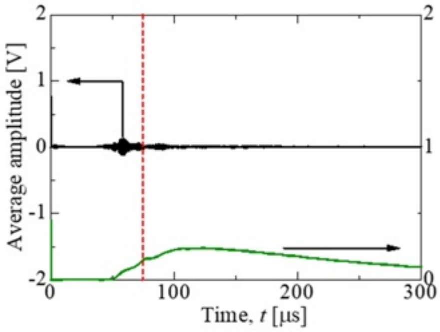

(b) Slug flow (j_L = 0.1 m/s, j_G = 0.7 m/s)

Figure 6: Average waveforms and their standard deviations for two-phase flows.

for reference.

In bubbly flow conditions, although bubbles sometimes obstruct ultrasonic wave propagation through liquids, many signals still propagate through the liquid and are received by sensors on the other side. Therefore, a high-intensity waveform is confirmed as the target signal. The signals confirmed before the target signal are guided waves, which mainly propagate within the pipe wall, and the intensity is weaker than that of wet steam flows. This is because the transmission intensity of ultrasound is higher from metal to water than from metal to steam, resulting in a reduction in the intensity of the guided waves in the pipe wall. It can be observed that a large fluctuation in the amplitude occurs after the propagation time. This is because multiple reflections of ultrasound occur between numerous bubbles, increasing the propagation distance and time of the ultrasound, as shown in Figure 7.

In slug flow, much of the ultrasound propagation is obstructed by slug bubbles. Consequently, the probability of the sensor on the opposite side receiving ultrasound that penetrates the liquid is drastically reduced. Therefore, a clear signal could not be detected when the target signal was expected to arrive. However, it can be seen that the time variation of the guided wave in the time prior to the arrival of the target signal is clearly larger than that in bubbly flow. This is because the ultrasonic waves transmitted from the pipe wall to the liquid phase were reflected at the interface of the slug bubbles, and these reflected waves then propagated again through the pipe as guided waves, causing a time-dependent change in the waveforms.

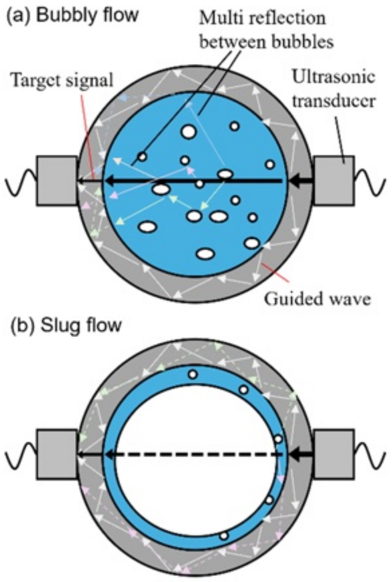

Figure 7: Schematic of the ultrasound propagation paths in bubbly and slug flows in vertical pipes.

These results indicate that the evaluation of the flow regimes of bubbly and slug flows in a vertical pipe is possible based on the time variation of the target signal and the guided wave, that is, the standard deviation distribution.

4. Summary

In this study, a clamp-on ultrasonic technique was applied to evaluate flow regimes in wet steam flows in a horizontal pipe and in bubbly and slug flows in a vertical pipe. The temporal changes in the received ultrasonic waveform are caused by changes in the path of the ultrasonic waves owing to changes in the gas–liquid interface. Based on the standard deviations of the waveforms, it was demonstrated that flow regime identification was possible. Furthermore, this technique can be used to predict the wetness fraction in wet steam flows. Thus, the clamp-on ultrasonic technique is effective for evaluating flow conditions inside existing metal pipes.

References

[1] Murakawa H, Ichimura S, Shimada M, Sugimoto K, Asano H, Umezawa S & Sugita K: Effect of incident angle on ultrasonic transmission in steam flow for use with clamp-on ultrasonic flowmeter, Mech. Eng. J. 7 (2020) 20-00131.

[2] Murakawa H, Ichimura S, Sugimoto K, Asano H, Umezawa S & Sugita K: Evaluation method of transit time difference for clamp-on ultrasonic flowmeters in two-phase flows, Exp. Therm. Fluid Sci. 112 (2020) 109957.

[3] Murakawa H, Ichimura S, Sugimoto K, Asano H, Umezawa S, Taira H, Ibi M & Akahane H: Measurement of steam flow rates using a clamp-on ultrasonic flowmeter with various wetness fractions, Flow Meas. and Instr. 80 (2021) 101997.

[4] Weisman J, Duncan D, Gibson J & Crawford T, Effects of fluid properties and pipe diameter on two-phase flow patterns in horizontal lines, Int. J. Multiphase Flow 5 (1979) 437–462.

Measurement of Bubble Rising Behavior using an Ultrasonic Phased Array Technique

Kota Uemura[1], Tasuki Nakane[1], Katsumi Sugimoto[1], Hideki Murakawa[1]

[1] Dept. of Mechanical Engineering, Kobe Univ., 1-1 Rokkodai, Nada, Kobe, Japan.

To improve the quality of steel products, it is important to understand the behavior of bubbles rising in a liquid metal under a horizontal magnetic field (MF). In this study, experiments were conducted in an air–water system to verify whether the rising trajectory of a bubble can be measured using an ultrasonic phased array (UPA) method. In the UPA measurement, strong reflected signals from the gas–liquid interface were successfully detected, enabling the reconstruction of the three-dimensional rising trajectory of a single bubble. These results demonstrate that the proposed method is effective as a measurement system for evaluating the three-dimensional rising behavior of bubbles. Furthermore, simultaneous measurements were performed using the UPA and ultrasonic tomography (UT). Although the measurement results were degraded by interference between the ultrasonic emissions in each method, it was shown that the evaluation of bubble trajectories and bubble shapes could be possible with simultaneous measurements using the UPA and UT.

Keywords: Bubble trajectory, Ultrasonic phased array, Ultrasonic tomography

1. Introduction

Understanding the behavior of bubbles under the influence of a magnetic field (MF) is a major concern in steelmaking processes. When bubbles rise in a liquid metal under a horizontal MF, it is known that bubble oscillations are suppressed owing to the Lorentz force caused by the induced current, and the bubbles tend to ascend linearly [1]. If the MF strength weakens, the bubble oscillation motion has anisotropy depending on the MF direction. One of the key factors affecting the rising behavior of bubbles is the bubble shape. For air bubbles rising in water, it has been reported that the bubble ascends with a zigzag trajectory for spherical bubbles, whereas it exhibits a spiral trajectory for ellipsoidal bubbles [2]. In addition, a horizontal MF is known to influence the bubble shape, and it has been reported that the bubble becomes more flattened when a horizontal MF is applied [3]. Based on these considerations, it is essential to simultaneously evaluate the bubble shape and the three-dimensional rising trajectory of bubbles to clarify the rising behavior of bubbles in liquid metals under a horizontal MF. However, the behavior of bubbles in liquid metals has not been fully clarified because of the difficulty of the experiment owing to the opacity of the fluids.

In our laboratory, the ultrasonic tomography (UT) method was developed and used to measure bubbles rising in liquid metals [4]. This method can evaluate the bubble shape and passing position at a measurement cross-section and allows the estimation of the bubble shape and bubble movement [5]. However, this technique is limited to obtaining information at the measurement cross-sections. Thus, it is difficult to clarify the trajectory of the bubble.

Gou et al. [6] demonstrated the measurement of bubble rising trajectories in a gallium alloy using an ultrasonic phased array (UPA) method. However, this method could not obtain the bubble shape. Therefore, simultaneous measurement with the UPA and UT is effective for clarifying the behavior and shape of bubble rising. Applying this approach, there are concerns about the effects of ultrasonic interference caused by each measurement method. In this study, we aimed to investigate the optimal signal processing method for measuring bubble behavior using the UPA and attempted simultaneous measurement with the UT.

2. Experimental setup

2.1 System configurations

Figure 1 shows a schematic of the experimental apparatus used in this study. The test section comprised a cylindrical container with an inner diameter of 50 mm filled with water up to a height of 215 mm. A single bubble was generated from a nozzle (d_e = 0.7 mm) installed at the bottom of the container. The nozzle was connected to a syringe to inject air and generate bubbles. A measurement cross-section using the UT sensors was installed at a height of 175 mm. The UPA sensor was placed in contact with water at the top of the container.

2.2 Ultrasonic phased array method

The UPA transducer comprised 10 × 10 ultrasonic elements with an area of 2.5×2.5 mm^2 as shown in Figure 2. The pitch size was 3.0 mm. The resonant frequency of the element was 4 MHz. The transducer was connected to a UPA device (Explorer, TPAC) for ultrasonic pulse transmission and reception. Ultrasonic pulses were transmitted and received by sequentially switching each

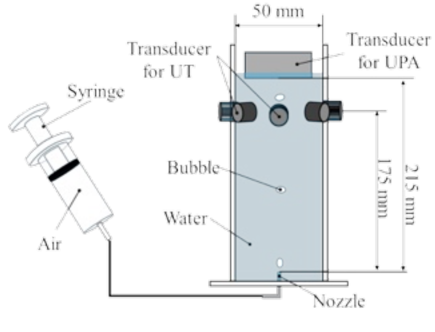

Figure 1: Schematic of the experimental apparatus.

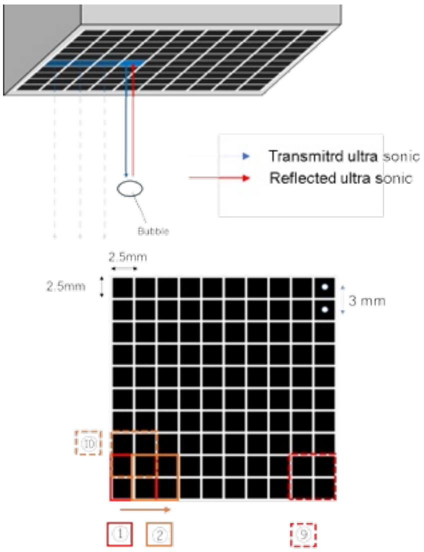

Figure 2: Schematic of the UPA sensor and its element configuration.

element or element group. By repeating this transmission–reception cycle, the reflected signals on the gas–liquid interface were obtained.

Ultrasonic pulses can be transmitted and received by a single element or by combining several elements. Considering the resonant frequency and element size, a 2 × 2 element group for transmitting and receiving ultrasound signals was selected. After transmitting an ultrasonic pulse from one element group, the reflected signal was recorded for 240 µs. This implies that the behavior of bubbles can be determined within a range of 180 mm from the transducer based on the speed of sound in water. The waveforms received by each element are combined into a single waveform and recorded on a PC. After a 70 µs of the waiting time, the element group is switched and ultrasonic pulse transmission and reception are performed with the next element group. Thus, the transmission interval between element groups is 310 µs. The element groups are scanned with overlapping elements, as shown in Figure 2, where two elements overlap during scanning. The scanning was performed in the horizontal x- and y-directions. By moving the element groups in this manner and sequentially transmitting and receiving ultrasound signals, one scan is completed through the transmission and reception of a total of 81 element groups. Therefore, it takes 310 µs × 81 = 25.11 ms for one scan, resulting in approximately 40 Hz.

To measure the position of the bubbles, the positions of the ultrasonic reflections were considered to be the centers of each element group. However, in this case, the spatial resolution will be 3 mm, which is the distance of the element pitch. Therefore, Gaussian interpolation was applied based on the signal intensities obtained by each element group in the UPA method to fill in the gaps between pitches.

2.3 Ultrasonic tomography method

In our group, an ultrasonic tomography (UT) method was developed and has been employed to measure the rising behavior of bubbles in liquid metals [4, 5]. The UT method consists of multiple wide-angle ultrasonic transducers (TDXs) installed in the measurement cross-section. The resonant frequency is 5 MHz. Each transducer sequentially transmits ultrasonic pulses with a single cycle, and the reflected and transmitted signals are received by all the other transducers. By superimposing the reflected signal intensities obtained along multiple propagation paths, the cross-sectional void distribution is reconstructed. At the gas–liquid interface, a large acoustic impedance difference exists between the gas and liquid phases, resulting in strong reflected signals. Therefore, regions with high reflected signal intensity correspond to the bubble interface. Using UT, the cross-sectional shape of the bubble can be visualized from the intensity distribution. To evaluate the impact of UT on the UPA measurements, a UT measurement cross-section was placed 175 mm from the bottom surface, and simultaneous measurements of the UPA and UT were performed.

3. Results and discussion

3.1 Received waveforms and signal processing

UPA measurements were performed for a single air bubble rising in water. Ultrasonic pulses were emitted from each element group into the water, and the reflected signals were received by the same element group. This transmission and reception was performed sequentially for all element groups, and the bubble position was determined after completing the scanning of all element groups. The ultrasonic signals received by each element group include reflections from the bubble. Owing to the large acoustic impedance difference at the gas–liquid interface, the received waveforms exhibit large amplitudes when reflections from the bubble are recorded. Figure 3(a) shows an example of a received waveform obtained by the UPA for one element group. As shown in the figure, the reflected signal, which appeared at approximately 210 µs, exhibits a sufficiently strong peak, indicating that signals including reflections from the bubble can be clearly distinguished.

As shown in Figure 3(a), the reflected waveform exhibits both positive and negative amplitudes. Therefore, the received waveforms were divided into time windows, and the peak-to-peak voltage (V_{pp}) in each time window was calculated to evaluate the signal intensities. As the ultrasonic resonant frequency is 4 MHz, the time window was set to 0.5 µs, which is the traveling time for one wavelength. In water, the time window corresponds to an axial distance of 0.375 mm, considering the round-trip distance. Figure 3(b) shows the temporal variation of V_{pp} calculated from the received waveforms, including reflections from the bubble. The reflected signals from the bubble exhibit clear peaks, indicating that V_{pp} is suitable for evaluating the bubble position. The bubble positions in the axial distance were determined based on the time at which a strong V_{pp} was observed, whereas those in the horizontal coordinate were determined from the position of the element group that received the strong V_{pp}.

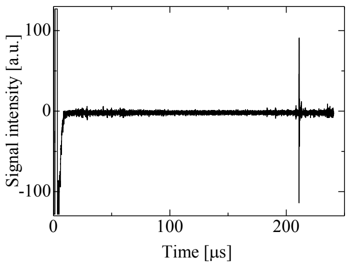

(a) Example of the received waveform obtained at an element group.

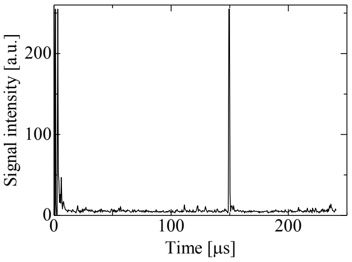

(b) Time variation of V_{pp}.

Figure 3: Received waveform and V_{pp} distribution.

3.2 Three-dimensional rising trajectory of the bubble

Figure 4 shows the two-dimensional distribution of V_{pp} calculated for one scan and its temporal variation. The figure on the left shows the results of one scan measured at the *n*-cycle, and the figure on the right shows the results in the next cycle, that is, at the *n*+1 cycle. The color scale represents the signal intensity, and the V_{pp} values received in each element group are shown. The outer circle indicates the inner diameter of the container. The *z*-axis represents the distance from the sensor surface, and the adjacent planar distributions correspond to the same depth obtained from one scan and the next scan. As the time window is set at 0.5 μs, a two-dimensional V_{pp} can be obtained every 0.5 μs, which corresponds to 0.375 mm. For readability, the distributions are displayed as one image every three images along the time window. Therefore, the distance between each distribution in the *z*-direction appears every 1.125 mm. Because one transmission–reception cycle requires 310 μs, the time difference between the left and right figures is 310 μs × 81 = 25.11 ms.

As shown in the figure, the bubble position can be confirmed in the high-intensity region at z = 129.875 mm for the *n*-cycle. In the next cycle, the position of the measured bubble shifted to z = 123.125 mm. The bubble has a horizontal velocity component, which indicates that the bubble ascended with the oscillation. This indicates that the bubble may move to adjacent element groups during a single measurement cycle. Assuming that the bubble rising velocity is 300 mm/s, the bubble may rise in the vertical direction by up to approximately 0.093 mm during 310 μs, which is the time difference between the measurements of the adjacent element groups in the scanning direction. During 310 μs × 9 = 2790 μs, which is the time difference between the measurements of the adjacent element groups in the direction perpendicular to the scanning direction, the bubble may move 0.837 mm in the *z*-direction. Although errors in the measurement position occur owing to the scanning time, the horizontal position of the bubble can be evaluated based on the center position of the element group with the maximum V_{pp} within one measurement cycle, and the three-dimensional rising trajectory is obtained by repeating and superimposing multiple measurement cycles. To interpolate the position difference, Gaussian interpolation was applied using the V_{pp} of the element group with the maximum intensity and the V_{pp} of the neighboring element groups, and the horizontal bubble position was calculated.

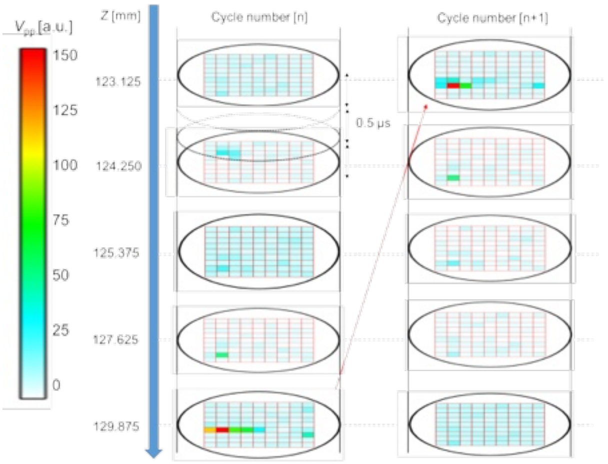

Figure 4: V_{pp} distribution in a measurement cross-section and the change between UPA scan cycles.

Figure 5 shows the temporal variation of the three-dimensional position of the bubble obtained in each plane, that is, the rising trajectory of the bubble. The color represents the cycle number corresponding to time. The bubble positions continuously change in the horizontal direction as the bubble rises in the *z*-direction, indicating that the bubble ascends with the oscillation. This behavior is consistent with visual observation qualitatively. In addition, the distance between successive plots in the z-direction agrees with the rising distance calculated from the measurement time and the bubble rising velocity. Furthermore, the measurable distance also agrees with the value estimated from the measurement time and the sound of velocity. The present measurement system is considered suitable for measuring the three-dimensional rising trajectory of bubbles.

3.4 Simultaneous measurement results with the UPA and the UT

Simultaneous measurements were performed using the UPA and UT. The results are shown in Figure 6. The UT measurement cross-section was placed at the height indicated by the red dashed line. The position of the UT measurement cross-section is shown in Figure 6(a). It can be confirmed that the rising behavior of the bubble with oscillation was successfully measured using the UPA, even when the UT measurement was performed simultaneously. However, the measurable depth decreased

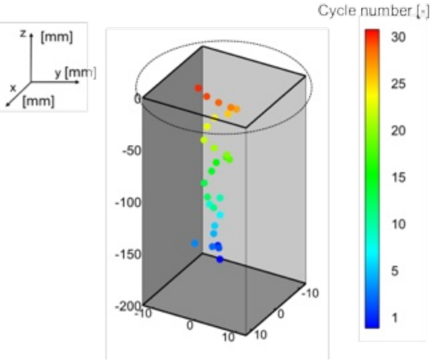

Figure 5: Result of the three-dimensional trajectory of a rising bubble.

compared with that without simultaneous measurement. The amplitude of the reflected signals from the bubble decreased, which is caused by interference between the UPA and UT ultrasonic transmissions. However, sufficient information was obtained to evaluate the rising trajectory of the bubble.

The effects of the UPA measurements on the UT measurement results were also evaluated. Figures 6(b) and (c) show the void distributions obtained by UT measurements without and with simultaneous UPA measurements, respectively. As shown in the figures, noise may appear in the void distribution when the UPA measurement is performed simultaneously. This is also considered to be caused by ultrasonic interference from the UPA measurements. Although the noise increased for the UT image, the cross-sectional shape of the bubble could be sufficiently identified. Although the measurement results were degraded by interference between the ultrasonic emissions in each method, these results demonstrate that simultaneous measurement using the UPA and UT allows for the evaluation of bubble trajectories and bubble shapes.

4. Conclusion

The measurement of bubble-rising trajectories using an ultrasonic phased array (UPA) method was investigated. Strong reflected signals from the gas–liquid interface were successfully detected in the UPA measurement, thereby enabling the reconstruction of the three-dimensional rising trajectory of a single bubble. These results demonstrate that the UPA is effective for evaluating the three-dimensional rising behavior of bubbles. In addition, simultaneous measurements were performed using the UPA and ultrasonic tomography (UT). The results show that the measurement distance of the bubble trajectory decreased for the UPA measurement, and the noise levels in the reconstructed image increased for the UT measurement. However, it was confirmed that simultaneous measurements using the UPA and UT allowed for the evaluation of bubble trajectories and bubble shapes.

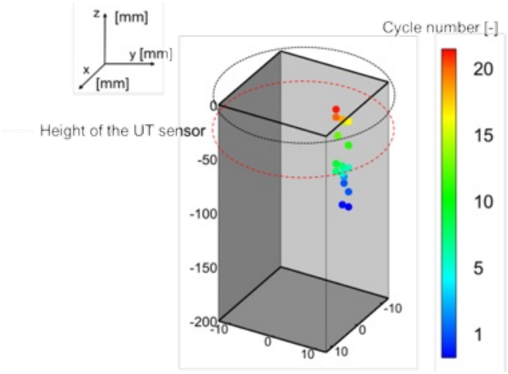

(a) Results of bubble trajectory using UPA.

(b) Bubble shape obtained using UT.

(c) Bubble shape obtained using UT with UPA.

Figure 6: Results of a bubble trajectory and bubble shape obtained using UPA and UT.

References

[1] Keplinger O, Shevchenko N & Eckert S: Visualization of bubble coalescence in bubble chains rising in a liquid metal, Int. J. Multiphase Flow 121 (2019), 103111.

[2] Wu J & Gharib M: Experimental studies on the shape and path of small air bubbles rising in clean water, Physics of Fluids, 14 (2002), 49–52.

[3] Zhang J, Ni M-J & Moreau R: Rising motion of a single bubble through a liquid metal in the presence of a horizontal magnetic field, Physics of Fluids 28 (2016), 032101.

[4] Murakawa H, Maeda S & Eckert S: Effects of a horizontal magnetic field on the cross-sectional distribution of gas bubbles chain rising in a gallium alloy, Int. J. Multiphase Flow 170 (2024), 104649

[5] Nakane T, Maeda S, Sugimoto K & Murakawa H: Evaluation method for the three-dimensional behavior of bubbles in a liquid metal under horizontal magnetic field using ultrasonic tomography, ISIJ Int. 65 (2025), 223–233.

[6] Gou H-Y, Ni M-J & Yao Z-H: Experimental study of a single bubble’s motion in a liquid metal under a horizontal magnetic field, J. Fluid Mech 988 (2024), A-21.

Machine Learning-Based Ultrasonic Tomography for Void Distribution Reconstruction with Noise-Reduction Preprocessing

Yuya Kojima[1], Hideki Murakawa[1], Katsumi Sugimoto[1], Teppei Kondo[2], Yuta Abe[3], Kosuke Aizawa[3]

[1] Dept. of Mechanical Engineering, Kobe University, 1-1 Rokkodai, Nada, Kobe 657-8501, Japan.
[2] NESI, 3600-3 Higashi-ishikawa, Hitachinaka, 312-0052, Japan.
[3] JAEA, 4002 Naritacho, Oarai-machi, Higashi-ibaraki-gun, Ibaraki 311-1313, Japan.

Ultrasonic tomography (UT) is a promising non-intrusive technique for measuring bubbly flows in opaque fluids; however, its reconstruction accuracy significantly deteriorates when multiple bubbles coexist in the measurement cross-section owing to complex wave interactions. To address this limitation, in this study, we propose a machine-learning-assisted UT method capable of simultaneous multi-bubble measurement under realistic experimental conditions. Since acquiring sufficient experimental training data with randomly distributed bubbles is impractical, training datasets were generated using ultrasonic wave propagation analysis. To mitigate the sim-to-real gap between numerical simulations and experiments, waveform preprocessing was introduced to extract bubble-induced signal variations and suppress noise inherent to experimental measurements. A fully connected neural network was trained using full-matrix UT waveforms to predict mesh-wise void fraction distributions. The proposed framework successfully reconstructed the approximate bubble locations and shapes for both simulated and experimental data, despite being trained exclusively on simulation data. Furthermore, the cross-sectional average void fraction was quantitatively estimated with reasonable accuracy. These results demonstrate the robustness and practical applicability of the proposed method for multi-bubble UT measurements in gas–liquid two-phase flows.

Keywords: Ultrasonic tomography, Machine learning, Void distribution, Neural network, Bubbles

1. Introduction

Bubbly flow appears in many industrial applications. Therefore, a comprehensive understanding of its fluid dynamics is important for optimizing production efficiency and ensuring product quality. However, accurately evaluating the shape and behavior of bubbles is particularly challenging in opaque fluids because of experimental limitations. Considering these significant challenges, ultrasonic tomography (UT) has recently attracted attention as a method for measuring these conditions.

Murakawa et al. [1] successfully reconstructed the void distribution using only eight transducers by employing transducers with a wide divergence angle of 110° for a pipe with an inner diameter of 50 mm. This significantly improved the temporal resolution, enabling the measurement of rising bubbles. This technique has been shown to be effective for understanding the behavior of bubbles rising in liquid metals [2]. However, it has been found that the reconstruction accuracy significantly deteriorates when multiple bubbles exist in the measurement cross-section owing to multiple reflections.

Wada et al. [3] demonstrated that UT reconstruction using machine learning (ML) was feasible for dense bubble distributions. By using waveforms obtained from 16 transducers and a neural network with one hidden layer, they showed that approximate bubble shapes could be reconstructed for up to nine bubbles. However, their study was based on the numerical analysis of ideal ultrasound waveforms; it did not account for disturbance factors, such as noise caused by the measurement system and sensor-specific inhomogeneities. Therefore, it is essential to develop a robust learning model that addresses complex and realistic factors when applied to data acquired in a real measurement system.

In this study, a novel machine-learning-assisted UT method that enables the simultaneous measurement of multiple bubbles and is applicable to real experimental environments was developed.

2. Methodology

2.1 Experimental setup

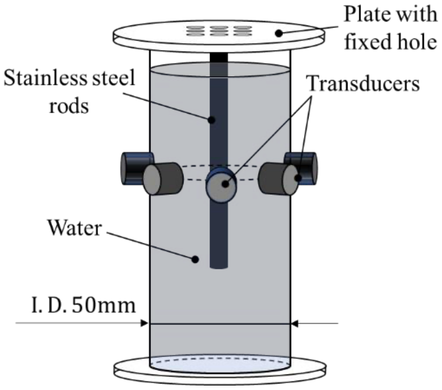

Figure 1: Schematic of the experimental UT measurement system using wide divergence angle ultrasonic transducers.

In this study, UT measurements were conducted using a wide divergence angle ultrasonic sensor developed by Murakawa et al. [1]. Figure 1 shows a schematic of the experimental UT measurement system. The test section consisted of an acrylic cylindrical pipe with an inner diameter of 50 mm, and eight transducers were installed at equal angles along the inner wall of the pipe. This system uses full-matrix capture (FMC) to acquire data. The first transducer emits a pulse, whereas the echo signals are received by all transducers, including the transmitter. In the second step, the role of the transmitter is assigned to the next transducer. During the measurement process, the active role of the transmitter alternates between the transducers and switches in sequence after each pulse emission so that ultrasonic pulses can emanate from all transducers.

Stainless steel rods were used as measurement targets to accurately determine the position and shape. The rods were fixed to an acrylic plate with a fixed hole mounted on the upper part of the pipe, and the position and number of rods could be changed.

2.2 Training data generation

To construct a high-performance machine learning model, it is essential to prepare a large amount of training data. However, acquiring experimental data with randomly distributed bubble positions, diameters, and numbers in sufficient quantities is difficult because of time constraints. Therefore, in this study, a training dataset was generated using ultrasonic wave propagation analysis. A numerical simulation for the propagation analysis was conducted using commercial software (ComWAVE, ver. 11.0.0.0).

Figure 2 shows a schematic of the analysis model. Assuming that the learning model is applied to the data obtained under the experimental setup shown in Section 2.1, a propagation analysis was performed with the same geometry of the test section and sensors as in the experiment. The analysis area was a two-dimensional region with dimensions of 52 mm × 52 mm.

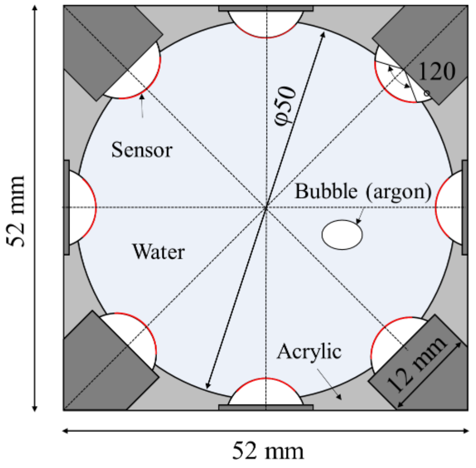

Figure 2: Two-dimensional analysis area for ultrasonic propagation.

Elliptical bubbles were randomly distributed within the analysis domain. The center coordinates of these bubbles were constrained within a circular area with a diameter of 30 mm from the model center. The major axis lengths of the elliptical bubbles were 2–8 mm. Detailed information regarding the generated bubbles and the total number of models is presented in Table 1.

Table 1: Parameters of the generated bubble model.

Number of bubbles	Major axis length a [mm]	Minor axis length b [mm]	Number of models
1	2–8	$a \times 0.75$–1	4800
2	2–8	$a \times 0.75$–1	4800
3	2–8	$a \times 0.75$–1	4800

3. Machine learning model

3.1 Ultrasonic propagation analysis

Figure 3 shows the results of the ultrasonic propagation analysis at (a) 10 µs, (b) 26 µs, (c) 36 µs, and (d) 46 µs of the elapsed time from the pulse emission, where the white arrows indicate the propagation paths of the signals reaching the sensor at each specific time. These results reveal that the ultrasonic waveforms captured by the sensor are not merely simple reflected waves from the bubbles but also include components reflected by the sensor or those resulting from multiple reflections within the medium.

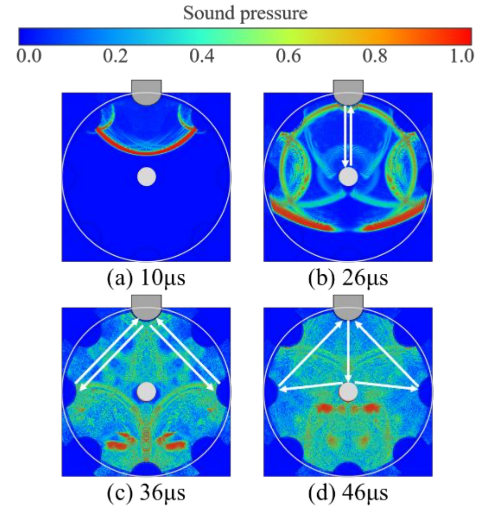

(a) 10μs (b) 26μs

(c) 36μs (d) 46μs

Figure 3: Visualization results of the sound pressure distribution at each elapsed time.

3.2 Adaptation of the experimental data

In machine learning, it is common practice to train models using data obtained from numerical simulations and subsequently apply them to experimental data. However, differences between simulated and experimental data, often referred to as the sim-to-real gap, can significantly degrade model performance if not properly addressed. Therefore, bridging this gap is crucial when deploying simulation-trained models in practical measurement environments.

Figure 4 shows examples of the received waveforms obtained from the simulation and experiments. The left-hand figures show the original received waveforms at a transducer. As indicated in Section 3.1, the received waveforms contain several distinct components. The bubble reflection waves (1) represent the primary signal reflected from the bubbles, whereas pipe wall reflection (2) represents the primary signal reflected from the pipe wall. Multiple reflections (3) appear owing to the ultrasonic waves bouncing between multiple boundaries of the setup. Furthermore, the experimental data specifically contain ultrasonic transmission noise (4) at the beginning of the time domain and other weak noise (5) distributed throughout, both of which are absent in the simulation data. Because differences in the received waveforms may affect the prediction accuracy of machine-learning models, a moving-window maximum filter and subtraction from the non-bubble condition were applied. The results are shown in the right-hand figures. Through this calculation, waveform differences associated with the presence of bubbles were extracted, and noise components that exist regardless of bubble presence in the experimental data were effectively removed.

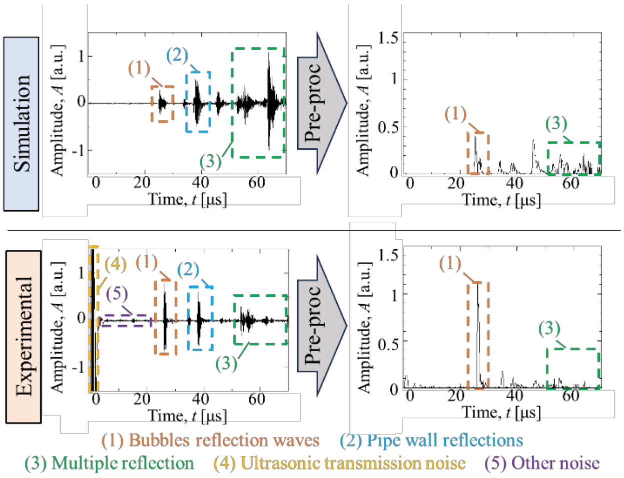

Figure 4: Received waveforms obtained from the simulation and experiment before and after preprocessing.

3.3 Void distribution prediction

Using the preprocessed waveforms described in the previous section, a machine learning model was constructed to predict the void fraction distribution. The received signals were concatenated to form a one-dimensional input vector for the machine learning model.

The ground-truth labels for supervised learning were defined as the local void fraction in each region, discretized on a 1 mm × 1 mm mesh, based on bubble distributions generated by ultrasound propagation analysis.

A fully connected neural network (FCNN) was employed as the machine learning model. The network architecture and training parameters are summarized in Tables 2 and 3. The model was implemented in Python (Ver. 3.10.0) using the Keras (Ver. 3.10.0) and TensorFlow (Ver. 2.19.0) libraries, and the Sigmoid function was used as the activation function in the input and hidden layers. The data obtained from a total of 14,400 simulation models were used by dividing the training, validation, and test data at a ratio of 8:1:1. The validation data were used to optimize the hyperparameters. After the grid search, the parameters were set to a learning rate of 0.01, epoch count of 20, and a batch size of 32.

Table 2: Structure of the FCNN.

Parameters	Input layer	Hidden layer	Output layer
Node size	22,400	5,600	1840
Activate function	Sigmoid	Sigmoid	Linear

Table 3: Parameters related to FCNN training

Parameters	Used by FCNN
Loss function	Binary cross-entropy
Optimizer	RMSprop

Figure 4 shows the variation in the prediction accuracy, *acc*, during the training process, with the results for the training and validation datasets presented separately. Accuracy was evaluated using the Pearson correlation coefficient as the primary metric. The Pearson correlation coefficient ranges from -1 to 1, and values closer to 1 indicate a higher degree of agreement between the predicted and true void fraction distributions. As the number of epochs increases, the prediction accuracy improves. In addition, the prediction accuracies for the training and validation datasets exhibit similar trends with only a small discrepancy, suggesting that overfitting does not occur significantly.

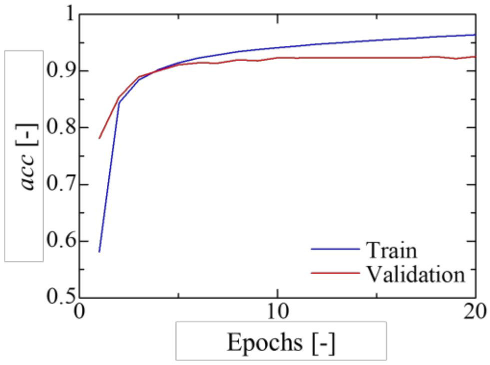

Figure 5: Changes in *acc* during the learning process.

Figure 6 shows a comparison of the output results obtained by applying the developed machine learning model to the data obtained from the simulations and experimental data. The answer void fraction distribution is shown for reference. The approximate locations and shapes of the bubbles could be successfully estimated for both simulation and experimental data. Although the machine learning model was trained solely using simulation data, a high prediction accuracy was also achieved for the experimental data. This result suggests that the proposed waveform processing framework effectively mitigates the Sim-to-Real gap.

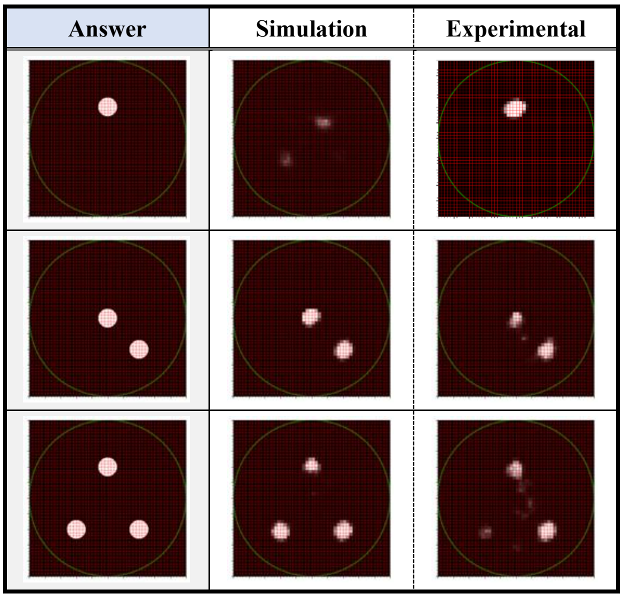

Figure 6: Answer and predicted void distribution for simulation and experimental data.

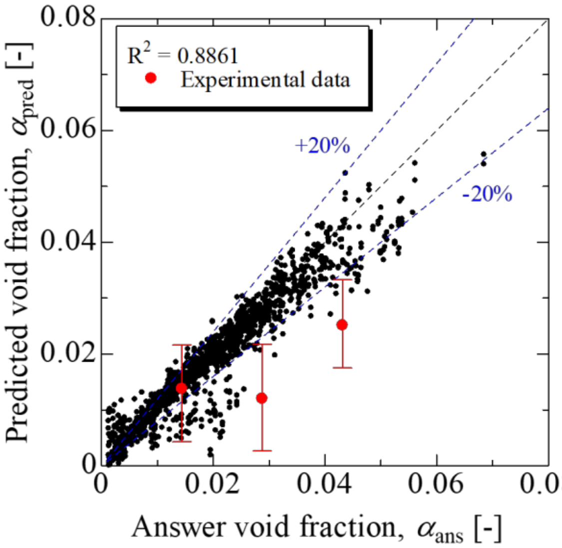

Figure 7: Evaluation of cross-section average void fraction.

In addition, the estimation of the cross-sectional average void fraction is important for quantitatively evaluating the flow characteristics of gas–liquid two-phase flows in pipes. Figure 7 shows the results of calculating the cross-sectional average void fraction in the pipe based on the void fraction of each mesh predicted by the machine learning model. The horizontal axis represents the reference cross-sectional average void fraction calculated from the model settings of the ultrasonic propagation analysis and the diameter of the stainless-steel rod, whereas the vertical axis represents the cross-sectional average void fraction calculated from the mesh-wise void fractions predicted by the machine learning model. The black markers indicate the results for the simulation data, and the red markers indicate those for the experimental data. The error bars represent the maximum and minimum values obtained for each bubble count condition. For the simulation data, the cross-sectional average void fraction can be estimated within an error range of approximately ±20%. In contrast, larger scatter was observed for the experimental data. The results indicate that under conditions with a large number of bubbles, the predicted void fraction tends to be consistently lower than the corresponding reference void fraction. One possible reason for this tendency is that the experimental waveforms exhibit an attenuation rate that is larger than that of the simulation data, resulting in a reduction in multiple-reflection components. This discrepancy in attenuation is primarily attributed to the use of a 2D model in the propagation analysis; specifically, the 2D simulation tends to underestimate the energy dissipation compared to actual 3D experimental environments. Because the machine learning model was trained using simulation data that do not fully account for such attenuation effects, this discrepancy in waveform characteristics is considered to contribute to the observed underestimation. From this perspective, applying an attenuation-matching preprocessing technique to the simulation data would be an effective approach for improving the prediction accuracy of experimental data.

4. Conclusion

A machine-learning-assisted ultrasonic tomography (UT) method was developed to simultaneously measure multiple bubbles in opaque fluids. By integrating a fully connected neural network with ultrasonic propagation analysis, the proposed framework successfully accounts for multiple-reflection components, which are typically neglected in conventional UT reconstruction.

The results demonstrate that the model, which was trained exclusively on 2D simulation data, generalized effectively to real experimental environments using a dedicated waveform preprocessing strategy. The cross-sectional average void fraction was estimated within an error range of approximately ±20% for the simulation data. Although the experimental results exhibited larger scatter and an underestimation trend under high void fraction conditions—primarily because of the attenuation mismatch between 2D simulations and 3D physical space—the robustness of the method against realistic disturbances was confirmed.

References

[1] Murakawa H et al.: Development of a high-speed ultrasonic tomography system for measurements of rising bubbles in horizontal cross-section, Measurement 181 (2021), 109654.

[2] Nakane T et al.: Evaluation Method for the Tree-dimensional Behavior of Bubbles in a Liquid Metal under Horizontal Magnetic Field Using Ultrasonic Tomography, ISIJ Int. 65 (2025), 223-233

[3] Wada Y et al.: A numerical study on machine-learning-based ultrasound tomography of bubbly two-phase flows, Ultrasonics 141 (2024), 107346.